

Infrared horizon sensor using multi-element thermopile imaging array for CubeSat orbital attitude determination.

Ace Janssen

This honours thesis is presented for the Degree of
B. Eng Mechatronics Engineering,
School of Civil & Mechanical Engineering
Curtin University.

October 2024

[Blank Page]

Declaration

To the best of my knowledge and belief this thesis contains no material previously published by any other person except where due acknowledgement has been made. This thesis contains no material which has been accepted for my award of any other degree or diploma in any university.

A.Janssen

29th October 2024

Acknowledgements

I wish to acknowledge the invaluable influence of Dr Robert Howie (BEng PhD), whose teachings throughout my studies played a pivotal role in shaping my academic path in space science engineering. Their enthusiasm for the subject and thoughtful guidance sparked my desire to conduct research in this field. I am grateful for the opportunity to have been their student, and for the knowledge and fascination in space they imparted.

Special thanks to Matt Creed (GradDipPsych) and Chris Douglas (MSci) for their time and attention in proofreading my thesis. Their thoughtful insights were truly helpful.

Abstract

This paper explores the application of a thermopile imaging array as an infrared horizon sensor to enhance the orbital navigation capabilities of resource-limited small-satellite platforms. Traditional image-based horizon sensors provide orientation information by detecting planetary edges against the background of space, a process often performed using visible light cameras due to the typically limited resolution of infrared imaging sensors. This study illustrates some of the advantages of using the infrared band for horizon detection, and explores recent advancements in sub-pixel edge localisation techniques, specifically the Zernike polynomials, to improve the performance of low-resolution thermal imaging sensors for horizon detection. To evaluate the utility of this technique, a prototype infrared horizon sensor and simulated infrared orbital view test stand was built to assess its performance.

Key components of this study include an introduction to the general concepts used for orbital attitude determination using horizon sensors, and a review of existing techniques in the visible and infrared bands. The practical design considerations required to create an operational prototype are also discussed, with specific context given to the space environment, and designing for resource limited small-satellites.

Using the sub-pixel edge localisation technique on a 32x24 pixel thermopile array, the prototype was able to determine the spacecraft's attitude with an accuracy of $\pm 5^\circ$ relative to the nadir vector of the physically simulated orbital horizon scene.

Although the response rate of these thermopile sensors still requires further study, the findings indicate that this sub-pixel correction method allowed the sensor to perform at a level that may be expected of higher-resolution system; and to the authors knowledge, this marks the first application of this technique to infrared imagery in horizon detection. The results demonstrate that adapting visible-light edge-detection techniques to infrared systems can enhance their precision, supporting opportunities for their use on resource-constrained small-satellite missions.

These findings underscore how bridging theoretical innovations with practical application in adjacent fields can open avenues for future advancements in space systems.

Nomenclature

ADCS	Attitude, Determination & Control Subsystem
API	Application Programming Interface
Attitude	The orientation / pointing of a craft relative to a known reference frame
CAD	Computer Aided Design
CubeSat	Design specification for small satellites, sizes are commonly referenced in units of ‘U’, each unit of ‘U’ being a 10x10x10cm cubic volume
CV	Computer Vision
FIR	Far Infrared; infrared radiation with a wavelength in the range 15 to 1,000 μ m
FOV	Field Of View
FPU	Floating-Point arithmetic Unit
GNC	Guidance, Navigation & Control system
I2C	Inter-Integrated Circuit; a serial communication protocol that connects embedded peripheral devices
IC	Integrated Circuit
KB	Kilobyte; represents a measurement of 1,000-bytes of computer memory
LED	Light Emitting Diode
LEO	Low Earth Orbit; approx. ~300km-900km altitude
LiPo	Lithium-ion Polymer; a rechargeable battery technology

LWIR	Long Wavelength Infrared; infrared radiation with a wavelength in the range 8 to 15 μ m
MB	Megabyte, represents a measurement of 1,000,000-bytes of computer memory
MEMS	Micro Electro-Mechanical System
Nadir Vector	Imaginary axis indicating the local vertical from the centre of the orbited body to the orbiting craft
PCB	Printed Circuit Board
PWM	Pulse Width Modulation
RANSAC	Random Sample Consensus
RCS	Reaction Control System
SMD	Surface Mount Device
SPI	Serial Peripheral Interface; a serial communication protocol that connects embedded peripheral devices
UART	Universal Asynchronous Receiver-Transmitter; a serial communication protocol

Table of Contents

Acknowledgements	i
Abstract	ii
Nomenclature	iii
List of Figures	vii
List of Tables	xii
1. Introduction.....	1
1.1 Purpose	1
1.2 Aims	2
1.3 Background	3
1.3.1 Perceiving the Planet.....	5
1.3.2 Infrared Sensors	8
1.3.3 Horizon Detection	9
1.3.4 Sub-Pixel Edge Localisation.....	10
1.3.5 Geometry & Coordinate Frames	13
1.3.6 Conic Projection of Visible Horizon	18
2. Method & Design.....	24
2.1 Requirements Verification Matrix	25
2.2 Horizon Sensor Prototype.....	28
2.2.1 Hardware	28
2.2.2 Firmware	33
2.2.3 Host Device Viewing Software	44
2.3 Orbital View Test Stand.....	47
2.3.1 Proxy Infrared Orbital Scene	47
2.3.2 Controlled Pitch-Roll Axis Gimbal.....	53
3. Results & Discussion.....	56
3.1 Horizon Sensor Prototype Verification.....	56
3.1.1 [P-1] Infrared Sensitivity.....	57
3.1.2 [P-2] Thermal Sensor Image	58
3.1.3 [P-3] Coarse Edge Detection.....	60
3.1.4 [P-4] Sub-Pixel Edge Correction	63
3.1.5 [P-5] Conic Fitting	67
3.1.6 [P-6] Attitude Estimation	69
3.1.7 [P-7] Power Supply	80
3.1.8 [P-8] External Interface.....	81
3.2 Orbital View Test Stand Verification	82
3.2.1 [P-9] Simulated Orbital View.....	82

3.2.2	[P-10] Positional Pitch-Roll Gimbal	86
3.2.3	[P-11] Test Stand Functional Range.....	86
4.	Conclusions.....	90
5.	Suggested Future Work.....	91
5.1	Component Selection	91
5.2	Launch / Space Environment Testing.....	92
5.3	Alternate Conic View Test Stand.....	93
5.4	Skip Conic Fitting	95
6.	References.....	97
APPENDIX A – Horizon Sensor Schematic		102
APPENDIX B – Horizon Sensor PCB Layout		103
APPENDIX C – PCB Trace Electrical Calculations.....		104
APPENDIX D – Software Flowchart Illustration.....		105
APPENDIX E – Prototype Conic Fitting Results		106
APPENDIX F – Prototype Attitude Estimation Results		115

List of Figures

Fig. 1 Render of Libertas 1U (10cm3) CubeSat by Virginia CubeSat Constellation [1]	3
Fig. 2 CubeSat deployment tubes being prepared within separation ring below Artemis I payload at NASA's Kennedy Space Centre in Florida [3].....	4
Fig. 3 Electromagnetic spectrum bands and associated wavelengths. Adapted from [6]	6
Fig. 4 Spectral wavelength distribution of energy to Earth from the Sun [10]	7
Fig. 5 Illustrative depiction of infrared Earth vs visible band. Adapted from [9].....	8
Fig. 6 Illustration of working principles of photonic vs thermal infrared detection	9
Fig. 7 Edge detection inaccuracy due pixel level edge sequence, <i>i.e.</i> from a typical low resolution thermal image.....	10
Fig. 8 Illustration of the first six Zernike polynomial aberrations. Adapted from [23]	11
Fig. 9 Illustration of sub-pixel adjustment to detected edge in low resolution thermal image	13
Fig. 10 Geometry of visible horizon transition relative to nadir vector and orbit altitude	14
Fig. 11 Illustration of pinhole camera world and projection planes.....	14
Fig. 12 Assigned pinhole camera coordinate reference frames. Adapted from [26]..	16
Fig. 13 Circular visible horizon view cone. Adapted from [28]	18
Fig. 14 Side section of a spacecraft's visible horizon view cone. Adapted from [9].	19
Fig. 15 Side section illustrating pinhole camera projection of world image plane to sensor array, while in nominal orientation. Adapted from [9]	19
Fig. 16 Illustration depicting how the horizon view cone projects the circular visible horizon to a conic section in the sensors image plane, relative to orientation of sensor	20
Fig. 17 From the cone's axis, the angle to its surface and the angle of the cutting plane are related to the eccentricity of the generated conic section.....	22

Fig. 18 Prototype PCB render, marked zone indicates key horizon detection hardware	32
Fig. 19 Component placement prior to reflow soldering	32
Fig. 20 Assembled horizon sensor prototype PCB	33
Fig. 21 Illustration of image intensity gradient field as 3D surface, used to identify prominent edges in the image	38
Fig. 22 Illustration of 7x7 image patch with pixel coordinates (u, v), and overlayed unit circle indicating the white area in which the Zernike polynomials are defined .	39
Fig. 23 Zernike 7x7 tilt and defocus aberration mask kernels	40
Fig. 24 Illustration of unit circle correction vector to edge perpendicular.....	41
Fig. 25 Example illustration of the prototypes image frame at some arbitrary orientation relative to the planet.....	43
Fig. 26 Illustration of a Euler $RzRx'$ attitude determination of nadir vector relative to horizon sensor bore	44
Fig. 27 Illustration depicting the serialised communication convention used by the prototype to send image and coordinate data to external host	45
Fig. 28 Host software image rendering options as OpenCV backend vs terminal ASCII gradient image.....	46
Fig. 29 Simulated infrared orbital view test stand design model	48
Fig. 30 Side section of simulated infrared orbital horizon view test stand	48
Fig. 31 Parametric model of visible horizon projection to world image plane, from $55^\circ \times 35^\circ$ FOV sensor, while in nominal orientation; ρ selected to match projected horizon conic shape bound to image frame.....	49
Fig. 32 Silicon heating mats attached to rear of horizon front plate	51
Fig. 33 Proxy infrared horizon view test stand rear	52
Fig. 34 Rear top-angled view of test stand showing mounting support structures	53
Fig. 35 Pitch-roll gimbal model components, associated coordinate frame and scribed indication markings	54
Fig. 36 Base structure tripod mount and aluminium flat bar reinforcement.....	55

Fig. 37 Assembled pitch-roll gimbal.....	55
Fig. 38 MLX90640 image feature validation against calibrated FLIR One Pro thermal camera	59
Fig. 39 MLX90640 separate subframe transmissions required to construct each thermal image [30]	59
Fig. 40 Prototype image pre-processing and coarse edge sequence detection, rendered from host device in greyscale using OpenCV.....	61
Fig. 41 Transitional ghosting artifact during rapid movement due to response rate of thermal detector.....	62
Fig. 42 Right positioned orbital horizon thermal image, identified edge contour and correction received from prototype; pixel-level guess in blue, sub-pixel edge correction shown in red.....	64
Fig. 43 Top-right positioned orbital horizon thermal image, identified edge contour and correction received from prototype; pixel-level guess in blue, sub-pixel edge correction shown in red.....	64
Fig. 44 Top positioned orbital horizon thermal image, identified edge contour and correction received from prototype; pixel-level guess in blue, sub-pixel edge correction shown in red.....	65
Fig. 45 Top-left positioned orbital horizon thermal image, identified edge contour and correction received from prototype; pixel-level guess in blue, sub-pixel edge correction shown in red.....	65
Fig. 46 Left positioned orbital horizon thermal image, identified edge contour and correction received from prototype; pixel-level guess in blue, sub-pixel edge correction shown in red.....	66
Fig. 47 The eccentricity spread of conic models fit to the test stands horizon edge by the prototype at various roll angles; yellow line depicts bounds of success criteria..	68
Fig. 48 Sensors thermal image of simulated orbital horizon and detected horizon edge; viewed with -40° z-axis roll in the sensor / gimbal frame	70
Fig. 49 Sensors thermal image of simulated orbital horizon and detected horizon edge; viewed with -30° z-axis roll in the sensor / gimbal frame	71
Fig. 50 Sensors thermal image of simulated orbital horizon and detected horizon edge; viewed with -20° z-axis roll in the sensor / gimbal frame	72

Fig. 51 Sensors thermal image of simulated orbital horizon and detected horizon edge; viewed with -10° z-axis roll in the sensor / gimbal frame	73
Fig. 52 Prototype thermal image of simulated orbital horizon and detected horizon edge; viewed with 0° z-axis roll in the sensor / gimbal frame	74
Fig. 53 Sensors thermal image of simulated orbital horizon and detected horizon edge; viewed with +10° z-axis roll in the sensor / gimbal frame	75
Fig. 54 Sensors thermal image of simulated orbital horizon and detected horizon edge; viewed with +20° z-axis roll in the sensor / gimbal frame	76
Fig. 55 Sensors thermal image of simulated orbital horizon and detected horizon edge; viewed with +30° z-axis roll in the sensor / gimbal frame	77
Fig. 56 Sensors thermal image of simulated orbital horizon and detected horizon edge; viewed with +40° z-axis roll in the sensor / gimbal frame	78
Fig. 57 Illustration of conic rotation discrepancy from two well-fit models; contour points and models taken from the -20° gimbal roll dataset [$Rz_{accepted} = 20^\circ \pm 5^\circ$]	79
Fig. 58 Host device thermal rendering and debug display of serial output from prototype horizon sensor	81
Fig. 59 Test stand FOV bound conic apex measurement	83
Fig. 60 Test stand receiving liquid nitrogen to cool the proxy space background plate	83
Fig. 61 Simulated orbital view test stand distinct thermal edge verification	84
Fig. 62 Orbital view test stand, prototype sensor, and pitch-roll gimbal	85
Fig. 63 Test stand functional range verification, pitch-roll gimbal at 0° roll and $\pm 5^\circ$ pitch.....	87
Fig. 64 Test stand functional range verification, pitch-roll gimbal at -45° roll and $\pm 5^\circ$ pitch.....	88
Fig. 65 Test stand functional range verification, pitch-roll gimbal at +45° roll and $\pm 5^\circ$ pitch.....	88
Fig. 66 Example illustration of QFP vs QFN package formfactor. Adapted from [45]	93

Fig. 67 Alternative idea for simulated infrared orbital view test stand, to more accurately represent the projected horizon conic in the sensors image frame during pitch movements; scaled to model a 600km LEO orbit altitude.....	94
Fig. 68 Illustration of Christian-Robinson projection transform to unit sphere vector space	96
Fig. 69 Conic models fit to imaged horizon edge by the prototype sensor at -40° z-axis roll. Orange marks represent edge coordinates, lines depict fit conic models.....	107
Fig. 70 Conic models fit to imaged horizon edge by the prototype sensor at -30° z-axis roll. Orange marks represent edge coordinates, lines depict fit conic models.....	108
Fig. 71 Conic models fit to imaged horizon edge by the prototype sensor at -20° z-axis roll. Orange marks represent edge coordinates, lines depict fit conic models	109
Fig. 72 Conic models fit to imaged horizon edge by the prototype sensor at -10° z-axis roll. Orange marks represent edge coordinates, lines depict fit conic models	110
Fig. 73 Conic models fit to imaged horizon edge by the prototype sensor at +10° z-axis roll. Orange marks represent edge coordinates, lines depict fit conic models .	111
Fig. 74 Conic models fit to imaged horizon edge by the prototype sensor at +20° z-axis roll. Orange marks represent edge coordinates, lines depict fit conic models .	112
Fig. 75 Conic models fit to imaged horizon edge by the prototype sensor at +30° z-axis roll. Orange marks represent edge coordinates, lines depict fit conic models .	113
Fig. 76 Conic models fit to imaged horizon edge by the prototype sensor at +40° z-axis roll. Orange marks represent edge coordinates, lines depict fit conic models .	114

List of Tables

TABLE 1 Project Requirement Statement and Verification Criteria	25
TABLE 2 Identified conic projective discriminant relative to image frame for 55°x35° FOV sensor while in nominal orientation	50
TABLE 3 Scaled conic discriminant values relative to test stands 380x300mm face	50
TABLE 4 Horizon Sensor Prototype Requirement Verification Results	56
TABLE 5 MLX90640 subframe refresh rate effects on image generation period....	60
TABLE 6 Average of initial results received from prototype while at -40° z-axis roll in the sensor / gimbal frame; refer Appendix F for individual results	70
TABLE 7 Average of initial results received from prototype while at -30° z-axis roll in the sensor / gimbal frame; refer Appendix F for individual results	71
TABLE 8 Average of initial results received from prototype while at -20° z-axis roll in the sensor / gimbal frame; refer Appendix F for individual results	72
TABLE 9 Average of initial results received from prototype while at -10° z-axis roll in the sensor / gimbal frame; refer Appendix F for individual results	73
TABLE 10 Average of initial results received from prototype while at 0° z-axis roll in the sensor / gimbal frame; refer Appendix F for individual results	74
TABLE 11 Average of initial results received from prototype while at +10° z-axis roll in the sensor / gimbal frame; refer Appendix F for individual results	75
TABLE 12 Average of initial results received from prototype while at +20° z-axis roll in the sensor / gimbal frame; refer Appendix F for individual results	76
TABLE 13 Average of initial results received from prototype while at +30° z-axis roll in the sensor / gimbal frame; refer Appendix F for individual results	77
TABLE 14 Average of initial results received from prototype while at +40° z-axis roll in the sensor / gimbal frame; refer Appendix F for individual results	78
TABLE 15 Prototype supply range verification.....	80
TABLE 16 Orbital View Test Stand Requirement Verification Results.....	82
TABLE 17 Comparison of orbital view temperatures vs simulated (*contingent cold plate temperature transfer assumption)	85
TABLE 18 Initial 5 conic models fit to imaged horizon edge by RANSAC on prototype sensor while at -40° z-axis roll; model colours in first column align to graph above	107
TABLE 19 Initial 5 conic models fit to imaged horizon edge by RANSAC on prototype sensor while at -30° z-axis roll; model colours in first column align to graph above	108

TABLE 20 Initial 5 conic models fit to imaged horizon edge by RANSAC on prototype sensor while at -20° z-axis roll; model colours in first column align to graph above	109
TABLE 21 Initial 5 conic models fit to imaged horizon edge by RANSAC on prototype sensor while at -10° z-axis roll; model colours in first column align to graph above	110
TABLE 22 Initial 5 conic models fit to imaged horizon edge by RANSAC on prototype sensor while at +10° z-axis roll; model colours in first column align to graph above	111
TABLE 23 Initial 5 conic models fit to imaged horizon edge by RANSAC on prototype sensor while at +20° z-axis roll; model colours in first column align to graph above	112
TABLE 24 Initial 5 conic models fit to imaged horizon edge by RANSAC on prototype sensor while at +30° z-axis roll; model colours in first column align to graph above	113
TABLE 25 Initial 5 conic models fit to imaged horizon edge by RANSAC on prototype sensor while at +40° z-axis roll; model colours in first column align to graph above	114
TABLE 26 Prototype Horizon Sensor Attitude Estimation Results.....	115

1. Introduction

This paper investigates the utility of a thermopile imaging array in orbital navigation, specifically an infrared horizon sensor for detecting the attitude of a spacecraft relative to the planet it is orbiting. Horizon sensors typically perform this task by detecting the transition of the planets edge against the background of space, *i.e.* the planets horizon. With knowledge of the sensor's location relative to the crafts frame of reference, the horizon sensor can estimate the crafts orientation relative to the planet based on the location and shape of the detected horizon edge. This information is critical for orbital navigation, and to ensure any equipment or payloads carried by the craft are correctly oriented to perform their intended function; for example, planetary imaging, scientific experiments, aligning communication antennas to ground stations, informing the crafts reaction control system, and sequencing thrust outputs / burns.

1.1 Purpose

The purpose of this paper is to progress infrared horizon detection research in the field of orbital navigation, particularly for small-satellite platforms. As space missions increasingly prioritise compact, efficient, and cost-effective systems, there is a growing demand for reliable horizon sensors that innovate on existing research.

While image-based horizon detection using visible light has seen significant advancements, detecting the horizon in the infrared band offers several advantages, particularly in varying lighting conditions and during Earth's eclipse, where visible light is limited. However, infrared imaging sensors are often hindered by lower resolution, which can reduce the accuracy of their detected horizon.

This research fills a key gap in infrared orbital navigation by leveraging recent breakthroughs in sub-pixel edge localisation techniques traditionally applied to visible-band imagery, specifically the use of the Zernike polynomials. By adapting this novel technique to infrared horizon detection, the research seeks to enhance the precision and detection performance of low-resolution infrared sensors. This not only improves the functionality of these sensors but also opens new opportunities for their use in small, resource-limited spacecraft. The findings will contribute to the broader

field of satellite navigation by demonstrating how innovative computational techniques can optimise existing hardware for improved space systems performance.

1.2 Aims

The aim of this paper focuses on reviewing current research on visible and infrared horizon detection, and integrating research across fields to build a prototype infrared horizon sensor, and a simulated orbital view test stand to assess its utility. While much of the existing research describes theoretical approaches and simulations, a physical prototype provides a deeper contextualisation of the integrated system, particularly in the context of the space environment, and other real-world considerations required in the design and construction of a working model.

This work ultimately seeks to bridge theoretical research and practical application, contributing to a new generation of navigation solutions tailored to the constraints and demands of small-satellite platforms.

1.3 Background

Humanity's innate curiosity has always pushed us towards new frontiers of discovery. We stand at a pivotal time in history where our advancing capabilities push those frontiers past the confines of our planet, and into the unknowns of space and beyond.

Recent advancements in the miniaturisation of technology have made this space frontier more accessible than ever. This has fostered a growing interest from the commercial and research sectors for small-scale ($<100\text{kg}$) orbital satellites with capabilities comparable to those historically reserved to government-backed space programs, or heavily funded commercial initiatives. Current developments include applications in planetary imaging, broadcasting and communication infrastructure, weather forecasting / atmospheric monitoring, global navigation networks, and scientific experiments, as a few examples.



Fig. 1 Render of Libertas 1U (10cm^3) CubeSat by Virginia CubeSat Constellation [1]

The standardisation of small-satellites through the CubeSat specification [2] has been a key facilitator of this growing industry. The specification defines standard interface and dimensional requirements for small-satellite designers to adhere to, and are classified in 'U' units of 10cm^3 volumes; an example of a 1U CubeSat is shown above

in Fig. 1. The standardisation of small-satellites has enabled a reduction in the cost of getting small payloads into space, by allowing integration of multiple disparate CubeSat designs to be deployed from a single common CubeSat deployment mechanism. These deployment tubes are commonly attached as tertiary payloads to existing rocket launches (see Fig. 2), akin to a ‘ride-share’ scheme which distributes the costs of getting into space.



Fig. 2 CubeSat deployment tubes being prepared within separation ring below Artemis I payload at NASA’s Kennedy Space Centre in Florida [3]

Operating in the space environment poses many unique challenges, and spacecraft designers must constantly balance the constraints of size, cost, power, and weight. Small satellites typically have a finite supply of resources available to achieve their mission objective, meaning the actions the craft takes should be considered and measured. A key aspect of any space bound craft is therefore its ability to perceive its current orbital position and orientation in 3D space, such that control outputs (*e.g.* to reaction wheels, payload deployments, RCS thrusters *etc.*), are performed accurately, efficiently, and result in the intended behaviour.

The system that manages the orbital navigation of the craft is the Guidance, Navigation & Control (GNC) system; with the crafts orientation at any point within the orbit

typically managed by a subsystem of the GNC, referred to as the Attitude Determination & Control Subsystem (ADCS) [4]. Together, they interpret and control the position, stability, and orientation of the craft in 3D space relative to a given frame of reference.

In orbital attitude determination, a common non-inertial frame of reference used by the ADCS is the local vertical to the planet's surface, *i.e.* the nadir vector. This vector represents an imaginary line extending from the spacecraft directly towards the centre of the body it is orbiting.

The nadir vector provides crucial information about the spacecraft's orientation relative to the planet's surface; and knowledge of its location relative to the crafts orientation can be used to solve for all rotational degrees of freedom, bar the one about the nadir vector itself.

The challenge of attitude determination in the context of general spacecraft design is one which is well researched; and a multitude of sensor technologies are currently available [4], each with their own advantages, disadvantages, and expected performance targets. Despite many of these technologies initially being developed with a weight, cost, and size envelope typical of a moderately sized spacecraft, miniaturisation and ongoing technological improvements have now made them viable options for use on small-satellites too.

In the context of this paper, determining a crafts orbital attitude is investigated through the use of an infrared planetary horizon sensor.

1.3.1 Perceiving the Planet

The general approach to determine the crafts attitude with a horizon sensor involves using a set of sensors to detect a planets horizon edge transition. The sensors perceive the horizon by detecting certain bands of the electromagnetic spectrum (Fig. 3) that the planet radiates against the $\sim 270^{\circ}\text{C}$ (3 Kelvin) background of space [5].

By analysing the shape and relative angles to the horizon edge, the horizon sensor can accurately determine the local vertical to the planet (the nadir vector), and therefore the crafts pointing relative to the planet's surface.

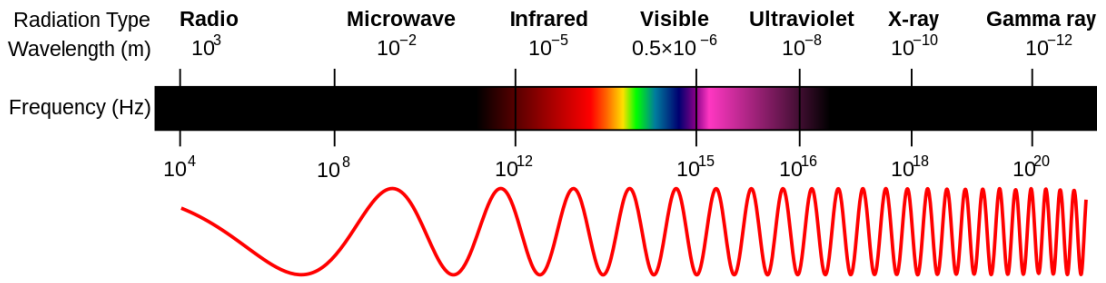


Fig. 3 Electromagnetic spectrum bands and associated wavelengths. Adapted from [6]

To better understand the expected radiation bands detectable from the planet while in orbit, it is worth considering a generalised balance of the planets thermal system.

The Earth is constantly being bombarded with electromagnetic radiation from the Sun, see Fig. 4, which emits primarily between the radio and x-ray bands. The radiation that reaches Earth's atmosphere is either absorbed by the planet, or reflected back into space based on planetary atmospheric conditions (*i.e.* planetary albedo) [5]. Of the radiation received by Earth from the Sun, approximately 70% of its energy is in the visible and near-infrared range [7]; which remains mostly un-absorbed as it travels through the atmosphere to ground level, where its energy is dissipated into the planet's surface.¹

Planks law tells us that the spectral radiance of a hypothetical black body, which is an object that absorbs all radiation incident upon it and emits radiation across a continuous spectrum based on the bodies uniform temperature, has a peak emission that shifts to shorter wavelengths as the body's temperature increases.

Consider that a planets overall thermal system must balance energy absorbed with energy emitted to maintain a relatively stable temperature that is neither rising or falling over a continuous period. Modelling the Earth as a black body, the surface therefore re-emits the Suns absorbed energy based on the planet's average temperature; as of 2023 the average global temperature is $\sim 15^\circ\text{C}$ (288K) [8] which indicates the primary black body radiation peak emission is in the infrared band of electromagnetic spectrum, with a wavelength of ~ 2 to $50\mu\text{m}$ [5].

¹*As an aside, this observation aligns with what we see from an evolutionary perspective, where eyes have adapted to be most sensitive to the visible band of the spectrum, which is the prominent radiation band at ground level.*

Spectrum of Solar Radiation (Earth)

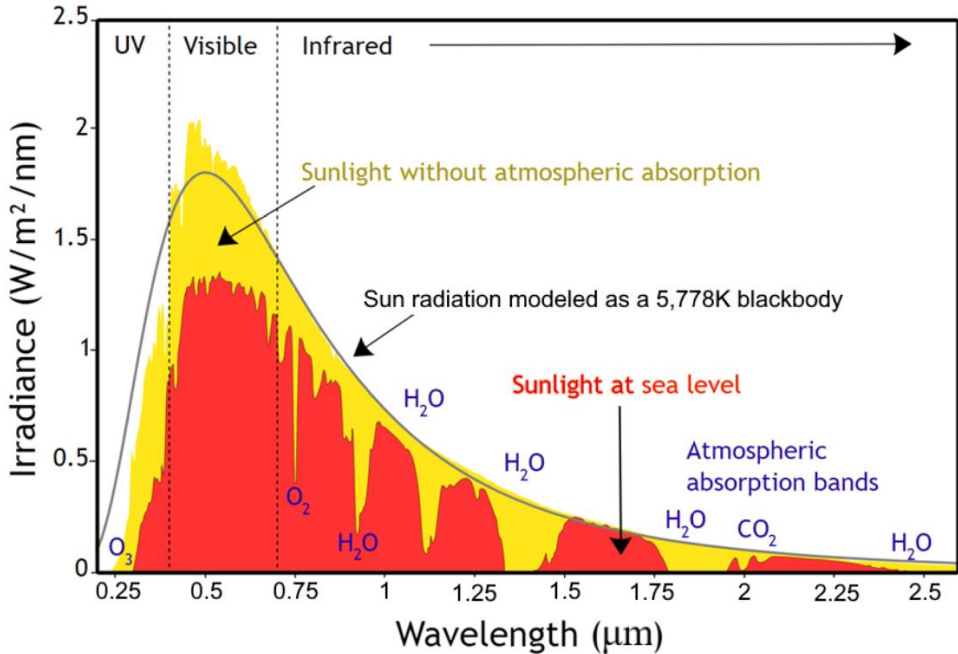


Fig. 4 Spectral wavelength distribution of energy to Earth from the Sun [10]

Radiation emitted in the infrared band is readily absorbed by elements in the atmosphere, primarily due to water vapor, carbon dioxide (CO_2), and ozone [7]. The CO_2 band in the range 14 to 16 μm [5] is commonly selected as the target band for orbital infrared detectors. This is due to its consistent presence from space while in and out of eclipse, good rejection of false edges in cloud cover and other geographic features, and low temporal variation relative to the background of space [5]. These characteristics demonstrate some of the appealing advantages of using the infrared band to detect the horizon edge, vs standard visible band cameras; an illustrative depiction is shown Fig. 5.

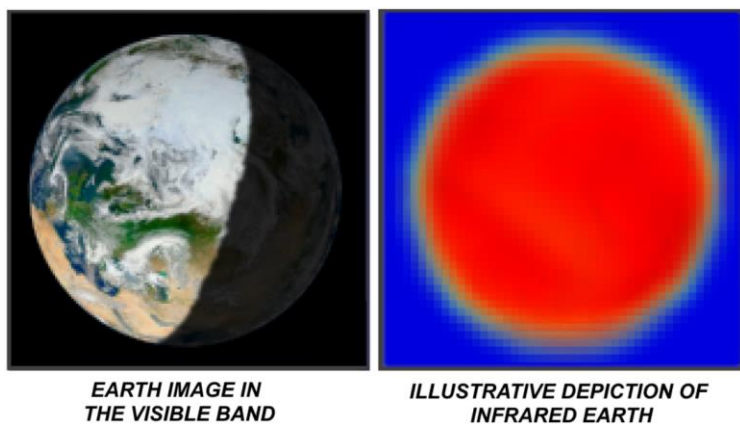


Fig. 5 Illustrative depiction of infrared Earth vs visible band. Adapted from [9]

1.3.2 Infrared Sensors

At a high level, infrared sensors are categorised into two primary classes: photonic detectors, and thermal detectors; the working concepts are illustrated in Fig. 6.

Photonic detectors utilise the photoelectric effect, and operate based on the interaction of photons (light particles in the infrared band) with the electronic states of a material, causing an electric excitation that can then be measured [11]. Historically, infrared sensors used for horizon detection were typically of this type, exhibiting fast response to thermal change, but requiring costly manufacturing processes and appreciable power and weight requirements. This is primarily due to the need for cryogenic cooling during operation, to reject thermal noise from within the sensor itself [12].

The second infrared sensor class is the thermal detector (commonly found in contactless temperature sensors). This sensor technology has seen significant improvements and miniaturisation within the last few decades due to recent advancements in Micro Electro-Mechanical System (MEMS) manufacturing [11]. Thermal detectors utilise the thermoelectric effect, and operate on the principle of the change in some physical property of the detector material due to the heating effect of absorbed infrared radiation [11]. They typically exhibit slightly slower response to thermal change compared to photonic detectors, but do not require cryogenic cooling; and their small size and weight makes them an appealing fit for adding advanced infrared sensing capabilities for horizon detection to small-satellites.

In the context of this paper, the thermal detector type infrared sensor is investigated, specifically a matrix array of thermopiles.

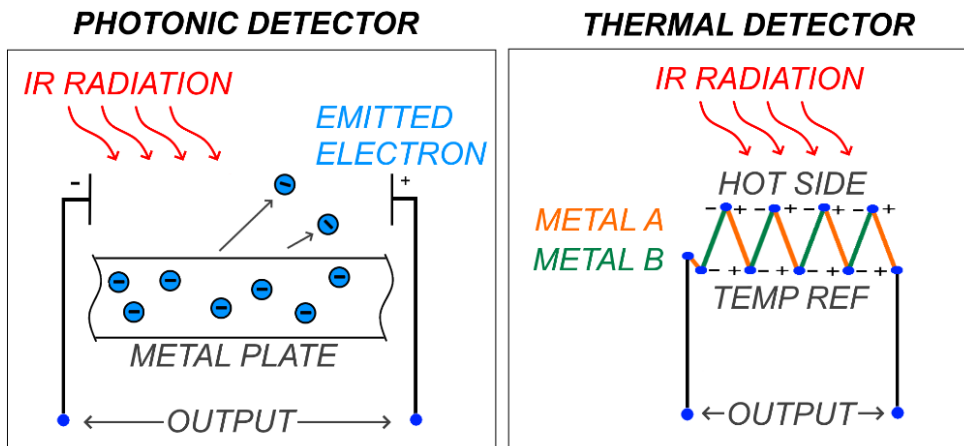


Fig. 6 Illustration of working principles of photonic vs thermal infrared detection

1.3.3 Horizon Detection

The mechanism used by infrared horizon sensors to detect the edge transition differs by implementation, but often involves an infrared sensor of some description which is either: progressively scanned across a certain field of view to detect the change in signal as the scan crosses the horizon edge [13][14]; or multiple static sensors which are positioned around the craft pointing to the location of the horizon transition, their fixed mounting angle is set based on an anticipated orbit altitude.

García Sáez et al. [15] demonstrates a common fixed sensor implementation using four thermopile infrared sensors positioned around the craft and angled to the anticipated visible horizon transition, when the differential between the sensor readings is zero, the local vertical to the planet can be inferred. Similarly, Nguyen et al. [16] demonstrates a novel approach using a trio of thermopiles aligned vertically, the local vertical to the planet is inferred by interpreting the differential between the outputs of the set of sensors as they cross the horizon edge.

The miniaturisation of thermal type infrared detectors through MEMS have also seen a growing interest in the use of multi-element infrared sensor arrays. These can be configured in a designated pattern as shown by Herwaarden [17], where 32 thermopiles are placed in a cross pattern, or the sensor elements can be configured in a matrix which can be used to construct a two-dimensional infrared thermal image of the given scene.

These thermal images have been evaluated for horizon detection with ground-based examples using 32x31 element arrays by Van Rensburg [18] and Wessels [19]; through the use of basic edge detection algorithms, the resulting pixel level thermal edge representing the horizon transition can be identified. However, given these approaches target pixel level guesses at the detected edge, their performance is limited by the number of infrared sensor elements that make up the matrix, *i.e.* the resolution, of the thermal image. This pixel level edge inaccuracy is illustrated in Fig. 7.

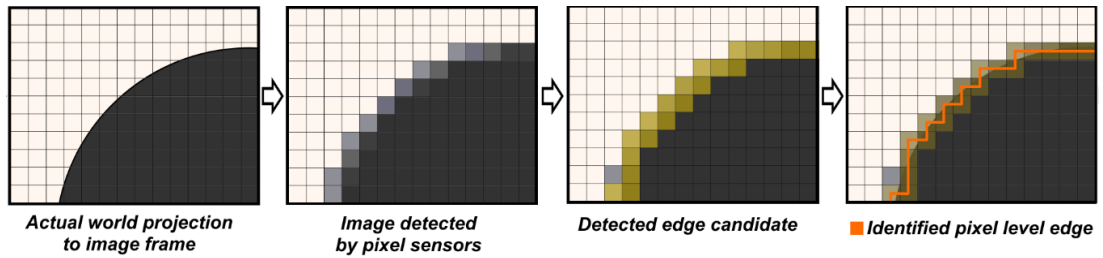


Fig. 7 Edge detection inaccuracy due pixel level edge sequence, *i.e.* from a typical low resolution thermal image

Image based horizon detection has also been thoroughly demonstrated in the visible spectrum. Christian [20] provides a solid introduction to the general geometry of the problem, and further considerations from the perspective of a visible band camera. Braun et al. [21] references and builds on this work, demonstrating an example using a high definition 1920 x 1080p (~2M pixels) GoPro camera; although the approach benefits from a substantially higher pixel count when compared to the typically low-resolution infrared options, the use of the visible band introduces new challenges in detecting the horizon transition. As mentioned previously, these challenges are related to the lack of visible light while the craft is in eclipse behind the Earth, converging lens distortion and corrections, and non-uniformity of the Earth silhouette, for example picking up false edge detections from geological features, cloud cover *etc.*

1.3.4 Sub-Pixel Edge Localisation

Although the challenges of accurate horizon edge detection differ slightly between approaches using visible and infrared bands, there are many common learnings that can be applied to thermal images from adjacent research using visible band cameras. An example of particular interest is the implementation of sub-pixel edge detection algorithms to improve the accuracy of detected edges in low resolution images.

One of the leading methods that shows promising results is the use of the Zernike polynomials, *i.e.* Zernike moments. These polynomials were originally introduced by Frits Zernike in the context of optical aberrations for improving the quality of telescope lenses, and are defined as a set of orthogonal complex polynomial functions bound to the unit circle [22]. These polynomials have since found applications in various fields, including medical imaging, wavefront analysis, image processing, and computer vision. Of note is their application in subpixel edge detection in low-resolution images,

where their mathematical properties enable precise localisation of edges beyond the confines of the standard pixel grid.

In simple terms, different Zernike polynomials can be created based on the generating functions order $[n]$, which describes how features change with distance from the centre of the unit circle, and repetition $[m]$, which relates to how features change with angular rotation around the unit circle. The order and repetition used to generate a Zernike polynomial is typically referenced alongside it, with this paper using the $[Z_{nm}]$ format; the first six unit-circle bound Zernike polynomials are illustrated in Fig. 8.

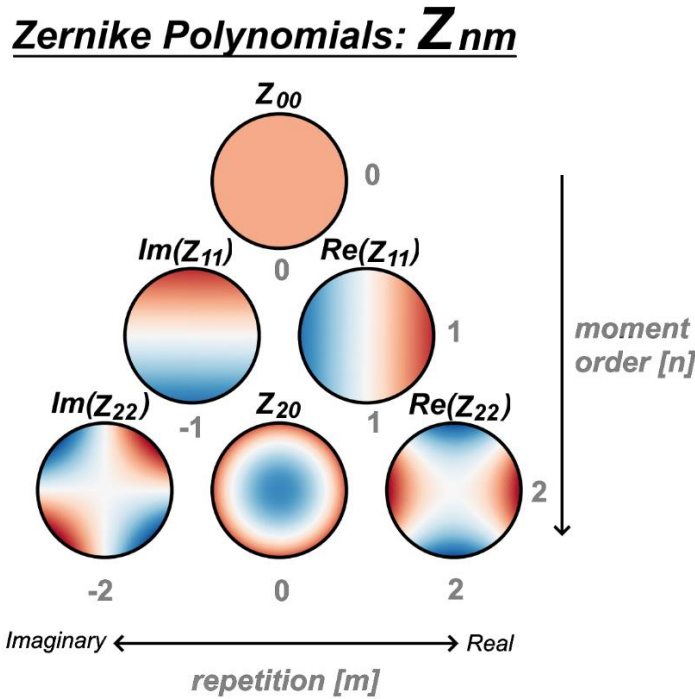


Fig. 8 Illustration of the first six Zernike polynomial aberrations. Adapted from [23]

Each generated Zernike polynomial describes a certain optical aberration, the main aberrations of interest for sub-pixel edge localisation are [24]:

- Horizontal Tilt aberration [$Re(Z_{11})$]: describes tilt / intensity distribution along the x-axis.
- Vertical Tilt aberration [$Im(Z_{11})$]: describes tilt / intensity distribution along the y-axis.
- Defocus aberration [Z_{20}]: describes radial defocus / the spread of intensity about the centroid.

The features of these three Zernike polynomials are used to generate a pixel quantized mask of weights, which is convolved with the image intensity in a patch of pixels surrounding each pixel-level edge guess. The result of this convolution is an image moment that describes how the shape in the image patch is modified by the Zernike aberration, and by analysing the three convolution results, the relative distance and angle of the underlying edge feature can be estimated. From this, a sub-pixel correction vector can be found that adjusts the coordinate of the pixel edge to better align with the underlying shape geometry in the scene.

Christian [24] demonstrates an improved method for applying Zernike moments to increase the accuracy of the detected horizon edge in visible band attitude determination; with the accuracy of the improved Zernike method out-performing all other popular sub-pixel detection algorithms tested.

In the context of this paper, the benefits of using the infrared band for horizon detection will be combined with learnings from sub-pixel edge detection algorithm research in the visible band camera space. This approach aims to improve the sub-pixel edge detection performance of the typically low resolution infrared thermal images. An illustration of a sub-pixel adjustment to the identified pixel level edge is provided in Fig. 9.

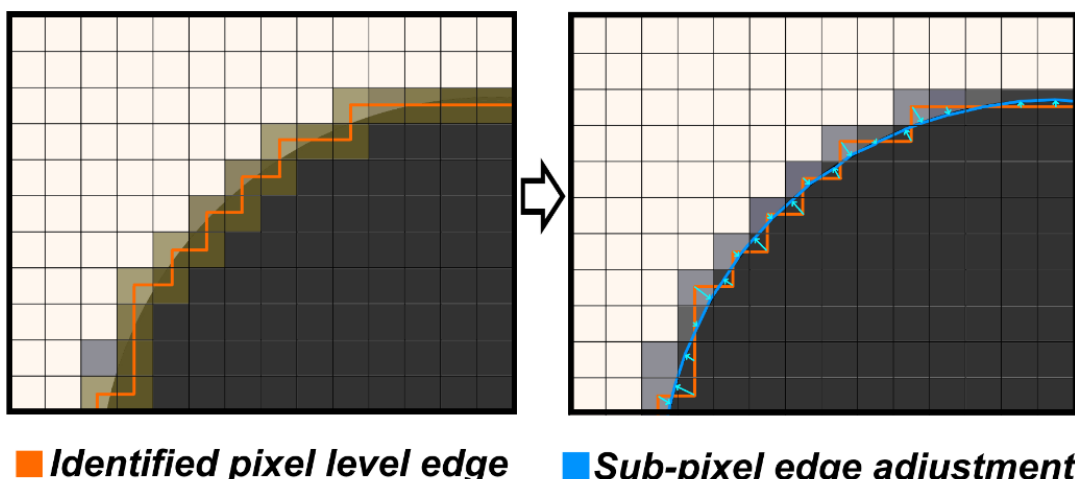


Fig. 9 Illustration of sub-pixel adjustment to detected edge in low resolution thermal image

1.3.5 Geometry & Coordinate Frames

Attaching a topocentric coordinate frame to the spacecraft, illustrated in Fig. 10, such that the z-axis is colinear with the nadir vector and the x, y-plane is tangent to the planet's surface; the angle from the nadir vector to the visible horizon can be determined from orbit altitude [h] and the radius of the Earth [R_E] using Eq. (1).

$$\theta_{hoz} = \sin^{-1} \left(\frac{R_E}{R_E + h} \right) \quad (1)$$

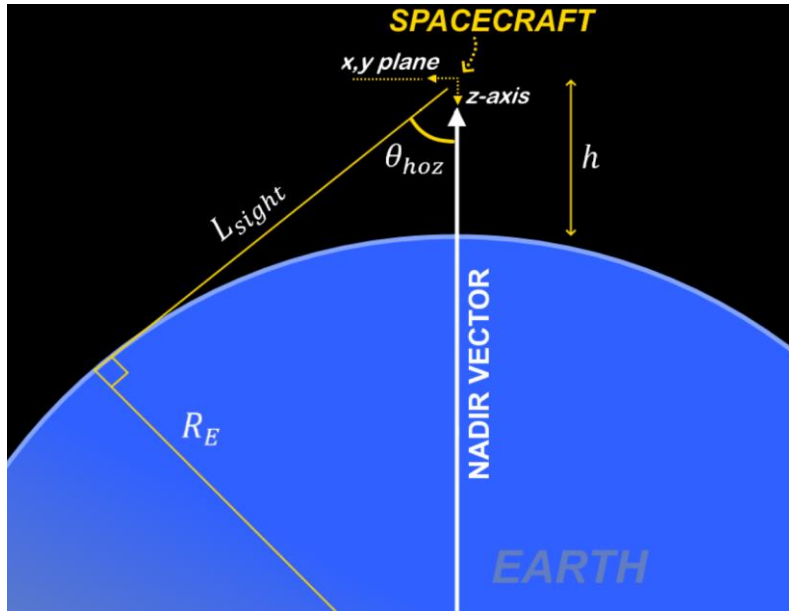


Fig. 10 Geometry of visible horizon transition relative to nadir vector and orbit altitude

With Earth's average radius as 6,378km [5], and considering a typical low earth orbit (LEO) altitude of 700km [5], the angle from the nadir vector to the visible horizon is found to be 64.3°.

Thermal sensing cameras are typically most sensitive to infrared radiation towards the centre of their image frames. For the purpose of this paper, the target mounting position of the horizon sensor on the craft will therefore be aligned with the angle calculated in Eq. (1), such that the top of the horizon edge arc crosses the centre of the image frame during nominal operation. This positioning is intended to also improve the contrast /

edge detection sensitivity of the thermal sensor array, by providing a similar ratio of image area at both temperature extremes of Earth and the background of space.

For the purpose of understanding how the image in object space is projected to the sensor array, the thermal camera is represented using the pin hole camera model with no lens. Using this model, two imaginary parallel image planes can be constructed to represent the world image plane in object space, and its projection onto the spacecrafts infrared sensing array; see illustration in Fig. 11.

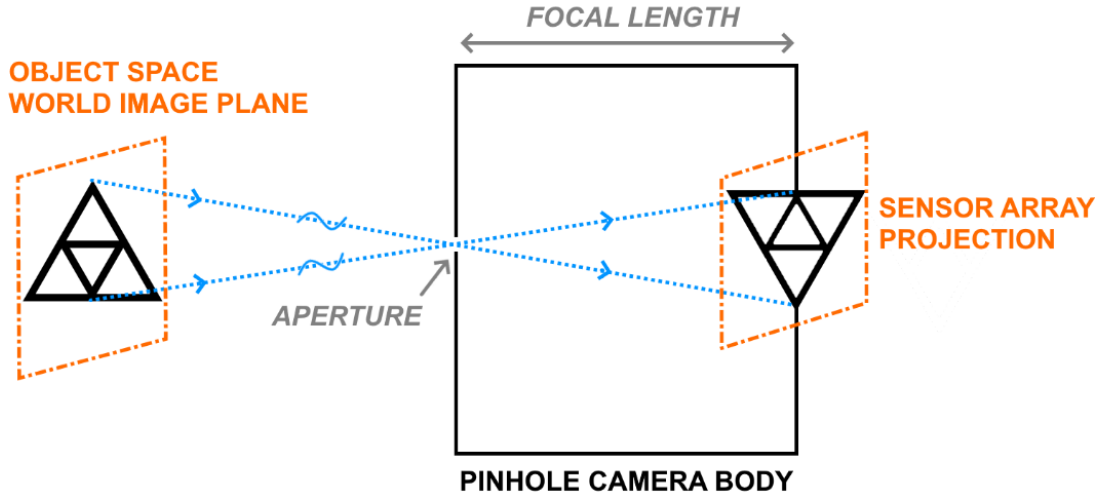


Fig. 11 Illustration of pinhole camera world and projection planes

The size of the world image plane in object space is determined by the sensors field of view, and the planes distance from the sensor at which a suitably sharp image can be produced is based on the camera's depth of field. This is typically assumed to be very large for a pinhole camera, and is related to the cameras f-stop number. Theoretically, the depth of field approaches infinity as the diameter of the pinhole aperture approaches a zero-diameter mathematical point; *i.e.* an ideal model of a pinhole camera [25].

This relationship is linked to the size of the pinhole (aperture) and the sensing arrays distance from the pinhole (focal length); as per Eq. (2).

$$fStop = \frac{focalLength}{pinHoleAperture} \quad (2)$$

As a practical thermal pinhole camera is likely to have a focal length and aperture of a few millimetres each, and considering the comparative scale of the observed planet in object space, the distance of the world image plane can, within reason, be set somewhat arbitrarily. For consistency, the world image plane is positioned at the edge of the visible horizon; *i.e.* L_{sight} distance from the camera under nominal orientation.

To understand how a point in object space is mapped to a pixel coordinate, consider three aligned reference frames (see Fig. 12): one in the object space 3D world frame $[\bar{X}_{\text{world}}, \bar{Y}_{\text{world}}, \bar{Z}_{\text{world}}]$, one in the thermal sensors reference frame $[\bar{X}, \bar{Y}]$, and one in the images pixel coordinate frame $[\bar{U}, \bar{V}]$. Let the associated point in each reference frame be:

$$P_{\text{world}} = [x_{\text{world}} \quad y_{\text{world}} \quad z_{\text{world}}]^T$$

$$P_{\text{camera}} = [x \quad y \quad 1]^T$$

$$P_{\text{pixel}} = [u \quad v \quad 1]^T$$

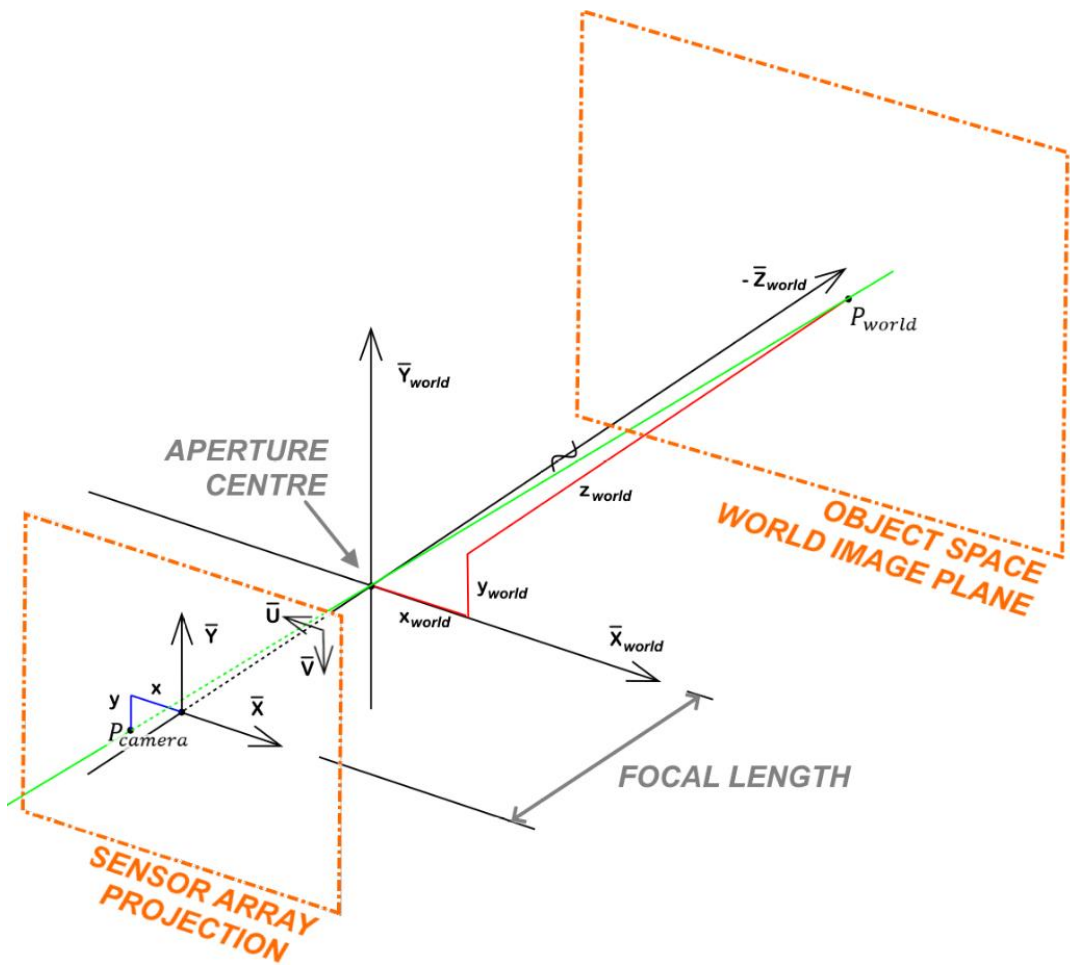


Fig. 12 Assigned pinhole camera coordinate reference frames. Adapted from [26]

The transform matrix that maps $[P_{world} \rightarrow P_{camera} \rightarrow P_{pixel}]$ is based on the physical properties of the specific camera. The two required matrix are the cameras intrinsic calibration and extrinsic position matrix, which are identified during an initial calibration routine. The forward transform is shown in Eq. (3) [27].

$$P_{pixel} = \mathbf{K}_{intrinsic} \cdot \mathbf{M}_{extrinsic} \cdot P_{world} \quad (3)$$

As the sensor array outputs pixel coordinates, we seek to find a transform from pixel space to object space; *i.e.* $[P_{pixel} \rightarrow P_{camera} \rightarrow P_{world}]$. To achieve this, each pixel coordinate is mapped through the inverse of the camera's intrinsic and extrinsic transform matrix, as shown in Eq. (4). As this inverse transform maps 2D pixel coordinates to 3D world coordinates, a scaling factor is used to represent the unknown depth in object space: let $\lambda = z_{depth} = L_{sight}$.

$$P_{world} = \mathbf{M}_{extrinsic}^{-1} \cdot (\lambda * \mathbf{K}_{intrinsic}^{-1} \cdot P_{pixel}) \quad (4)$$

The forward intrinsic transform typically includes a 2D translation, scale, and shear operation defined by the physical properties of the camera [27], its inverse matrix $[\mathbf{K}_{intrinsic}]^{-1}$ maps pixel coordinates to the sensor frame $[P_{pixel} \rightarrow P_{camera}]$.

The intrinsic camera calibration matrix definition is shown in Eq. (5), followed by its inverse in Eq. (6). Each operation is further explained below [27]:

- a) **Translation** $[x_0, y_0]$: shifts optical axis origin to pixel coordinate system and corrects for misalignment of principle axes between planes; *e.g.* if the array of detecting elements is not centrally mounted below the aperture within the sensor housing;
- b) **Scale** $[f_x, f_y]$: scale operation in the x and y direction corrects for focal length and non-uniformity of assumed ‘square’ sensor pixels;
- c) **Shear** $[s]$: adjusts principal axis skew; *e.g.* corrects for tilt of the array of detecting elements in their mounted position within the sensor housing.

$$\mathbf{K}_{intrinsic} = \begin{bmatrix} 1 & 0 & x_0 \\ 0 & 1 & y_0 \\ 0 & 0 & 1 \end{bmatrix} \begin{bmatrix} f_x & 0 & 0 \\ 0 & f_y & 0 \\ 0 & 0 & 1 \end{bmatrix} \begin{bmatrix} 1 & s/f_x & 0 \\ 0 & 1 & 0 \\ 0 & 0 & 1 \end{bmatrix} = \begin{bmatrix} f_x & s & x_0 \\ 0 & f_y & y_0 \\ 0 & 0 & 1 \end{bmatrix} \quad (5)$$

$$[\mathbf{K}_{intrinsic}]^{-1} = \begin{bmatrix} \frac{1}{f_x} & -\frac{s}{f_x f_y} & \frac{s y_0 - f_y x_0}{f_x f_y} \\ 0 & \frac{1}{f_y} & -\frac{y_0}{f_y} \\ 0 & 0 & 1 \end{bmatrix} \quad (6)$$

To correct for the pinhole cameras inherent optical flip, an extrinsic transform is used to rotate 180° about the \bar{Z} axis [$P_{camera} \rightarrow P_{world}$]. As there is no camera translation required, the transform and its inverse are identical, as shown in Eq. (7).

$$\mathbf{M}_{extrinsic} = [\mathbf{R}_{z(180^\circ)} \mid t] = \begin{bmatrix} -1 & 0 & 0 & 0 \\ 0 & -1 & 0 & 0 \\ 0 & 0 & 1 & 0 \end{bmatrix} = [\mathbf{M}_{extrinsic}]^{-1} \quad (7)$$

Continuing from Eq. (4), the expanded transform from pixel coordinates to world coordinates [$P_{pixel} \rightarrow P_{world}$] is shown in Eq. (8).

$$\begin{bmatrix} x \\ y \\ z \end{bmatrix}_{world} = \begin{bmatrix} -1 & 0 & 0 \\ 0 & -1 & 0 \\ 0 & 0 & 1 \end{bmatrix} \left(\lambda * \begin{bmatrix} \frac{1}{f_x} & -\frac{s}{f_x f_y} & \frac{s y_0 - f_y x_0}{f_x f_y} \\ 0 & \frac{1}{f_y} & -\frac{y_0}{f_y} \\ 0 & 0 & 1 \end{bmatrix} \begin{bmatrix} u \\ v \\ 1 \end{bmatrix} \right) \quad (8)$$

1.3.6 Conic Projection of Visible Horizon

While a craft is in orbit, its possible view of the Earth is restricted to the area bound by its visible horizon, approximating the Earth as a sphere, this visible horizon is dependent on orbit altitude, and represents tangent rays from the visible horizon edge transition. These rays form the surface of an imaginary cone, with an apex at the spacecraft's location, and a surface which is tangent to the planet sphere; see Fig. 13, Fig. 14. Imagining the visible horizon as a cone in this way leads to a deeper

understanding of the geometry of the horizon edge when it is projected onto the crafts two-dimensional sensor array, as will be seen further below.

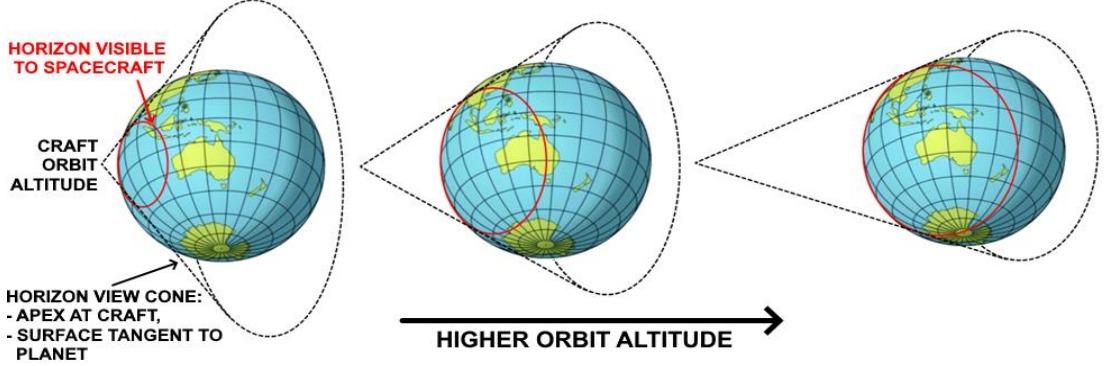


Fig. 13 Circular visible horizon view cone. Adapted from [28]

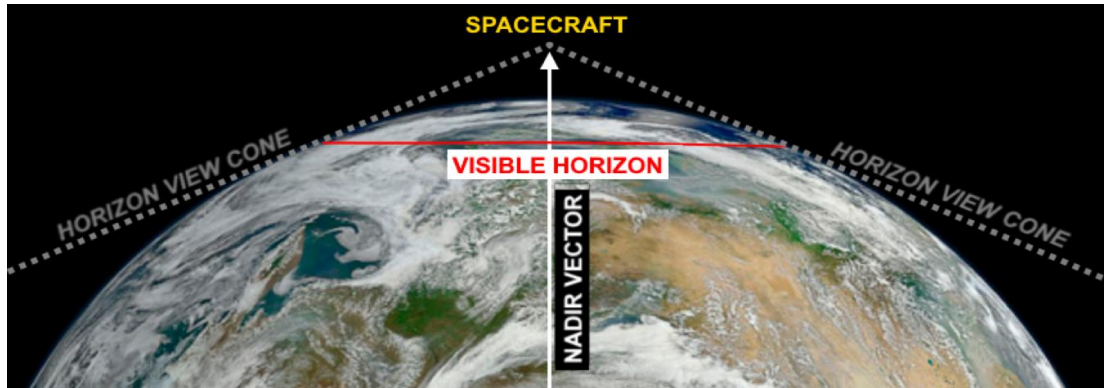


Fig. 14 Side section of a spacecraft's visible horizon view cone. Adapted from [9]

As mentioned in section 1.3.5, the pinhole cameras world image plane in object space will be centrally positioned at the edge of the visible horizon under nominal orientation. A side section illustration of this nominal position is provided in Fig. 15.

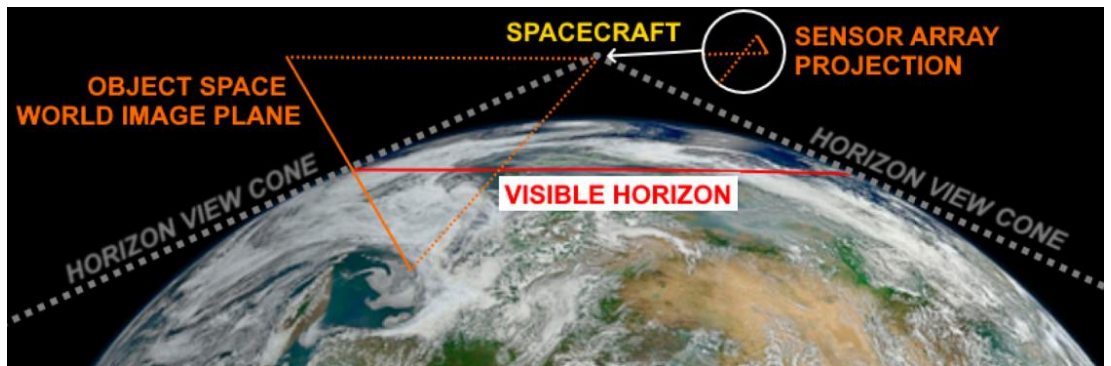


Fig. 15 Side section illustrating pinhole camera projection of world image plane to sensor array, while in nominal orientation. Adapted from [9]

Returning to the concept of the imaginary horizon view cone representing rays to the visible horizon transition (refer Fig. 13). Considering the geometric definition of a conic section, *i.e.* the curve formed by the intersection of a plane and a cone, it may become clear that the cameras object space world image plane that was just created forms a Euclidean plane, that intersects the horizon view cone at some angle based on the camera's orientation. Based on this relationship, it can be inferred that the circular visible horizon on the 3D planet sphere will appear as a conic section once projected onto the cameras 2D image of the scene; an illustration of this phenomenon is provided in Fig. 16.

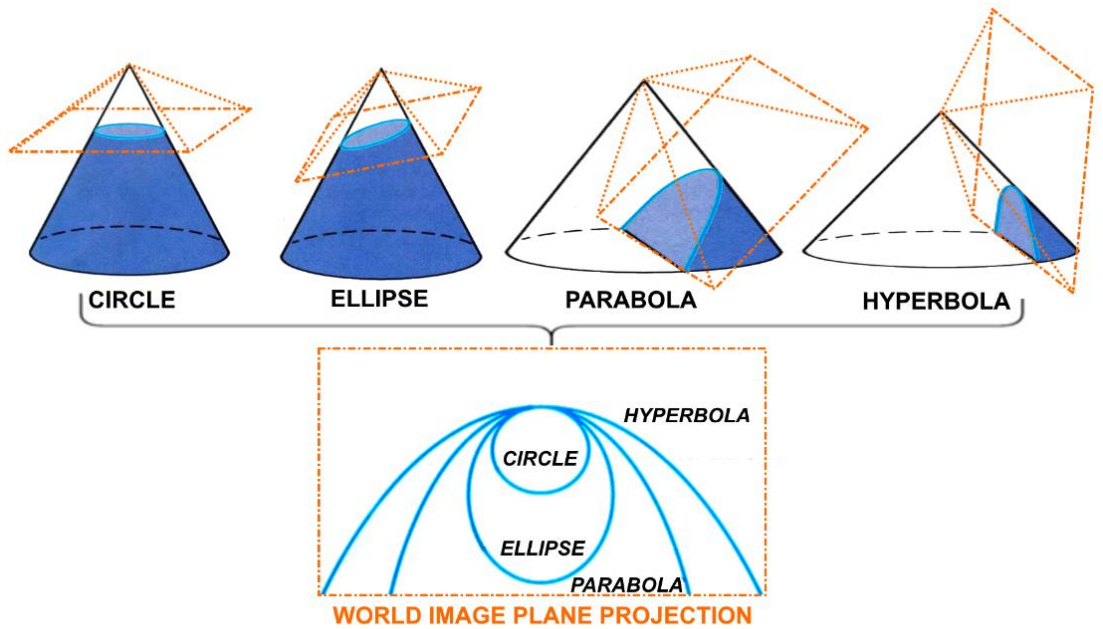


Fig. 16 Illustration depicting how the horizon view cone projects the circular visible horizon to a conic section in the sensors image plane, relative to orientation of sensor

This implies that, from the perspective of the image sensor, the circular horizon edge appears as either a hyperbola, parabola, ellipse, or circle; based on the craft's orbit altitude, the FOV of the sensor, and the orientation of the camera relative to the nadir vector.

Conics sections have a few unique geometric properties that can be exploited; the conic general quadratic equation, Eq. (9) [29], defines all possible conic sections, and by finding a solution that satisfies its definition using the identified edge coordinates, the orientation of the plane used to generate the conic can be inferred; *i.e.* the orientation

of the world image plane in object space, and therefore the current pointing of the crafts sensor.

$$Ax^2 + Bxy + Cy^2 + Dx + Ey + F = 0 \quad (9)$$

Each transformed pixel / sub-pixel coordinate $[x_i, y_i]$ of the identified edge sequence in the image is used to construct a system of equations to solve for the unknown conic coefficients. Eq. (10) shows the system of equations represented in the matrix form of the conic general quadratic equation [29].

A unit length $z_i = 1$ component is amended to each frame coordinate such that the conic general equation can be represented in homogeneous 3x3 matrix form:

$$\begin{bmatrix} x_i & y_i & 1 \end{bmatrix} \begin{bmatrix} A & B/2 & D/2 \\ B/2 & C & E/2 \\ D/2 & E/2 & F \end{bmatrix} \begin{bmatrix} x_i \\ y_i \\ 1 \end{bmatrix} = 0 \quad (10)$$

By solving for the unknown coefficients (*e.g.* using the least mean squares method), the conic type and its parameters can be identified.

Given the camera frame sits at the conic apex, and the world image frame can never intersect this point, the conic is non-degenerate and its type can therefore be inferred using the following conditions:

Let conic discriminant $\Delta = B^2 - 4AC$, then the horizon shape in the image frame is a circle when $A == C \ \&\& B == 0$; an ellipse when $\Delta < 0$; a parabola when $\Delta == 0$; or a hyperbola when $\Delta > 0$.

Conveniently, the conic discriminant is also invariant to rotation and translation of the conic section within the image frame [29].

Geometrically, these conditions for non-degenerate conic section types are based on the relationship between:

- a) The angle $[\beta]$ of the cones surface from its central axis; *i.e.* the angle from the nadir vector to the visible horizon transition. Given a known orbit altitude, β is found trivially from θ_{hoz} in Eq. (1):

$$\beta = \theta_{hoz} \quad (11)$$

- b) The angle $[\alpha]$ between the cutting plane used to generate the conic section and the cones central axis; *i.e.* the angle of the world image plane relative to the nadir vector.

These two angles, illustrated in Fig. 17, form an important relationship with the eccentricity $[e]$ of the generated conic section in Eq. (12).

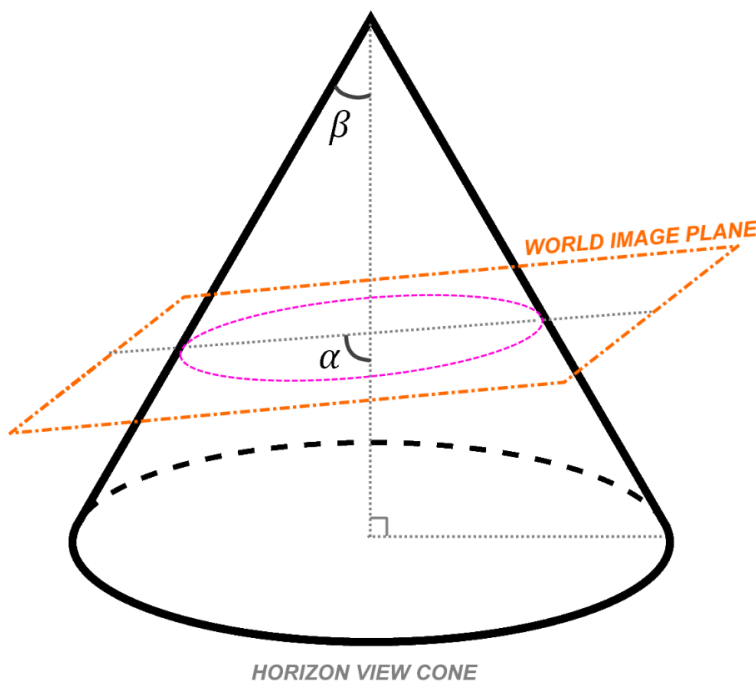


Fig. 17 From the cone's axis, the angle to its surface and the angle of the cutting plane are related to the eccentricity of the generated conic section

$$e = \frac{\cos (\alpha)}{\cos (\beta)} \quad (12)$$

Taking the determinant of the 3x3 matrix in Eq. (10), let $\eta = 1$ when the determinant is negative, and $\eta = -1$ when the determinant is positive; then, the eccentricity of the identified conic section can be found with Eq. (13) below [29].

$$e = \sqrt{\frac{2\sqrt{(A-C)^2 + B^2}}{\eta(A+C) + \sqrt{(A-C)^2 + B^2}}} \quad (13)$$

With a valid solution to the conic quadratic equation and a known orbit altitude, the angle α of the cutting plane relative to the nadir vector can be found using Eq. (12) and Eq. (13); *i.e.* $(90^\circ - \alpha)$ is the angle of the cameras bore axis from the nadir vector.

To find the rotation of the horizon arc relative to the sensors frame of reference, the conics rotation within the image frame also needs to be identified. Given a camera reference frame with an origin at its centre, the conics rotation within the frame can be found from the cross-term xy on the B coefficient of Eq. (9). The presence of this term indicates a skew of the generated conic, and the counter-clockwise rotation $[\varphi]$ from the cameras x-axis that generated this skew in symmetry can be solved for using Eq. (14) [29].

$$\varphi = \frac{1}{2} \tan^{-1} \left(\frac{B}{A - C} \right) \quad (14)$$

By identifying key parameters of the conic section, the rotation of the conic relative to the cameras reference frame $R(z)_{sensorFrame}$, and the angle of the conic cutting plane relative to the nadir vector $R(x')_{sensorFrame}$ can be calculated. From this, the location of the nadir vector relative to the sensor, and therefore the crafts relative attitude to the planet, can be determined.

2. Method & Design

To assess the function of the thermopile imaging array in orbital navigation, a prototype infrared horizon sensor and proxy orbital view test stand was designed and built to evaluate its utility.

The choice to build a physical prototype for testing has several advantages over relying solely on simulations or mathematical models. While simulations provide valuable insights, real-world prototypes capture the complexities and unpredictability of the environment that mathematical models may overlook. Prototypes also allow an observation of the physical interactions of the integrated system, such as interface of components, material properties, and other environmental factors which are often difficult to model accurately.

Real-world testing provides hands-on feedback, enabling quicker adjustments and refinements, and more opportunities for deeper learning experiences as unforeseen challenges are faced and overcome. Prototypes can also reveal practical issues related to manufacturing tolerances, and other user / environmental interactions that may not be evident in simulation.

The design methodology for the development of the prototype infrared horizon sensor and proxy orbital view test stand is detailed in the following sections, and was driven by the overarching project design requirements; defined in the Requirements Verification Matrix on the following page.

2.1 Requirements Verification Matrix

TABLE 1 Project Requirement Statement and Verification Criteria

Req. No.	Project Area	Requirement Statement	Verification Method	Success Criteria
P-1	Horizon Sensor Prototype	The infrared sensor shall have sensitivity within the preferred 14 to 16 μ m infrared radiation band detectable from orbit.	Inspection	The spectral sensitivity of the sensor is within the stated infrared band, confirmed via manufacturer datasheet.
P-2	Horizon Sensor Prototype	The prototype shall incorporate a matrix of thermal detector type infrared sensors to construct a thermal image of the given scene.	Inspection	<ul style="list-style-type: none"> 1. The infrared imaging sensor is a matrix of thermal detector type sensors (<i>e.g.</i> a thermopile matrix), confirmed via manufacturer datasheet. 2. The prototype transfers the captured thermal image of a known scene of infrared emitting objects to host machine for inspection. 3. Taking an image from the same location using a calibrated thermal camera; by visual inspection, the pose of features in both images are correlated and represent the scene of infrared emitting objects.
P-3	Horizon Sensor Prototype	The prototype shall internally process images captured from the thermal camera and perform coarse edge detection to identify candidate edge sequences within the image.	Inspection	<ul style="list-style-type: none"> 1. The prototype transfers the thermal image and identified edge coordinates to host machine for inspection. 2. The identified edge sequences visually correlate to intensity transitions in the underlying thermal image.
P-4	Horizon Sensor Prototype	The prototype shall apply a sub-pixel edge correction method to refine the accuracy of the identified pixel-level edge sequence.	Inspection	<ul style="list-style-type: none"> 1. The prototype transfers the captured thermal image, original edge coordinates, and sub-pixel adjustments to host machine for inspection. 2. By visual inspection, the sub-pixel edge correction is more closely aligned to the true shape of the imaged feature, vs the original pixel-level edge.

P-5	Horizon Sensor Prototype	The prototype shall attempt to fit a conic section to the identified edge sequence and estimate the coefficients of its general quadratic equation.	Test	<ol style="list-style-type: none"> 1. The prototype captures an image of the test stand and transfers the edge coordinates and conic quadratic coefficients that were identified to host machine for inspection. 2. The identified conic represents the configuration of the test stand, and is a hyperbola with eccentricity between 1.94 (800km altitude) and 2.25 (600km altitude). <u>Configuration of test stand:</u> LEO altitude of 600-800km from a $55^\circ \times 35^\circ$ FOV sensor at nominal orientation (refer Fig. 15).
P-6	Horizon Sensor Prototype	The prototype shall perform attitude determination by estimating the relative location of the nadir vector based on the parameters of the identified conic.	Test	<ol style="list-style-type: none"> 1. The prototype captures images of the test stand and transfers the calculated sequence of rotations required to align the sensors bore axis to the nadir vector, within $\pm 5^\circ$ of its expected location; i.e. roll about sensors optical axis $[R(z)_{sensorFrame}]$, then pitch along the perpendicularly aligned coordinate frame axis $[R(x')_{sensorFrame}]$. 2. Rotating the horizon sensor about its bore (roll) by 10° increments in the CW and CCW directions changes the magnitude of the calculated conic rotation in the corresponding direction and within $\pm 5^\circ$ of the physical rotation. 3. The calculated angle of the conic cutting plane $[\alpha]$ corresponds to the test stands conic shape: $\alpha = 26^\circ \pm 5^\circ; \therefore bore\angle nadir = 64^\circ \pm 5^\circ$
P-7	Horizon Sensor Prototype	The prototype shall accept and operate from an unregulated 4-18V DC supply; i.e. analogous to a typical direct battery supply from the Electrical Power Subsystem (EPS) of a CubeSat.	Test	Incrementally vary prototypes supply in 1V steps within expected input range and confirm correct board operation via continuous program serial output to host machine.

P-8	Horizon Sensor Prototype	The prototype shall interface externally via serial for calculated outputs, sensor state flags, and debug messages; <i>i.e.</i> emulating rudimentary data transfers to the CubeSat's ADCS.	Inspection	The prototype interfaces and sends stated data to connected port on host device via serial UART.
P-9	Test Stand	A proxy infrared scene of Earths conic horizon shall be built that approximates what is seen from an LEO orbit altitude of 600-800km, with a $55^\circ \times 35^\circ$ sensor FOV, while in the nominal orientation (refer Fig. 15).	Test	<ol style="list-style-type: none"> 1. Confirm by measurement horizon arc represents a conic with eccentricity between 1.94 (800km altitude) and 2.25 (600km altitude); <i>e.g.</i> a projective discriminant $\rho = 0.53 \pm 0.01$ with conic apex [D1] of 21-24mm for a 380mm span simulate scene, refer Eq. (17). 2. Confirm a distinct thermal edge between the simulated Earth and space background using calibrated thermal camera; $\Delta\text{C} \geq 200^\circ\text{C}$.
P-10	Test Stand	While viewing the proxy infrared scene, the horizon sensor prototype shall be centrally mounted to a controllable pitch and roll gimbal with a positional pitch and roll accuracy resolution $<0.5^\circ$.	Inspection	Actuators directly tied to the pitch and roll structures are within positional accuracy tolerance, confirmed via manufacturer datasheet.
P-11	Test Stand	The proxy infrared scene shall extend to allow the prototype a minimum 90° ($\pm 45^\circ$) roll and 10° ($\pm 5^\circ$) pitch window without exceeding the edge of the simulated view.	Inspection	With the sensor centrally positioned 25cm from the thermal face of the test stand, the FOV is bound within test stand at extents of roll and pitch allowance (accounting also the diagonal of the sensors image under roll conditions); confirmed by visual inspection of intensity uniformity at edges of generated thermal image.

2.2 Horizon Sensor Prototype

The development of the prototype infrared horizon sensor was organised by hardware and software design considerations, which are detailed in the following sections.

2.2.1 Hardware

In addition to the overarching project verification requirements, the hardware design of the horizon sensor was approached with the context of a space bound craft, specifically a CubeSat; and was focused primarily on prototype component selection, thermal, electrical and environmental considerations, and PCB design best practices. The design methodology relating to each key aspect of the prototype's hardware is detailed in the sub-sections below:

2.2.1.1 Thermal Sensor

The infrared sensor class selected for the prototype was a thermal detector type sensor. In the context of infrared horizon detection for small-satellites, this sensor technology was chosen over photonic detection due to its smaller general size, cost and weight, availability, and comparative simplicity (*e.g.* not requiring external cooling).

To generate a thermal image of the scene, a packaged matrix of thermopiles was chosen for the prototype; specifically, the Melexis MLX90640-BAB [30]. The selected sensor has a $55^\circ \times 35^\circ$ FOV, and 768 thermopile infrared sensing elements that make up the 32x24px thermal image. Although a sensor with a higher resolution would have been preferred, this detector was selected as a best fit considering also the constraints of project budget and availability.

2.2.1.2 Control Unit

As the resource usage of components within a small-satellite are of key importance, a control system which uses power as efficiently as practical was preferred. The microcontroller is likely to be a key contributor to the overall resource usage of the final horizon sensor, it was therefore decided to target a low-power ARM based offering from STMicroelectronics (STM). The preference for STM was also related to

the authors previous familiarity with the STM32 environment, and general domain knowledge of the platform from colleagues at Curtin University.

The selection of chip was based around a number of factors, including a preference for a USB recognised device for serial debugging, the specification of inter-chip communication protocols (SPI, I2C *etc.*), and a hardware accelerated Floating-Point arithmetic Unit (FPU) to process the sensors floating point precision output.

As per the MLX90640 datasheet [30], the thermal sensor outputs a 768-element float array of the image via I2C (4 bytes \times 768 elements \approx 3.1KB image); considering the horizon sensor program may require multiple copies of the image as it is processed, plus an overhead for the program itself and any other dynamic runtime flash requirements, a microcontroller with a large allocation of memory was targeted.

Based on the above considerations, the 512KB flash memory Arm Cortex-M4 STM32-L4-52CE microcontroller was selected to control the horizon sensor prototype.

Precise scheduling and timekeeping are essential for the correct operation of any space-bound crafts attitude control system. While microcontrollers typically have built-in oscillators that can be referenced for basic time keeping purposes, they are generally less accurate when compared to external hardware, and may exhibit long-term stability issues / drift due to low component tolerances, and sensitivity to changes in temperature [31].

For the prototype, the microcontrollers clock reference was configured to operate from a set of external high precision piezoelectric crystals, located on the PCB in close proximity to the microcontroller. The frequency of the selected low-speed external (LSE) and high-speed external (HSE) clocks has been adapted from work by [32]. The HSE clock is responsible for core processing functions that require speed and performance, while the LSE clock provides the controller an accurate real-time clock (RTC) and an energy efficient timing reference while in low-power states.

The choice to use external timing crystals was expected to enhance the overall reliability of the controller's timekeeping accuracy.

2.2.1.3 Power Regulation

The decision to power the prototype from an unconditioned supply was intended to approximate the variable battery source typically available to sensors from a direct connection through the CubeSats Electrical Power Subsystem (EPS); for example, LiPo batteries in a 1S to 4S configuration.

The unregulated 4-18V DC supply to the board was conditioned using a switch-mode regulator circuit; this was selected based on the anticipated component draw, voltage input range requirements, and the general high conversion efficiency of switch-mode regulation. The circuit was designed around the TPS560430 IC, which uses Pulse Width Modulation (PWM) to efficiently produce a stable 3.3V source for all components on the PCB; with an output capacity of 600mA continuous current, vs a max estimated board consumption of ~150-250mA.

Decoupling capacitors were also placed in close proximity to supply inputs of key components, such as the microcontroller and thermal sensor, to ensure a stable voltage reference was available. A selection of capacitances was chosen to dampen a wider range of perturbating frequencies in the supply.

2.2.1.4 PCB Design

Thermal management was also a key consideration in the PCB's design. Unlike terrestrially, the lack of atmosphere for convection in orbit means heat generated by components on the PCB can only be dissipated via conduction and radiation.

The prototype was designed as a two-layer PCB. The back copper ground plane layer provides a highly conductive path for all common voltage references, and a radiative surface / thermal sink for heat generating components, such as the voltage regulation circuitry and ICs.

The board was designed with two primary trace widths based on the type of connection being made; the electrical calculations for this are in Appendix C. To reduce voltage-drop, power and ground nets were routed with a larger 0.4mm trace, with a capacity for ~1A at 10°C rise over a 50mm run. Signal lines were routed with a thinner 0.25mm

trace to reduce line capacitance, and the potential for crosstalk between communication and reference links (~350mA capacity at 2°C rise over 50mm). Consideration has also been given to route signal traces away from power nets where practical, and each signal line is spaced at least 0.75mm (3x the trace width as a rule of thumb) from other signal lines.

In order to reduce the potential for external interference, *e.g.* from other hardware inside the CubeSat or the external space environment, ensuring adequate ground shielding was an important consideration in the layout of the PCB. To achieve this, additional grounded top layer copper pours were also placed around key inter-board communication / reference / timing signal traces and components. The PCB layout for the prototype has been provided in Appendix B.

To simplify the design of the controllable roll-pitch gimbal the PCB will be mounted to for testing, the thermal sensor is centrally positioned on the PCB such that planar rotations to the board are about the optical bore of the detector; refer location Fig. 18. Components on the horizon sensor PCB are sized primarily as Surface-Mount Device (SMD), this was chosen as a balance between miniaturisation and ease of assembly. The dashed area marked on the PCB in Fig. 18 represents the key operating components of the horizon sensor, with additional hardware and area on the PCB related to prototype specific mounting, and debug / auxiliary functions.

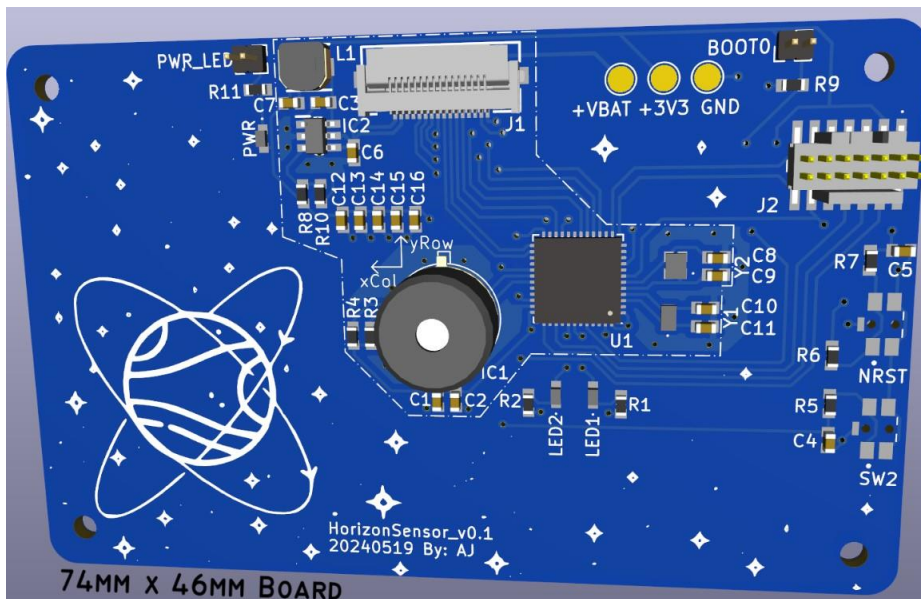


Fig. 18 Prototype PCB render, marked zone indicates key horizon detection hardware

All components on the prototype were mounted to a single side of the PCB. Although a smaller footprint is likely possible in a future two-sided revision, the prototype's single sided design was chosen to simplify the manual hot plate reflow soldering process steps that followed assembly (Fig. 19).

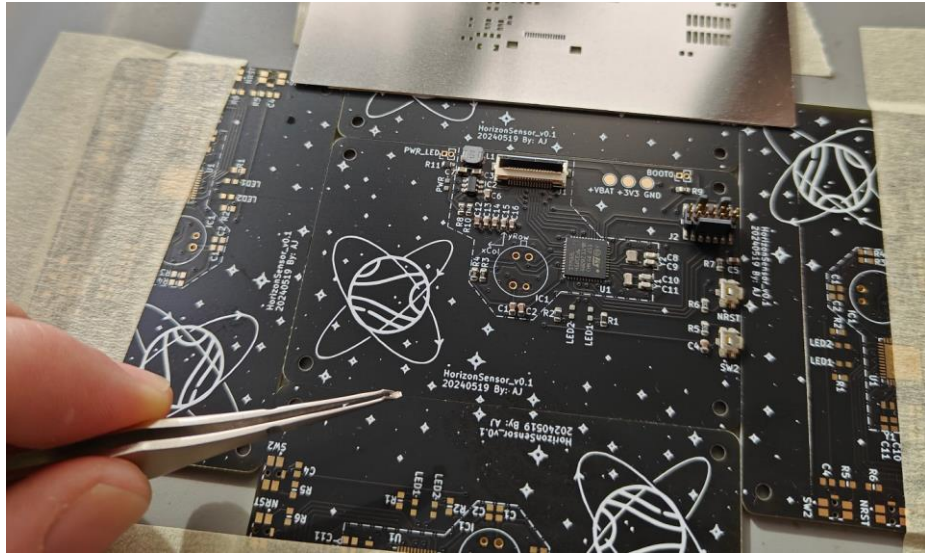


Fig. 19 Component placement prior to reflow soldering

2.2.1.5 External Interface

External interface to the microcontroller is via two connectors, a primary Molex ribbon cable termination [J1], and a secondary STDC14 debug header [J2].

The primary ribbon termination can supply unregulated power to the board, and allows interface with the microcontroller via serial UART, SPI, and I2C; additional hardware interrupt lines were also configured to allow inbound and outbound interrupt triggers.

The interface pinouts can be found on the PCB electrical schematic in Appendix A.

The primary ribbon connection and board formfactor of the initial horizon sensor PCB is designed to interface with the bolt mounting pattern and CubeSat SPI payload connector of BinarX-Curtin [33].

Three auxiliary indication LEDs and a number of voltage reference test points were also included on the prototype for debugging purposes. Of the included LEDs, two are controlled by the microcontroller to indicate device state / status, and one which denotes conditioned power being generated locally on the board.

Additionally, two momentary switches were included for device reset and other auxiliary functions; *e.g.* initiating calibration routines, selecting device modes during testing *etc.* The assembled prototype horizon sensor PCB is shown in Fig. 20.

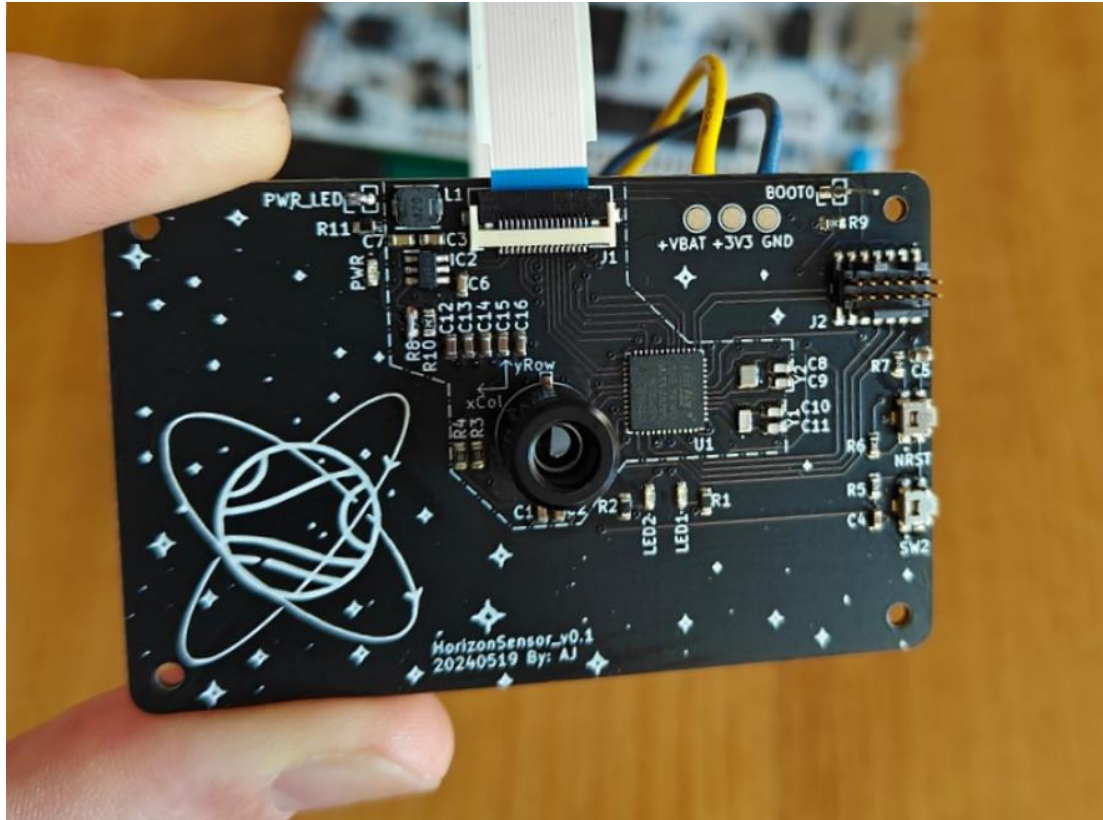


Fig. 20 Assembled horizon sensor prototype PCB

2.2.2 Firmware

A common approach to orbital attitude determination in image-based horizon sensors involves fitting an accurate conic section to the projected horizon edge transition. By identifying the parameters of the conic section quadratic equation, the location of the nadir vector relative to the crafts sensor can be estimated.

To guide the devices firmware development, the following high-level set of tasks was formulated based on the project requirements in 2.1.

A flowchart illustrating the program execution is also provided in Appendix D.

1. Interface with the infrared sensor and capture a thermal image of the scene from a known location relative to the crafts frame of reference;

2. Perform image pre-processing to improve the performance of the edge detection algorithms;
3. Apply a coarse pixel-level edge detection method to identify edge candidates within the image;
4. Filter the identified edge candidates such that strong interlinked edges of a certain sequence length are identified;
5. Improve the accuracy of the pixel-level edge sequence candidates by applying a sub-pixel edge correction;
6. Transform the adjusted sub-pixel coordinates from the image frame to the object space world frame;
7. Based on a known FOV and orbit altitude, attempt to fit the related horizon edge conic projection;
8. Use the identified conic parameters to estimate the translation and rotation of the conic within the image frame; *i.e.* relates to the roll angle about the cameras principal bore to align the frames coordinate axis to a plane with the nadir vector;
9. Use the conic parameters to estimate the angle of the conic cutting plane; *i.e.* relates directly to the angle between the cameras principal bore axis and the nadir vector;
10. Interpret result from 8, 9 to determine horizon sensors orientation relative to the nadir vector; *i.e.* relates the attitude of the spacecraft relative to the planet;
11. Transfer the horizon sensors resulting output to host device via serial; *i.e.* analogous with a rudimentary data transfer to the spacecrafts ADCS.

As of writing, traditional feature rich computer vision (CV) libraries such as OpenCV do not currently have widespread support for low-power Arm based microcontroller platforms. Additionally, these libraries are commonly targeted to hardware platforms with substantially more available memory than is typical of a low-power microcontroller (*e.g.* an estimated library overhead of ~500KB to 1MB or more). As the anticipated image processing requirements seemed relatively straightforward, and memory usage was of key importance, it was decided that simple CV functionality may be able to be achieved using low-level matrix-based maths libraries.

To manage the underlying matrix manipulations, Eigen [34] was selected as a foundational linear algebra library to build upon. The choice to use this library is based on the nature of its open-source licence, the authors previous familiarity with the library, its general execution performance, and the libraries light-weight memory requirements (*e.g.* an estimated library overhead of ~50KB to 100KB).

Each 32x24px thermal image is represented in software by a two-dimensional float matrix; with the value in each cell representing the intensity detected by the thermopile sensor at that pixel coordinate.

In order to use the limited memory of the microcontroller as efficiently as practical, the primary image matrix and other key data structures were allocated to stack memory for the life of the program at device startup. To avoid unnecessary copying operations, the program's various processing functions were configured as 'pass-by-reference', allowing them to operate directly on the location of the pre-assigned memory. Additionally, to minimise redundant storage of data, object relationships and other ordered structures (such as connected sequences of edges in the image *etc.*) were managed using pointers to the static memory address locations of the underlying data.

Using this matrix-based approach, commonly known computer vision algorithms can be applied to the matrix representation of the thermal image. The computer vision C++ library that was built for this project is available for collaboration on GitHub at mtxCV [35].

2.2.2.1 Thermal Camera Interface

The ARM microcontroller receives images from the Melexis infrared sensor via a fast-mode plus (1MHz) I2C interface. A custom library was built to port the manufacturers API via the STM32 I2C Hardware Abstraction Layer (HAL) functions.

Due to the way the Melexis sensor processes readings from each of the thermopile pixel sensors, the thermal image is received from the sensor in two distinct subframe arrays. By combining both subframes and applying calibration factors, a thermal image of the infrared intensity in the scene can be constructed.

Since the primary concern of the infrared horizon sensor is in discerning distinct shape and not accurate measurement of temperature, the sensors pixel readings were interpreted in relative terms.

To improve the programs execution speed as the image was processed, the floating-precision intensity values of the thermal image were quantized with a normalisation and rescale to a scalar integer range.

2.2.2.2 *Image Pre-Processing*

As the performance of edge detection algorithms can be sensitive to noise in the image, a Gaussian blur was applied to smooth out small variations in pixel intensity. This step was chosen to reducing high frequency noise in the image, improving the edge detection algorithms effectiveness by reducing the impact of errant pixel sensor readings, and focusing on the more prominent underlying edge features in the scene.

To reduce the number of required matrix calculations, the Gaussian blur is applied to the image using separable convolution. The selected Gaussian row and column vectors are shown in Eq. (15), and were decomposed from a unity sum 5x5 Gaussian kernel generated with a standard deviation $\sigma = 1.1$.

$$G_x = G_y^T = [0.070766 \quad 0.24446 \quad 0.369546 \quad 0.24446 \quad 0.070766] \quad (15)$$

All convolutions were applied using mirrored borders; that is to say, when the convolution kernel processes a seed pixel near the border of the image, and the kernel would exceed the image bounds, the image pixels are mirrored to fill the area of the kernel not bound to the image. This approach was taken so the convolved result was the same dimensions as the original image passed to the function, and allowed a pseudo accurate representation of the convolution at the bounds of the image.

Additional optional image pre-processing functions were also included to aid the effectiveness of the edge detection algorithm, as required. These functions aim to improve the contrast in the image and make edges more distinguished; for example,

suppressing pixel intensities within a certain ratio of the image's intensity range, and equalising the histogram of the pixel intensities in the image.

2.2.2.3 Coarse Edge Detection

Identifying coarse edges in the image was achieved using an implementation of the Canny edge detection algorithm [36]. The image intensity gradients in the x and y-axis directions were first identified using a convolution with the 3x3 Sobel kernels shown in Eq. (16).

$$S_x = S_y^T = \begin{bmatrix} -1 & 0 & 1 \\ -2 & 0 & 2 \\ -1 & 0 & 1 \end{bmatrix} \quad (16)$$

Analysing the intensity gradient of each pixel's eight neighbours, trigonometry was used to find the gradient magnitude and direction of highest intensity change; *i.e.* a vector field representing the rate of change in pixel intensity across the image.

The expectation is that prominent edges will be perpendicular to areas in the image with the highest local rate of intensity change; *i.e.* the local peaks in the gradient magnitude vector field are the prominent edges in the image; an example of the gradient magnitude vector field represented as a 3D surface is illustrated in Fig. 21.

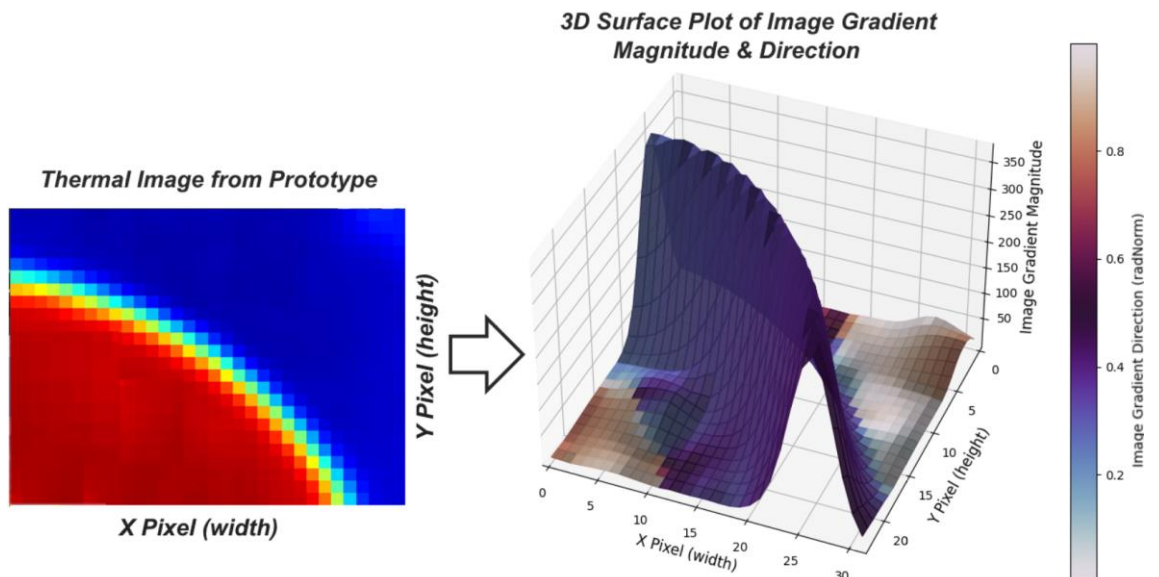


Fig. 21 Illustration of image intensity gradient field as 3D surface, used to identify prominent edges in the image

To refine the identified edges in the image, non-maximum gradient suppression was applied by suppressing any pixels where the rate of intensity change in the directions of the gradient vector is higher than the current pixels intensity gradient. When the angle of a gradient vector bisects neighbouring pixels in the suppression step, the intensity gradient that is assessed is an interpolation between the bisected pixels based on the vectors relative angle between them. This resulted in the identification of the thin prominent edges in the image.

A dynamic gradient threshold was implemented to flag each prominent edge candidate as either a weak or strong edge, which is stored in an edge image mask representing edge candidates in the image. Taking the images highest gradient magnitude, the implementation assigns a strong edge when a pixel's gradient is greater or equal to 70% of this value, and a weak edge when the pixels gradient is less than 70% but greater or equal to 30% of this value. These dynamic ratios were estimated through experimentation, and allow the identification of edges across a varied range of image contrasts.

To identify connected sequences of edges in the image, edge tracking via hysteresis was used with an implementation of the Breadth First Search (BFS) algorithm [37]. The BFS algorithm traverses the image edge mask and begins a sequence when it finds a strong edge candidate, once a sequence is started, each subsequent pixel edge must remain a weak edge or higher to be included in the sequence. Note that the implemented BFS traversal does not assess the outer single pixel border of the image due it not having eight image-bound pixel neighbours. This results in a single pixel border missing from the identified edge contour, which was deemed acceptable in the context of overall edge shape accuracy, vs implementing a mirrored edge approach. As the horizon edge is expected to traverse a large portion of the imaged scene, an edge sequence minimum length constraint of 10 pixels was also applied. This is intended to promote the identification of long interconnected strong edge sequences in the image; *i.e.* prominent edge contours representative of the planet's horizon in the scene.

2.2.2.4 Sub-Pixel Edge Correction

To refine the accuracy of the identified pixel-level edge, a sub-pixel edge correction was calculated for each of the edge coordinates in the contour using the Zernike moments. This approach was adapted to infrared detection from research in the visible band camera space [24]. Taking each coordinate in the identified edge contour as a seed, a 7x7 image patch centred on the seed pixel is extracted from the image and convolved with the pre-calculated Zernike tilt and defocus aberration mask kernels (Z_{11} and Z_{20}).

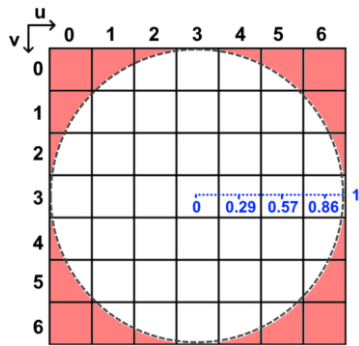


Fig. 22 Illustration of 7x7 image patch with pixel coordinates (u, v), and overlayed unit circle indicating the white area in which the Zernike polynomials are defined

As briefly discussed in 1.3.4, the Zernike polynomials are only defined within the unit circle; therefore, the outer weightings of the Zernike mask kernels were adjusted based on the relevant area of each pixel which is bound within the inscribed unit circle. An illustration of the unit circle's defined area overlayed on the 7x7 image patch is provided in Fig. 22 above. The pixel quantized and unit circle adjusted versions of the tilt and defocus 7x7 Zernike mask kernels are illustrated in Fig. 23.

$\text{Re}(Z_{11})$							$\text{Im}(Z_{11})$							Z_{20}						
0	-0.015	-0.019	0	0.019	0.015	0	0	-0.022	-0.057	-0.069	-0.057	-0.022	0	0	0.023	0.039	0.04	0.039	0.023	0
-0.022	-0.047	-0.023	0	0.023	0.047	0.022	-0.015	-0.047	-0.047	-0.047	-0.047	-0.047	-0.015	0.023	0.027	-0.013	-0.026	-0.013	0.027	0.023
-0.057	-0.047	-0.023	0	0.023	0.047	0.057	-0.019	-0.023	-0.023	-0.023	-0.023	-0.023	-0.019	0.039	-0.013	-0.053	-0.066	-0.053	-0.013	0.039
-0.069	-0.047	-0.023	0	0.023	0.047	0.069	-0.057	-0.047	-0.023	-0.023	-0.023	-0.023	-0.019	0.04	-0.026	-0.066	-0.079	-0.066	-0.026	0.04
-0.057	-0.047	-0.023	0	0.023	0.047	0.057	-0.057	-0.047	-0.023	-0.023	-0.023	-0.023	-0.019	0.039	-0.013	-0.053	-0.066	-0.053	-0.013	0.039
-0.022	-0.047	-0.023	0	0.023	0.047	0.022	0	0.019	0.023	0.023	0.023	0.023	0.019	0.023	0.027	-0.013	-0.026	-0.013	0.027	0.023
0	-0.015	-0.019	0	0.019	0.015	0	0	0.015	0.047	0.047	0.047	0.047	0.015	0	0.023	0.039	0.04	0.039	0.023	0
0	-0.015	-0.019	0	0.019	0.015	0	0	0.022	0.057	0.069	0.057	0.022	0	0	0.023	0.039	0.04	0.039	0.023	0

Fig. 23 Zernike 7x7 tilt and defocus aberration mask kernels

The choice to use a 7x7 kernel over a different odd numbered size was based on the thermal image's low resolution, and finding a balance between the amount of scene information used for sub-pixel adjustment, and the required matrix computations. As each pixel contains averaged information about a comparatively wide section of the given scene, the three-pixel buffer around each pixel edge coordinate was chosen to aid the accuracy of the sub-pixel correction, by providing the Zernike polynomials more information about the underlying shape features in the scene.

The result of the image patches convolution with each of the three Zernike polynomials provides information about how the intensity in the patch surrounding the edge is modified by the horizontal / vertical tilt, and defocus aberrations.

Adapting the equations suggested by [24], the resulting convolutions were fit to a simple ramp edge model representing the transition of intensity at an edge, using the geometric properties of the three aberration convolutions, the rotation and translation (transform) required to align the frame of the ramp edge model to the image patch can be estimated; *i.e.* representing a correction vector from the centre of the unit circle to perpendicular with the underlying ramp edge feature; see example illustration in Fig. 24. With reference to [24], the adapted equations of interest were Eq. (56), Eq. (60), Eq. (66), and Eq. (70).

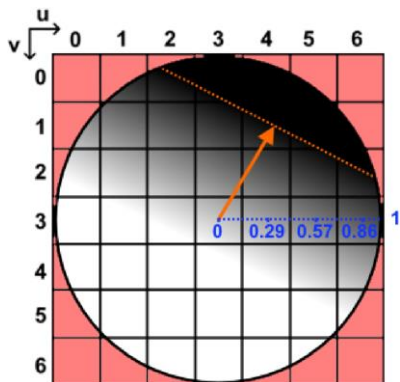


Fig. 24 Illustration of unit circle correction vector to edge perpendicular

Transforming and re-scaling the identified correction vector back to the pixel coordinate frame as a (u, v) sub-pixel adjustment, this was then applied to the pixel-level edge candidate to localise the coordinate to the underlying edge shape. This sub-pixel coordinate adjustment was repeated for each edge candidate in the contour.

2.2.2.5 Conic Fitting

To centralise the origin of the pixel frame to the sensor's optical axis for conic fitting, the inverse transforms detailed in 1.3.5 were applied to map the sub-pixel adjusted contour from pixel coordinates to the object space world frame; during testing, the image depth was set to scale the frame by a factor of 10.

In order to identify the conic shape from the coordinates of the contour, the least squares method was applied using Singular Value Decomposition (SVD). This method fits a model of the conic quadratic equation, Eq. (9), to a set of coordinate points by minimising the sum of the squared distance between each sample point and the function of a conic curve; *i.e.* minimising the squared residual sum.

To improve the robustness of this approach, the least squares fitting method was applied using an implementation of Random Sample Consensus (RANSAC) [38]. This method iteratively generates candidate models by re-running the least squares fitting method with a random subset of the points that make up the identified edge contour. The accuracy of each candidate was assessed by running the model across all points in the contour, and summing the number of inliers that fall within a given tolerance of the expected result; *i.e.* from Eq. (9) the conic quadratic equation should be equal to 0 for all points on a well fit conic.

The best conic equation model identified by the RANSAC method is the one with the greatest number of edge point inliers. Based on the results of initial testing, the parameters that were used for conic fitting are:

- a) For each edge contour, RANSAC was used to test 100 candidate conic models;
- b) Each model was fit with a minimum of 6 random sample points, or 20% of the total points in the contour, whichever is larger;
- c) The conic is of a type expected from the simulated orbit altitude and FOV, *i.e.* a conic eccentricity > 1 ;
- d) The tolerance to classify a point as an inlier to the candidate model was a conic quadratic equation result of 0 ± 0.1 ;

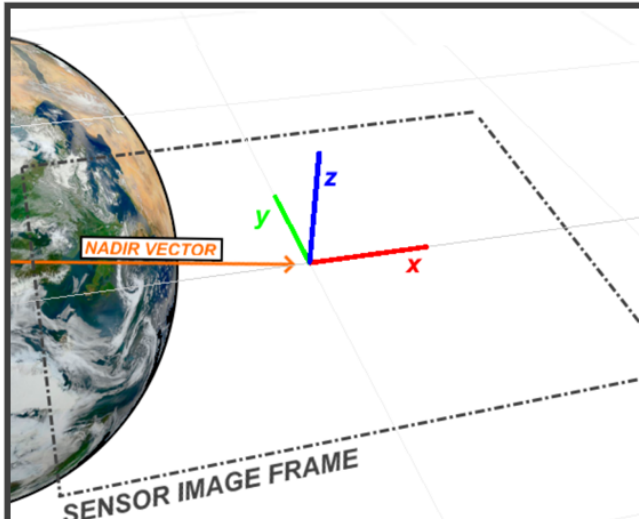
- e) The candidate model must represent a non-degenerate conic; *i.e.* referring to Eq. (10), the determinant of the 3x3 matrix form of the conic quadratic equation is not equal to 0 [29].

2.2.2.6 Attitude Estimation

Using the approach described in 1.3.6, the coefficients of the conic that was fit to the horizon edge contour were used to estimate:

- a) The rotation about the bore of the detector [$R(z)$] to align the sensor frames y-axis to a plane with the nadir vector, relates to Eq. (14); and
- b) The angle between the sensors optical bore and the planets nadir vector [$R(x')$], relating to Eq. (12) and Eq. (13).

To better visualise the calculated Euler zx' frame rotation transforms, an illustration is provided in Fig. 25 and Fig. 26.



**SENSOR FRAME AT SOME ORIENTATION
RELATIVE TO NADIR VECTOR**

Fig. 25 Example illustration of the prototypes image frame at some arbitrary orientation relative to the planet

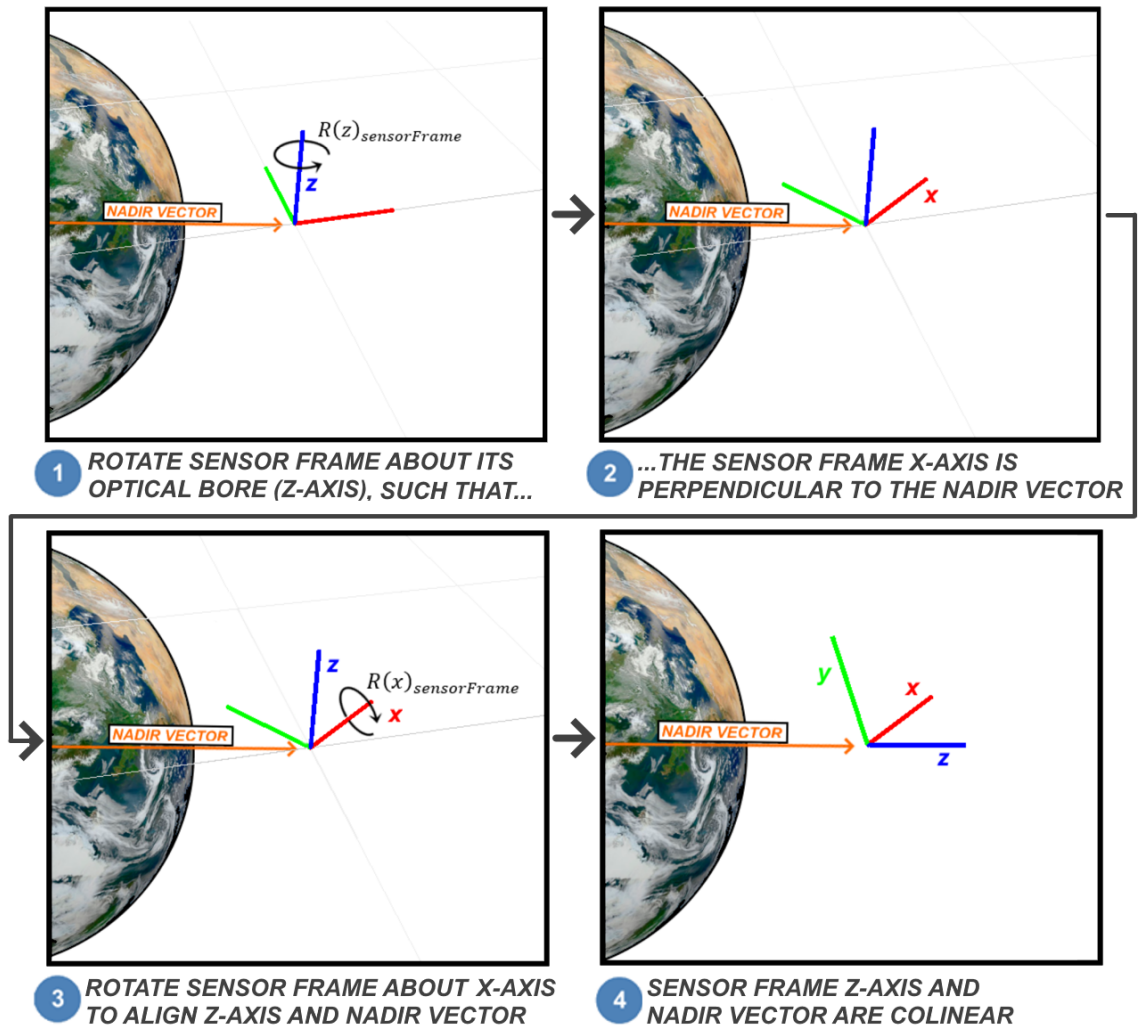


Fig. 26 Illustration of a Euler $R(z)R(x')$ attitude determination of nadir vector relative to horizon sensor bore

2.2.3 Host Device Viewing Software

To receive data from the prototype horizon sensor, it must interface with a host device externally via a serial communication protocol. For ease of connecting to a standard computer COM port, the prototype's link was configured as a serial UART interface. Using this method, a COM port connected Python script on the host computer was used to monitor and de-serialise the data sent by the microcontroller.

To interpret and visualise the prototype horizon sensors thermal image and edge coordinate data on the host machine, a communication formatting convention was established which the Python script scans for.

Each of these transmissions was encapsulated by a special start and end tag, along with an accompanying header containing metadata about the matrix being sent. The convention uses delimiter-separated formatting to send the image and coordinate data as a table matrix to the host machine; see example illustration of convention Fig. 27, with metadata depicted in blue, and matrix data in red.

```

~txBEG~

{ID:matrixUniqueReference,X:matrixColumns,Y:matrixRows,dt:matrixDataType}
    matrixData(0,0), matrixData(0,1), matrixData(0,2), ... ;
    matrixData(1,0), matrixData(1,1), matrixData(1,2), ... ;
    ...
~txEND~

```

Fig. 27 Illustration depicting the serialised communication convention used by the prototype to send image and coordinate data to external host

When the host Python script interprets a transmission using the convention, the data is de-serialised to be rendered as either an OpenCV image, or a Matplotlib graph.

The ID in the header is a unique reference to the dataset on the microcontroller, and was used to determine which window the data should be rendered to; *i.e.* each unique ID received is rendered to a new window, if the same ID is seen again the existing window is updated instead. Using this approach, each stage of the images processing was able to be rendered to a separate window, without the microcontroller requiring any additional copies in memory.

All other messages from the prototype that did not match the convention were passed by the Python script directly to the hosts terminal, *e.g.* calculated outputs, program states, debugging, *etc.*

In cases when the host machine did not have capabilities to run the Python viewing software, the prototypes messages were able to be monitored through a console terminal directly linked to the port the device was connected to. Additional functionality was added to allow the prototype to generate rudimentary images within the terminal using ASCII gradients. As the ASCII images were generated, an aspect ratio compensation was applied by the prototype to account for the size of the ASCII

characters, intended to generate a pseudo accurate representation of the images length-to-width ratio when printed to the hosts text-based terminal.

Examples illustrating the two image rendering approaches are shown in Fig. 28.

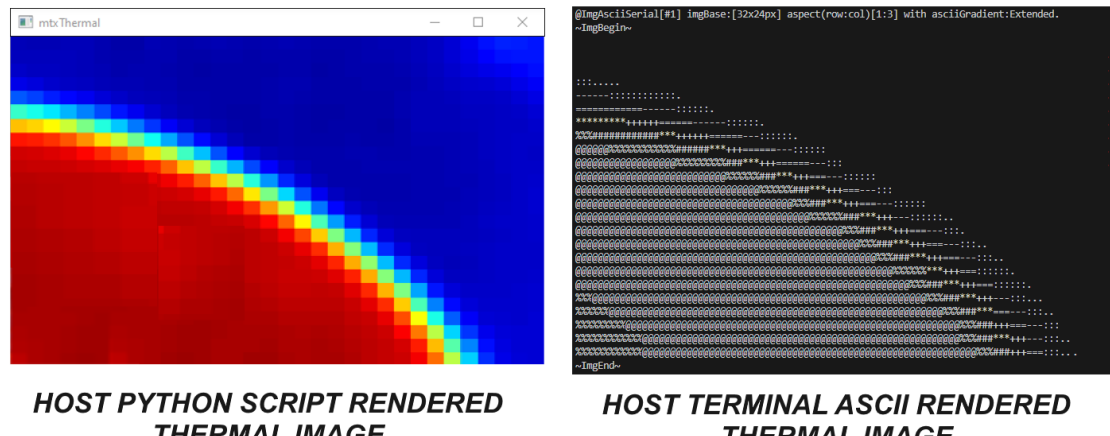


Fig. 28 Host software image rendering options as OpenCV backend vs terminal ASCII gradient image

2.3 Orbital View Test Stand

To assess the utility of the prototype infrared horizon sensor, a simulated infrared view of Earth's orbital horizon was designed, with the following configuration:

- a) LEO orbital altitude of 600-800km;
- b) $55^\circ \times 35^\circ$ sensor FOV;
- c) Viewed from the nominal orientation (refer Fig. 15).

The prototype was mounted to a controllable pitch and roll gimbal while viewing the proxy orbital view, at a distance of 25cm from its thermal face. By adjusting the sensors roll and pitch by known quantities, the horizon sensors attitude estimation relative to the nadir vector of the simulated view can be evaluated.

The final test stand is comprised of two key components, the proxy infrared orbital view that the prototype will perceive, and the controllable pitch-roll gimbal that the prototype is mounted within; the design considerations of both are detailed in the following sub-sections.

2.3.1 Proxy Infrared Orbital Scene

To create the simulated orbital view in the infrared range, two metal plates of differing temperatures were placed in view of the sensor. The front plate is heated representing the warm Earth silhouette, and was cut to the shape of the expected horizon edge conic section, while the rear plate was cooled to sub-zero temperatures to simulate the background of space; the design is illustrated in Fig. 29 and Fig. 30.

The overall scale of the test stands simulated orbital view was based primarily around the plate sizes available during design, with the scene scale based on the FOV in view of the sensor relative to the overall front face plate dimension of 380x300mm.

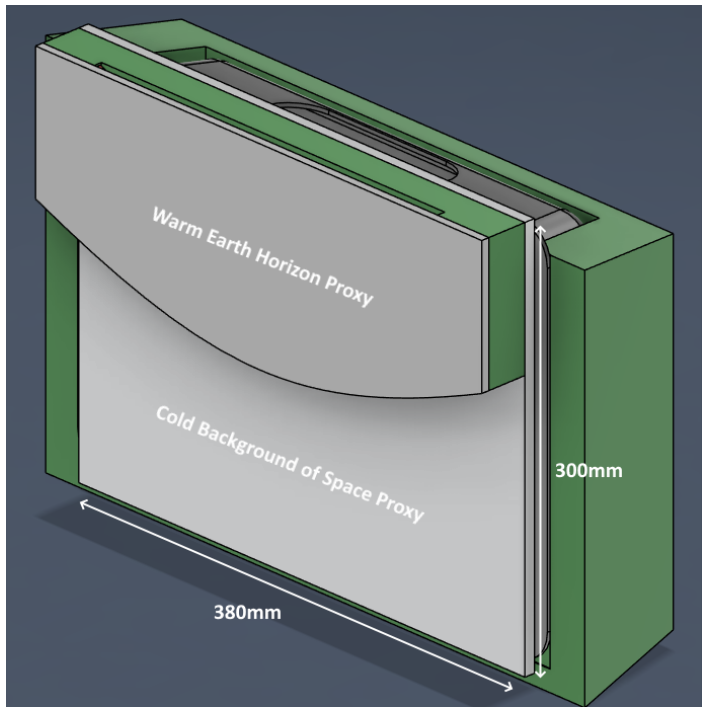


Fig. 29 Simulated infrared orbital view test stand design model

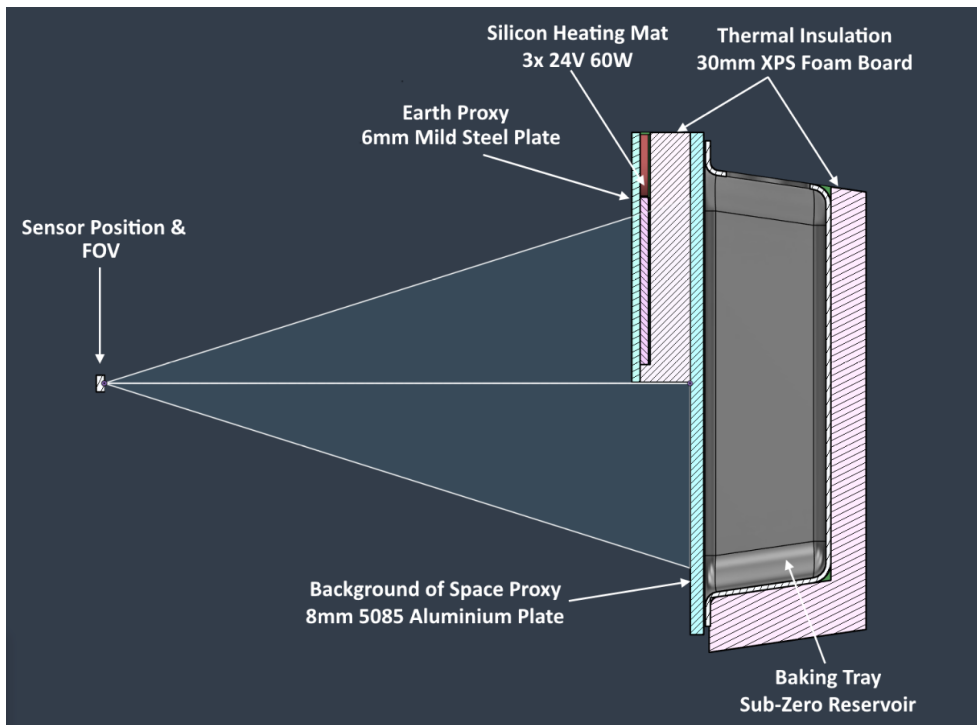


Fig. 30 Side section of simulated infrared orbital horizon view test stand

To quantify the conic shape to be cut into the front plate, a scaled model of the crafts $55^\circ \times 35^\circ$ FOV view from orbit, while in the nominal orientation, was designed in CAD. The model uses a spherical Earth approximation, with a representative radius of 6,378km [5]. The conic projection of the circular visible horizon onto the object space

world image plane, as viewed from the crafts sensor, was then extracted; see example illustration Fig. 31.

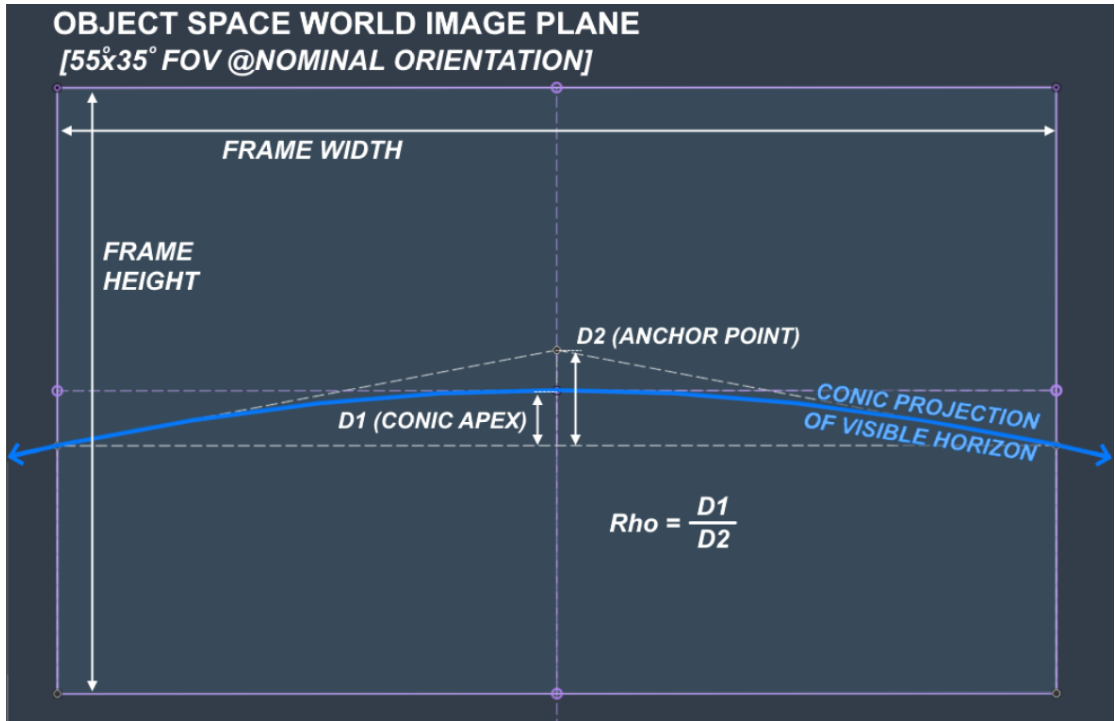


Fig. 31 Parametric model of visible horizon projection to world image plane, from $55^\circ \times 35^\circ$ FOV sensor, while in nominal orientation; ρ selected to match projected horizon conic shape bound to image frame

As only a portion of the conic is in view of the crafts sensor (based on the sensors FOV), the accurate replication of the shape of this bound section on the test stands front plate was the main objective.

To achieve this, the conic projective discriminant [ρ], relative to the image plane, that matched the bound shape of the projected horizon edge at 600km, 700km, and 800km altitude was identified; see Table 2 below. This 200km range was chosen to provide some tolerance in the front plates manufacturing.

Using this approach, the portion of the conic within the image frame was replicated to the front plate of the test stand, using scaled measurements relative to the overall visible FOV size of the test stands front face; the conic projective discriminant is defined in Eq. (17), with the scaling ratio used in Eq. (18).

$$\rho = \frac{D1 \text{ (Conic Apex)}}{D2 \text{ (Anchor Point)}} \quad (17)$$

$$anchorScalingRatio = \frac{D2 \text{ (Anchor Point)}}{x_{frame}} \quad (18)$$

TABLE 2 Identified conic projective discriminant relative to image frame for 55°x35° FOV sensor while in nominal orientation

Orbit	Distance to Plane	Frame Width	Frame Height	Conic Apex	Anchor Point	Conic Projective Discriminant [ρ]
Altitude [h]	[L_{sight}]	[x_{frame}]	[y_{frame}]	[D1]	[D2]	
600km	2,831km	2,947km	1,785km	162km	299km	~0.54
700km	3,069km	3,195km	1,935km	191km	359km	~0.53
800km	3,293km	3,429km	2,077km	220km	423km	~0.52

TABLE 3 Scaled conic discriminant values relative to test stands 380x300mm face

Simulated Altitude	Conic Apex [D1]	Anchor Point [D2]
600km	~21mm	~39mm
700km	~23mm	~43mm
800km	~24mm	~47mm

Referring to Table 3, the conic projective discriminant used to define the front plate shape was 0.53 ± 0.01 , this equates to a conic apex distance of 21-24mm (with the conic apex anchored to the centre of the test stand), and an anchor point of 39-47mm; representing an orbit altitude between 600km and 800km, for a 55°x35° sensor FOV, at nominal orientation.

The rear plate that simulates the $\sim -270^\circ\text{C}$ [5][39] cold background of space was cooled via an insulated reservoir attached to its back. As achieving this low of a temperature was not practical without specialised equipment, the reservoir was instead filled with liquid nitrogen (LN_2) at approximately $\sim -196^\circ\text{C}$ at 1-atmosphere [40]. The reservoir was mounted via bolts that thread into the back plate over a silicon gasket, the top

section of the reservoir was also left unsealed, to allow safe venting of any pressure generated from the liquid nitrogen as it evaporates.

Although Earth's recent average global temperature was approximately $\sim 15^{\circ}\text{C}$ [8], a higher target front plate temperature of $\sim 35\text{--}45^{\circ}\text{C}$ was selected to improve the thermal differential against the practically achievable temperature of the cold back plate; and was intended to more accurately portray the difference in temperature that would be seen from orbit.

The front plate was heated with three thermistor-controlled silicon 3D printer bed heating mats. To improve heat soak, and reduce the potential for visible hot spots mentioned as problematic for infrared imaging by [19], the mats were undervolted to 12V and run in parallel, providing $\sim 45\text{W}$ of total heating power to the 2.4kg front plate; approximately $+2.5^{\circ}\text{C}/\text{min}$ for the plates final size.



Fig. 32 Silicon heating mats attached to rear of horizon front plate

To achieve a distinct thermal edge for the horizon sensor to detect, the heated Earth plate was positioned at the top of the test stand, this positioning was intended to reduce the amount of heat rising in front of the cold plate via convection; a common cause of error identified in similar efforts by [18] and [19].

Both plates were thermally insulated from each other with closed cell foam board, which was affixed using silicon to allow flexibility as the plates thermally expand and contract. Because the top positioning of the front plate creates a cantilever, two structural timber dowls have been added to tie the two plates together. This was intended to give structural support to the cantilevered front plate, without providing a thermally conductive path between them; one of the front-plate connected structural dowels is seen through its mounted hole on the cold plate top left of Fig. 33.



Fig. 33 Proxy infrared horizon view test stand rear

Ideally, the front surfaces of both plates facing the thermal camera should have a high emissivity / low reflectivity [18] to improve their ability to emit thermal radiation that is detectable by the infrared camera. The front of both plates on the test stand have therefore been coated with a thin matte black enamel automotive paint, which was lightly sanded to increase the surface area available to emit radiation.

To hold the finished test stand in its intended vertical position, two mounting support structures were designed. The mounting supports interface with either side of the 8mm thick aluminium cold plate, which the remaining components of the test stand are securely attached to. To minimise the risk of the test stand toppling and causing a

hazardous LN_2 spill while in use, the mounting supports were designed with additional structures to allow the entire assembly to be clamped to the work surface; the mounting supports are shown in Fig. 34.



Fig. 34 Rear top-angled view of test stand showing mounting support structures

2.3.2 Controlled Pitch-Roll Axis Gimbal

Due to the miniaturised scale of the simulated view vs what would be seen from orbit, the accurate positioning of the horizon sensors detector at the intersect of the pitch and roll axes was a key consideration of the gimbals design. Ideally, the converging point of the pinhole camera should be positioned at this intersection, such that changes to pitch and roll are interdependent. To aid this point, the pitch-roll gimbal was designed with scribed markings indicating the models coordinate frame, as well as an allowance for adjustability of the sensors mounting position in the x, y, and z translational axis to precisely align the sensors detector; the initial model is shown in Fig. 35.

The horizon sensor PCB mounts to the roll structure via four securely mounted M2 threaded rods, two nuts on each rod are used to correctly position the detector of the PCB along the z-translational axis, and lock it into position.

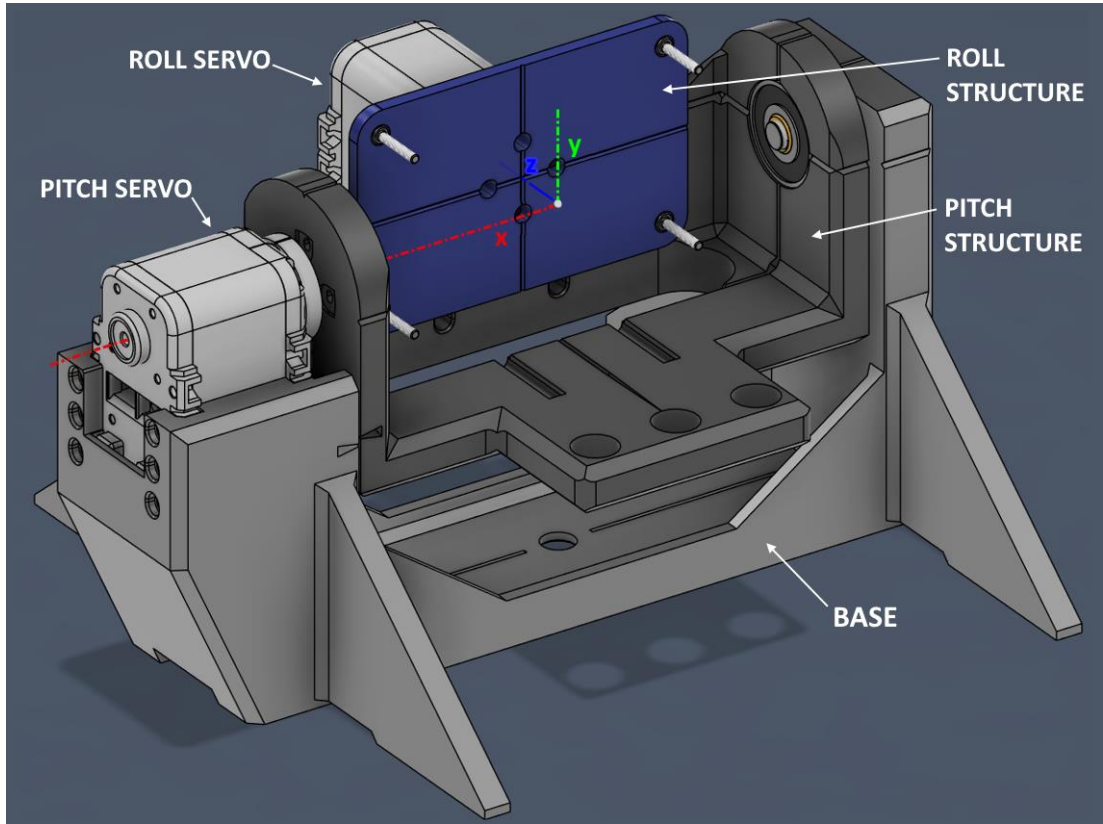


Fig. 35 Pitch-roll gimbal model components, associated coordinate frame and scribed indication markings

To target the design requirement of $<0.5^\circ$ positional accuracy, two Dynamixel AX-12A [41] robotics servos were selected to drive the pitch and roll axis structures. To reduce the effects of backlash, the geared servos are directly mounted to their respective pitch and roll structures with no additional gear reductions.

The un-driven side of the pitch structure is supported by a skateboard bearing mounted via a threaded bushing bolted to the structural base. An allowance was also given for counterweight bolts to be installed at the front of the pitch structure, to balance the weight of the cantilevered roll servo, as required.

Additionally, the design of the base structure allows the pitch-roll gimbal to be used either directly on a flat surface, or mounted to a tripod using a common 3/8" UNC threaded camera mount insert. The tripod insert was permanently pressed into a section of aluminium flat bar that runs the length of the base; helping to distribute forces and also providing additional rigidity to the structure, depicted in Fig. 36. This was done to allow flexibility positioning the prototype relative to the test stands simulated view.

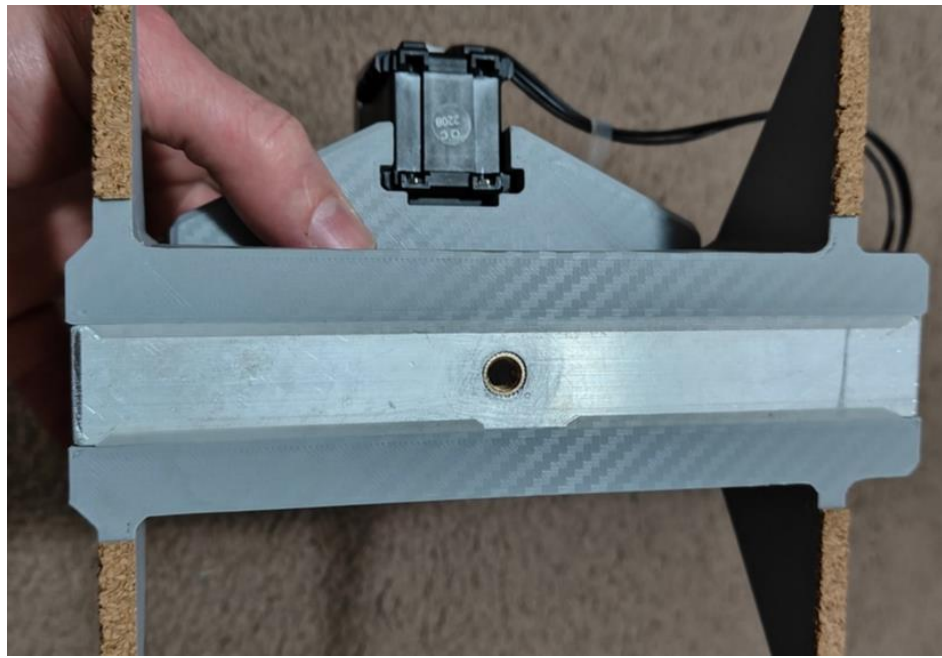


Fig. 36 Base structure tripod mount and aluminium flat bar reinforcement

The model parts were printed in PLA, see Fig. 37; and sliced with extra wall thickness and additional internal structure in key locations, intended to increase the model's physical rigidity, and therefore positional tolerance.

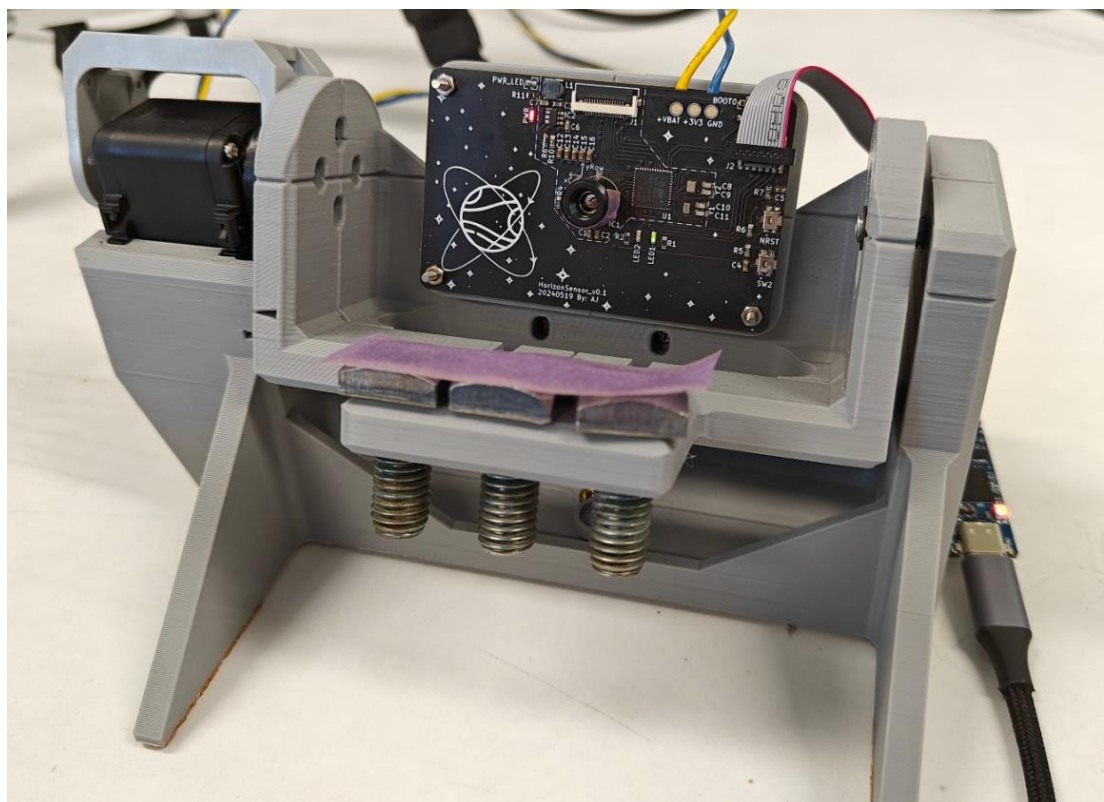


Fig. 37 Assembled pitch-roll gimbal

3. Results & Discussion

The following section presents the projects outcomes in the context of the Requirements Verification Matrix in section 2.1, the result of each success criteria is provided, along with general discussion points regarding the results.

3.1 Horizon Sensor Prototype Verification

The results and discussion of each project requirement relating to the prototype infrared horizon sensor have been grouped into the following sub-sections; a summary of the outcomes is provided in Table 4.

TABLE 4 Horizon Sensor Prototype Requirement Verification Results

Req. No.	Name	Result	On	By
[P-1]	Infrared Sensitivity	Success criteria met contingent assumption on wavelength of FIR subdivision scheme.	9-Oct-2024	A.Janssen
[P-2]	Thermal Sensor Image	All success criteria met.	9-Oct-2024	A.Janssen
[P-3]	Coarse Edge Detection	All success criteria met.	9-Oct-2024	A.Janssen
[P-4]	Sub-Pixel Edge Correction	All success criteria met.	9-Oct-2024	A.Janssen
[P-5]	Conic Fitting	All success criteria met.	9-Oct-2024	A.Janssen
[P-6]	Attitude Estimation	All success criteria met for overall outputs at each roll angle. 7 of the 45 results contain minor outliers related to the conic rotation within the image frame.	9-Oct-2024	A.Janssen
[P-7]	Power Source	All success criteria met.	9-Oct-2024	A.Janssen
[P-8]	External Interface	All success criteria met.	9-Oct-2024	A.Janssen

3.1.1 [P-1] Infrared Sensitivity

Statement: The infrared sensor shall have sensitivity within the preferred 14 to 16 μm infrared radiation band detectable from orbit.

Success Criteria:

- ✓ *[By Inspection]:* The spectral sensitivity of the sensor is within the stated infrared band, confirmed via manufacturer datasheet.

Although the Melexis MLX90640 datasheet [30] states that the detector is sensitive to the Far Infrared (FIR) range of the thermal spectrum, it does not specifically state a spectral wavelength range, or the standard subdivision scheme this FIR classification belongs to. However, a reasonable assumption based on a typical FIR sensitivity is in the range 15 μm to 1,000 μm [42], [43].

Although this does not specifically meet the ‘reference to datasheet’ component of the success criteria, the FIR estimation is deemed a suitable stand-in to satisfy this requirement and continue testing the remaining functionality of the prototype horizon sensor.

Despite the datasheets mentioned FIR sensitivity, terrestrially the 8-15 μm range just below FIR is commonly targeted in these types of thermal sensors, to avoid the atmospheric water vapour and CO_2 absorption bands [42]; *i.e.* the range has improved transparency to infrared radiation while inside the atmosphere. As discussed in 1.3.1, the preferred sensitivity for infrared horizon detection from orbit is 14 to 16 μm [5], where these absorption and emission bands aid in providing the planet’s atmosphere an opaque and uniform appearance [7].

Although the sensor’s estimated FIR sensitivity does have some crossover with this preferred 14 to 16 μm range, a sensor with a closer stated specification would have been favourable. Alternatively, the application of a ~14 - 16 μm infrared filtering film over a detector with sensitivity encompassing this range, may also be an option worth investigating in future.

3.1.2 [P-2] Thermal Sensor Image

Statement: The prototype shall incorporate a matrix of thermal detector type infrared sensors to construct a thermal image of the given scene.

Success Criteria:

- ✓ *[By Inspection]:* The infrared imaging sensor is a matrix of thermal detector type sensors (*e.g.* a thermopile matrix), confirmed via manufacturer datasheet.
- ✓ *[By Inspection]:* The prototype transfers the captured thermal image of a known scene of infrared emitting objects to host machine for inspection.
- ✓ *[By Inspection]:* Taking an image from the same location using a calibrated thermal camera; by visual inspection, the pose of features in both images are correlated and represent the scene of infrared emitting objects.

The MLX90640 infrared sensor is made up of a 32x24px matrix of thermopiles [30], and therefore satisfies the criteria for a thermal detector class of sensor.

The infrared scene reference contains a curved plate which is heated to ~40°C, and a background plate at room temperature. From a static location in front of the scene, an image is taken with a calibrated 160x120px FLIR One Pro thermal camera, followed by the MLX90640 infrared sensor from the same location.

The MLX90640 image pixel intensities are transferred via serial UART to the COM port of a host machine as a float matrix, which is then interpreted and rendered using the OpenCV library.

As shown in Fig. 38, the thermal image generated by the MLX90640 aligns with the features of the scene reference, and despite the lower resolution, the generated shape is highly correlated to the calibrated thermal camera.

This provides confidence that the infrared sensor is operational, and that the firmware written for the prototype is correctly interpreting the thermal image.

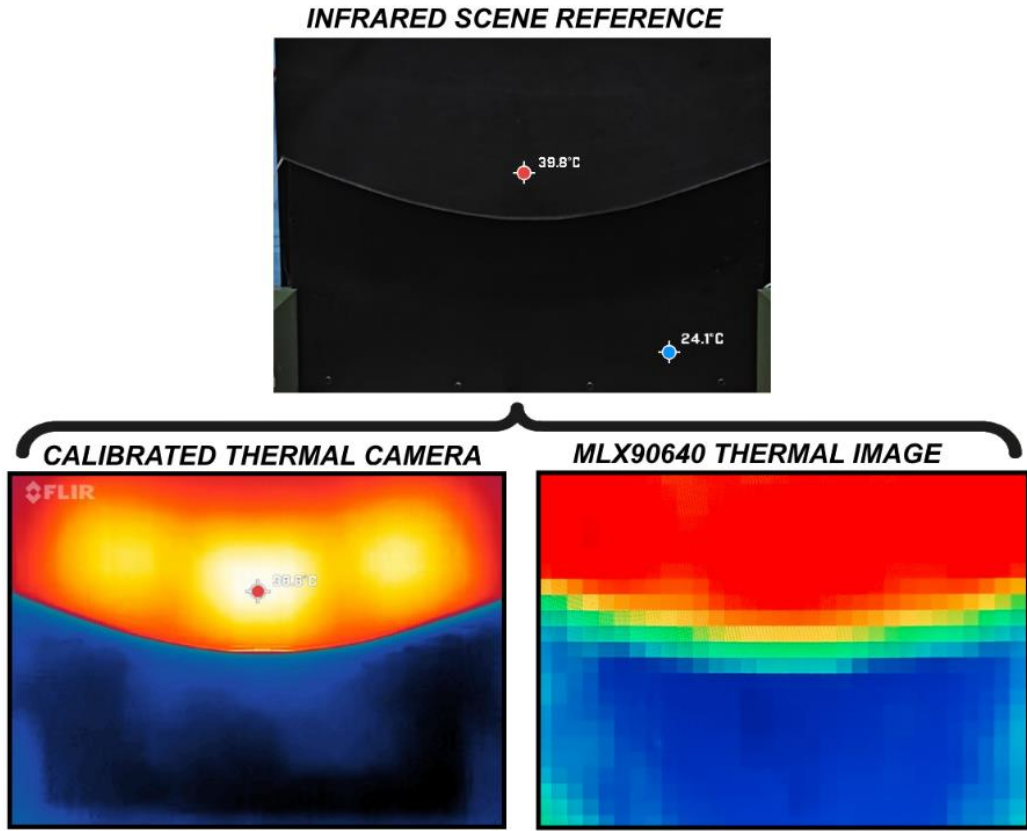


Fig. 38 MLX90640 image feature validation against calibrated FLIR One Pro thermal camera

As briefly mentioned in 2.2.2.1, the MLX90640 transfers the thermal image to the microcontroller in two distinct subframes, illustrated in Fig. 39. The time to receive each subframe is based on the sensors refresh rate, assuming the fastest 64Hz communication rate of the sensor, the generated thermal image is made from both subframes read over a period of ~31 millisecond; illustrated in Table 5.

Figure 8 TV mode reading pattern (only highlighted cells are updated)

Fig. 39 MLX90640 separate subframe transmissions required to construct each thermal image [30]

It was noted there is the potential for temporal artifacts in the generated image based on the selected refresh rate, *i.e.* banding due the combination of subframes taken from slightly different views of the scene. Considering the image is generated from two subframes taken at slightly different times, this could cause inaccuracies in the detected horizon edge when the craft is experiencing high rates of rotation.

TABLE 5 MLX90640 subframe refresh rate effects on image generation period

MLX90640 Refresh Rate [30]	New Subframe	Image Generation Period
8Hz	~125ms	~250ms
16Hz	~62ms	~125ms
32Hz	~31ms	~62ms
64Hz	~16ms	~31ms

3.1.3 [P-3] Coarse Edge Detection

Statement: The prototype shall internally process images captured from the thermal camera and perform coarse edge detection to identify candidate edge sequences within the image.

Success Criteria:

- ✓ *[By Inspection]:* The prototype transfers the thermal image and identified edge coordinates to host machine for inspection.
- ✓ *[By Inspection]:* The identified edge sequences visually correlate to intensity transitions in the underlying thermal image.

The prototype processes the captured test image as described in 2.2.2.2 and 2.2.2.3. The initial image, its pre-processed state, the edge candidate mask, and the identified pixel-level edge sequence are all transferred from the prototype to the host device to be rendered using OpenCV.

Referring to Fig. 40, the prototypes initial test image is shown in (1), followed by the resulting image after pre-processing with an applied Gaussian blur in (2). The intensity gradient of the pre-processed image is then used to generate the prominent edge

candidate mask using non-maximal gradient suppression; shown in (3) with strong edge candidates depicted in white, and weak edge candidates in grey.

Lastly, while referencing the pre-processed image, edge tracking via hysteresis is applied to the edge candidate mask to identify the prominent pixel-level edge sequence in the image (4); the rendered colour gradient of the edge sequence simply indicates the start and end of the BFS algorithms traversal.

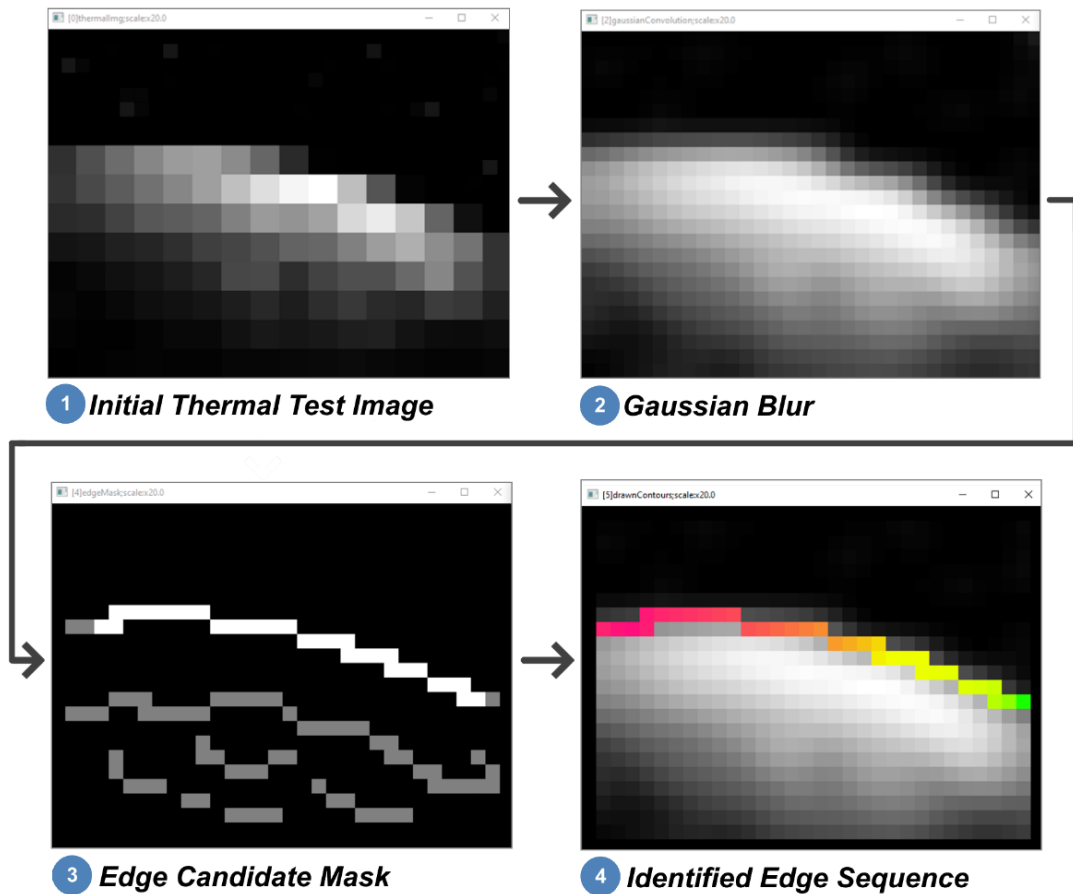


Fig. 40 Prototype image pre-processing and coarse edge sequence detection, rendered from host device in greyscale using OpenCV

The prototype's coarse edge detection algorithm was able to correctly identify the prominent edge in the thermal test image. The edge sequence is also well correlated to the area of high intensity change in the underlying image, and therefore satisfies this requirement.

It was found during testing that the sequence length constraint worked well to ensure the identified sequence was the prominent edge in the image. Given the sensors low-resolution representation of the scene, a constraint similar to this may be useful to

reject false edge positives from other bodies in the background of the image frame, *e.g.* with additional edge shape constraints, rejection of the Sun and Moon.

The function parameters used to process the image and identify its prominent connected edge sequences appear to perform well for the given task. However, it should be noted that the image was taken while the sensor was statically positioned relative to the test view, giving the thermopile pixel sensors time to settle to an output representative of the thermal energy being emitted.

Unlike photonic detectors, an inherent characteristic of thermal detector type sensors is a slightly delayed response to changes in radiation. This is due to the detector requiring time to adjust to the new infrared radiation level being absorbed, before its output signal settles to represent the updated view. When the sensors position is rapidly changed between snapshots of the scene, this characteristic appears as ‘ghosting’ in the image; see example in Fig. 41.

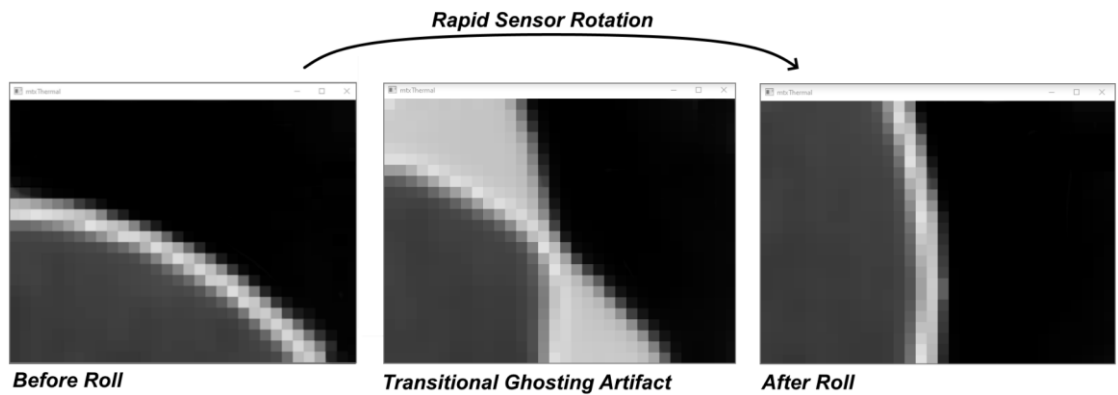


Fig. 41 Transitional ghosting artifact during rapid movement due to response rate of thermal detector

Although the sensor settles relatively quickly, estimated $< 1\text{ second}$ (ΔC dependant), the transitional artifact may be erroneously detected as a valid edge. It was noted that this phenomenon, in addition to the refresh rate banding mentioned in 3.1.2, has the potential to cause inaccuracies in the detected horizon edge, particularly when the craft is experiencing high roll rates (*e.g.* during tumble recovery *etc.*).

Given the MLX90640 sensor is on the cheaper end of what is available on the market, higher quality thermal detector type sensors may exhibit improved response characteristics.

3.1.4 [P-4] Sub-Pixel Edge Correction

Statement: The prototype shall apply a sub-pixel edge correction method to refine the accuracy of the identified pixel-level edge sequence.

Success Criteria:

- ✓ *[By Inspection]:* The prototype transfers the captured thermal image, original edge coordinates, and sub-pixel adjusted coordinates to host machine for inspection.
- ✓ *[By Inspection]:* By visual inspection, the sub-pixel edge correction is more closely aligned to the true shape of the imaged feature, vs the original pixel-level edge.

The prototype views the simulated orbital horizon test stand, and is positioned to capture a range of detected horizon edge directions. The captured thermal image, identified pixel-level edge contour, and the sub-pixel adjusted contour are transferred to the host device.

The results received from the prototype are presented in Fig. 42, Fig. 43, Fig. 44, Fig. 45, and Fig. 46 below.

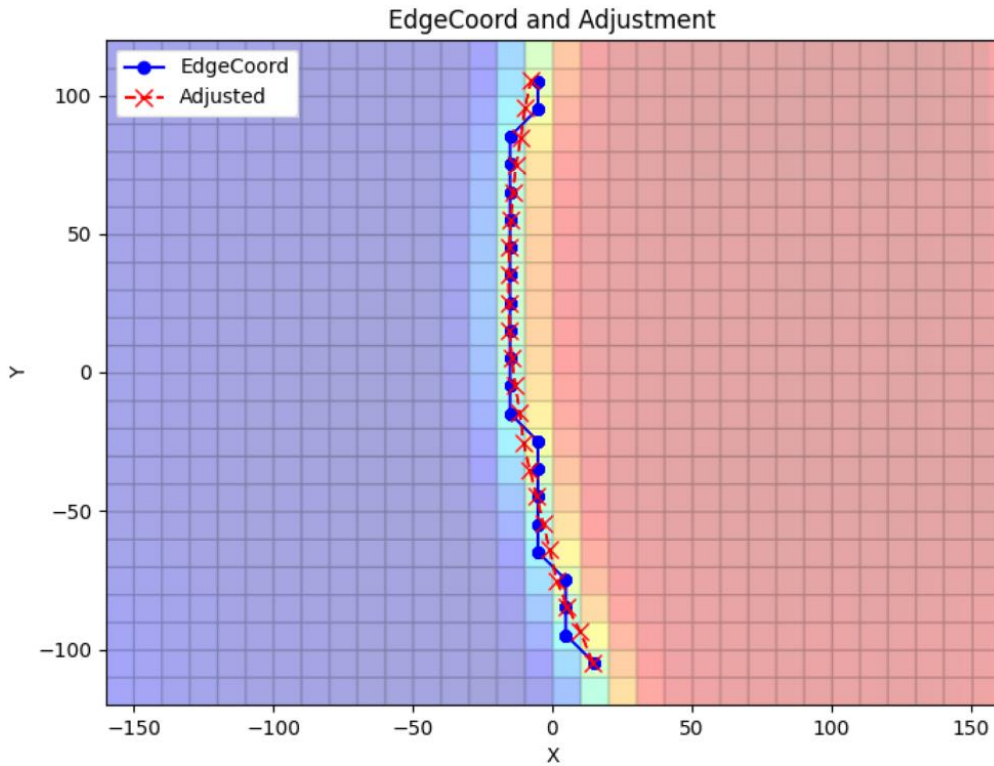


Fig. 42 Right positioned orbital horizon thermal image, identified edge contour and correction received from prototype; pixel-level guess in blue, sub-pixel edge correction shown in red

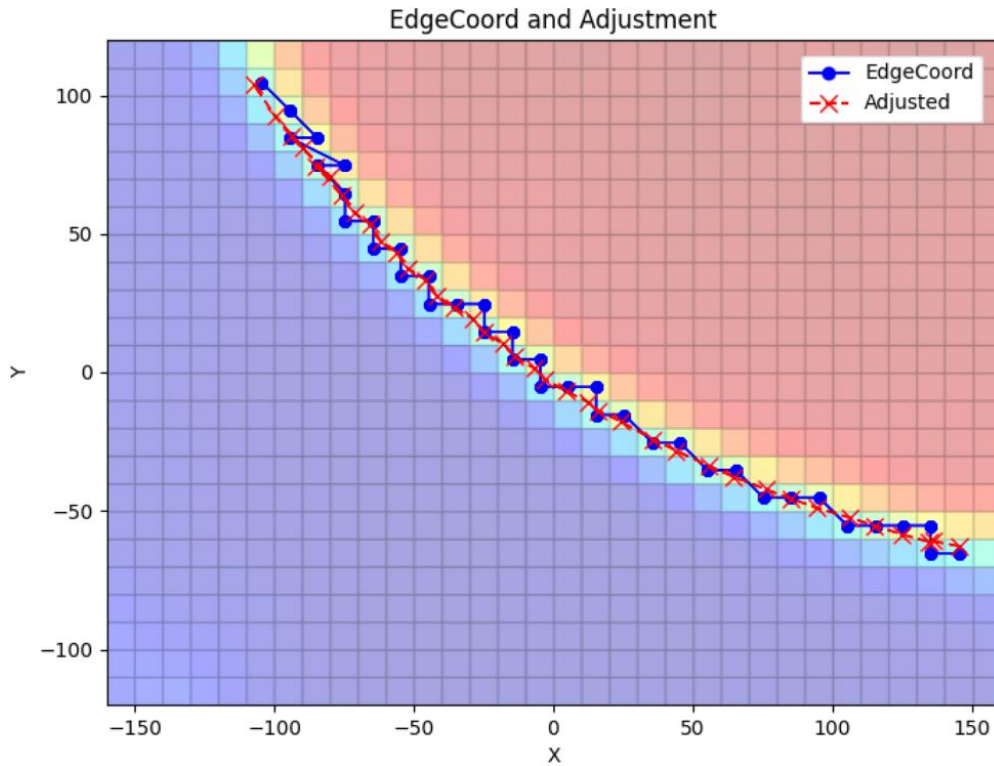


Fig. 43 Top-right positioned orbital horizon thermal image, identified edge contour and correction received from prototype; pixel-level guess in blue, sub-pixel edge correction shown in red

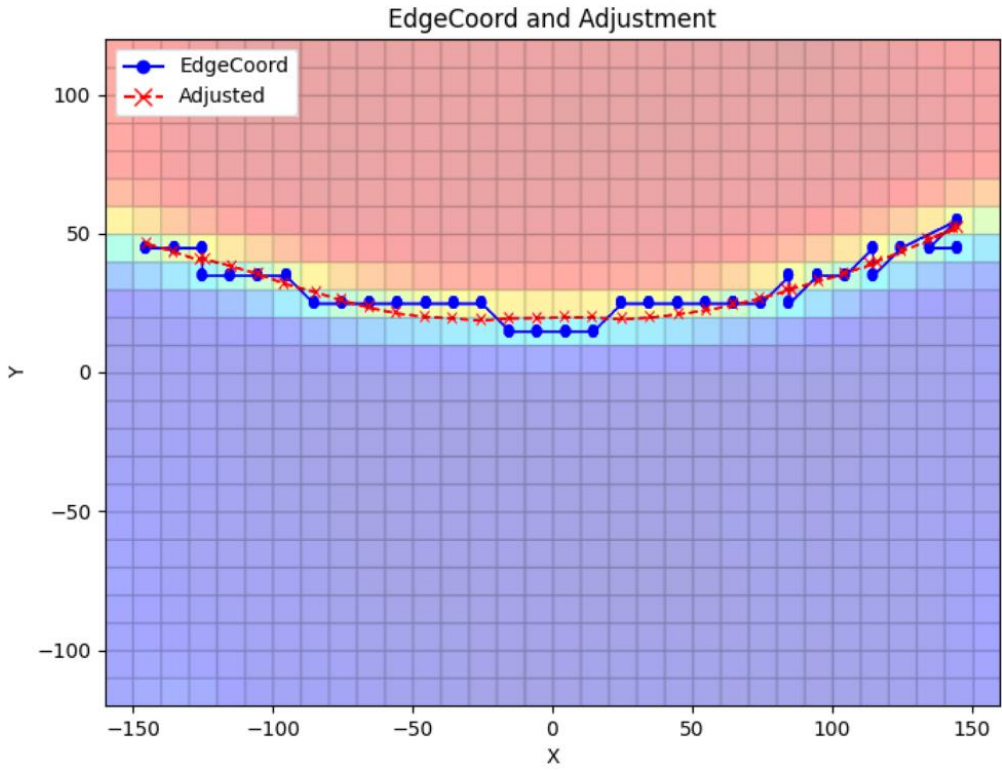


Fig. 44 Top positioned orbital horizon thermal image, identified edge contour and correction received from prototype; pixel-level guess in blue, sub-pixel edge correction shown in red

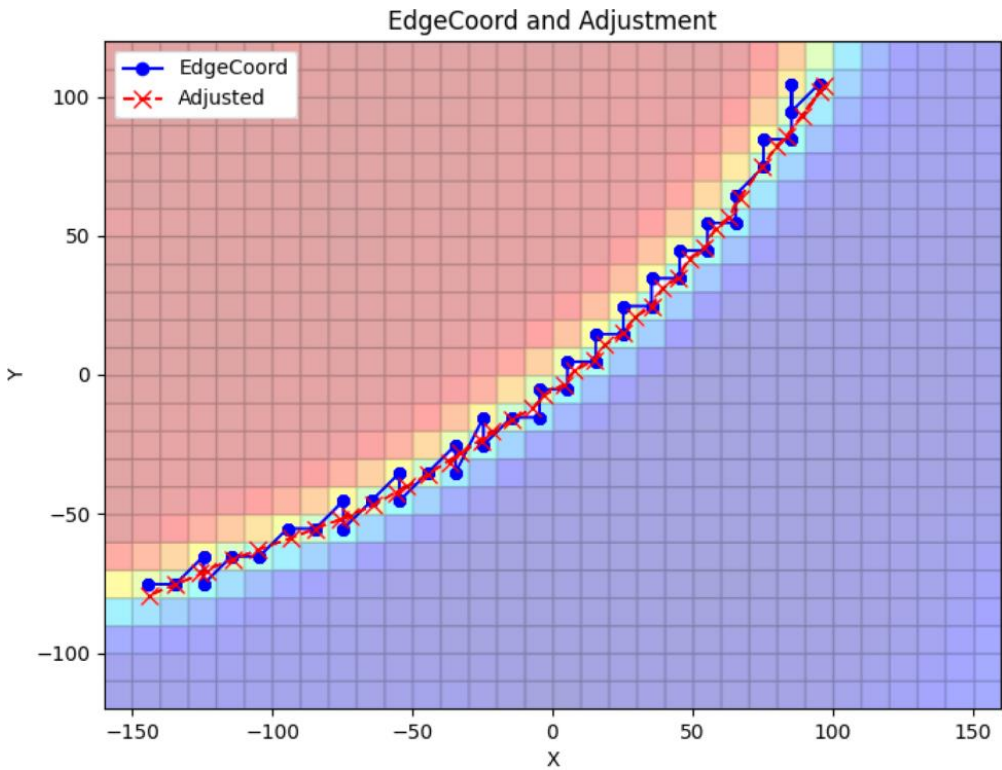


Fig. 45 Top-left positioned orbital horizon thermal image, identified edge contour and correction received from prototype; pixel-level guess in blue, sub-pixel edge correction shown in red

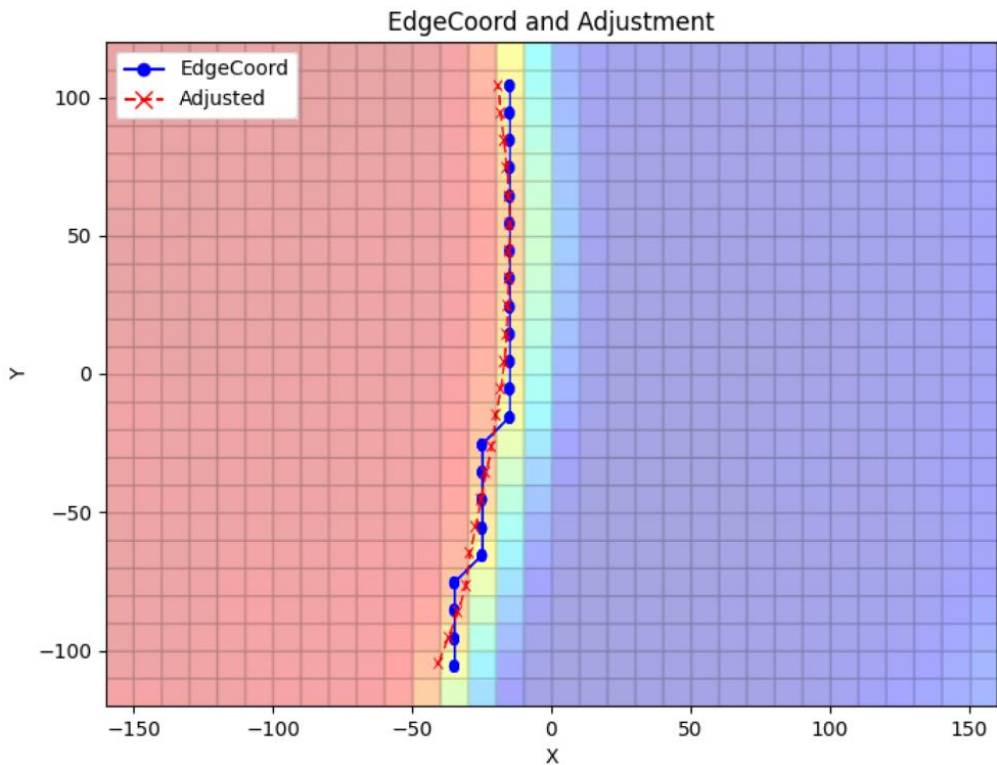


Fig. 46 Left positioned orbital horizon thermal image, identified edge contour and correction received from prototype; pixel-level guess in blue, sub-pixel edge correction shown in red

Referring to the figures above, it is evident that the sub-pixel edge corrections have greatly improved the accuracy of the identified horizon edge arc. In each image, the adjusted edge contour is a much closer representation of the underlying conic shape than the initial pixel-level edge guess, and therefore satisfies the success criteria for this requirement.

The implemented sub-pixel edge correction was able to enhance the prominent edge detection performance of the 32x24px thermal sensor, allowing it to determine the coordinates of large edge features in the image to a precision that would typically require a higher resolution thermal camera to resolve. This is an exciting prospect for improving the general edge detection utility of these low-resolution sensors, particularly in the context of orbital horizon detection for small satellites.

3.1.5 [P-5] Conic Fitting

Statement: The prototype shall attempt to fit a conic section to the identified edge sequence and estimate the coefficients of its general quadratic equation.

Success Criteria:

- ✓ *[Test]:* The prototype captures an image of the test stand and transfers the edge coordinates and conic quadratic coefficients that were identified to host machine for inspection.
- ✓ *[Test]:* The identified conic represents the configuration of the test stand, and is a hyperbola with eccentricity between 1.94 and 2.25 (800-600km altitude).
Configuration of test stand: LEO altitude of 600-800km from a 55°x35° FOV sensor at nominal orientation (refer Fig. 15).

While viewing the simulated orbital horizon scene, the prototype identifies the sub-pixel coordinates of the horizon edge in the captured thermal image, and applies the conic fitting method discussed in 2.2.2.5. Rotating the sensor to various roll angles about the sensor frames z-axis, the prototype transfers the initial five conic models fit to the horizon edge coordinates at each orientation.

The identified horizon edge coordinates and conic models fit by the prototype at each roll angle, are detailed in Appendix E; the eccentricity of the identified models is summarised with the box and whiskers chart in Fig. 47 below:

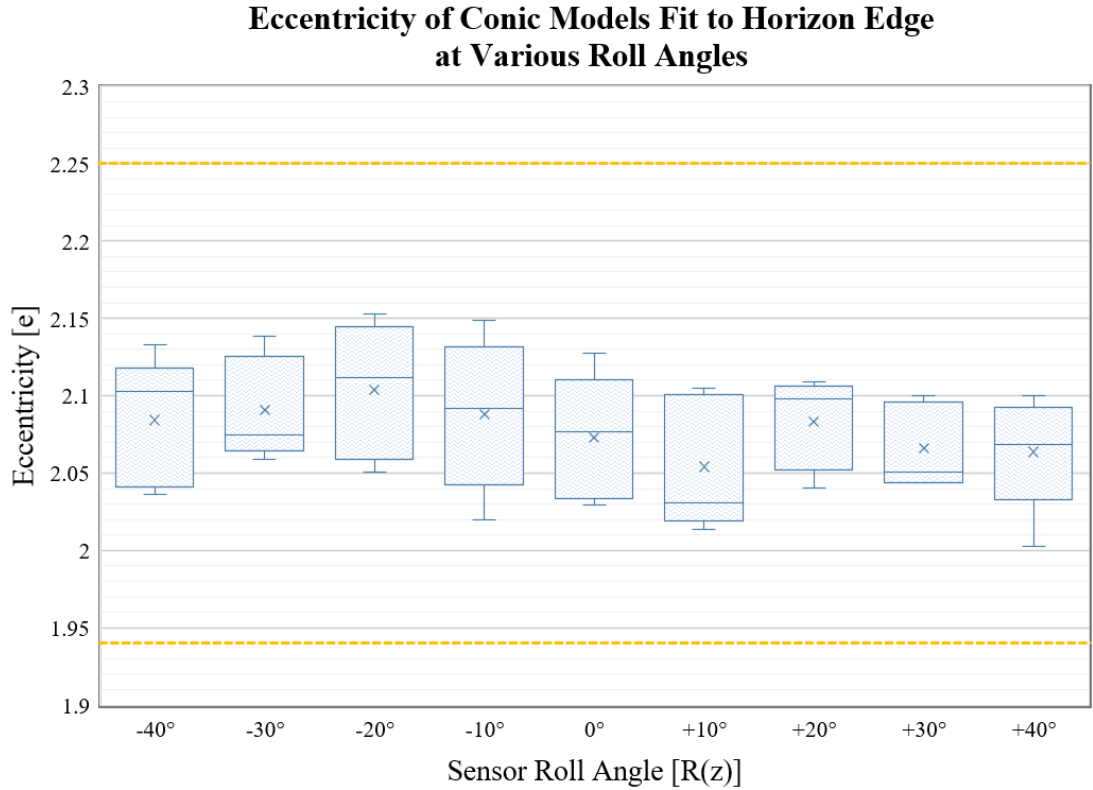


Fig. 47 The eccentricity spread of conic models fit to the test stands horizon edge by the prototype at various roll angles; yellow line depicts bounds of success criteria

Referring to Fig. 47, the prototype horizon sensor was able to accurately determine the correct conic shape of the test stand across all conic models and rotations tested within the stated eccentricity tolerance; therefore, satisfying the success criteria for this requirement.

It was noted that the sub-pixel adjustment appears to have greatly enhanced the performance of the conic fitting, by allowing a tighter inlier tolerance to be stipulated within the RANSAC fitting method. This approach worked well to identify a strong conic model from the adjusted points of the horizon edge contour, and was deemed a primary contributor to the eccentricity accuracy achieved.

3.1.6 [P-6] Attitude Estimation

Statement: The prototype shall perform attitude determination by estimating the relative location of the nadir vector based on the parameters of the identified conic.

Success Criteria:

- ✓ *[Test]:* The prototype captures images of the test stand and transfers the calculated sequence of rotations required to align the sensors bore axis to the nadir vector, within $\pm 5^\circ$ of its expected location; *i.e.* roll about sensors optical axis $[R(z)_{sensorFrame}]$, then pitch along the perpendicularly aligned coordinate frame axis $[R(x)_{sensorFrame}]$.
- ✓ *[Test]:* Rotating the horizon sensor about its bore (roll) by 10° increments in the CW and CCW directions changes the magnitude of the calculated conic rotation in the corresponding direction and within $\pm 5^\circ$ of the physical rotation.
- ✓ *[Test]:* The calculated angle of the conic cutting plane $[\alpha]$ corresponds to the test stands conic shape: $\alpha = 26^\circ \pm 5^\circ$; $\therefore bore\angle nadir = 64^\circ \pm 5^\circ$

The prototype is mounted to the pitch-roll gimbal while viewing the test stands simulated orbital horizon view 25cm from its thermal face. The roll of the gimbal is then adjusted in 10° increments; to avoid the previously discussed ghosting artifacts, the sensor is given approximately 3-5 seconds to adjust to the scene at each new roll angle. The next five attitude estimations from the horizon sensor are then transferred to the host device, along with the captured thermal image and identified edge contour. Each attitude determination received from the prototype is formatted in Euler zx' rotations, represented below as $R(z)$ and $R(x)$ rotations respectively; refer Fig. 26.

3.1.6.1 Results of Attitude Estimation

Referring the results of each roll angle tested in the following sub-sections, the horizon sensor was able to accurately determine the angle of the conic cutting plane, the conics rotation within the image frame, and an estimation of the nadir vectors attitude relative to the sensors reference frame.

Despite a small number of conic rotation outliers in the individual results (discussed in 3.1.6.2), the overall attitude determination functionality of the prototype horizon

sensor performed well; with the average calculated attitude outputs at each roll angle all satisfying the $\pm 5^\circ$ tolerance range for the success criteria of this requirement.

For the sake of brevity, the five attitude estimations at each roll angle are averaged in the sub-section result tables below, with conforming results depicted in green, and non-conforming results depicted in red; each of the individual estimations received from the horizon sensor are detailed in Appendix F.

3.1.6.1.1 -40° Roll Test Result

The prototype's thermal image and detected horizon edge is shown in Fig. 48, the average of the initial five attitude estimation results is summarised in Table 6.

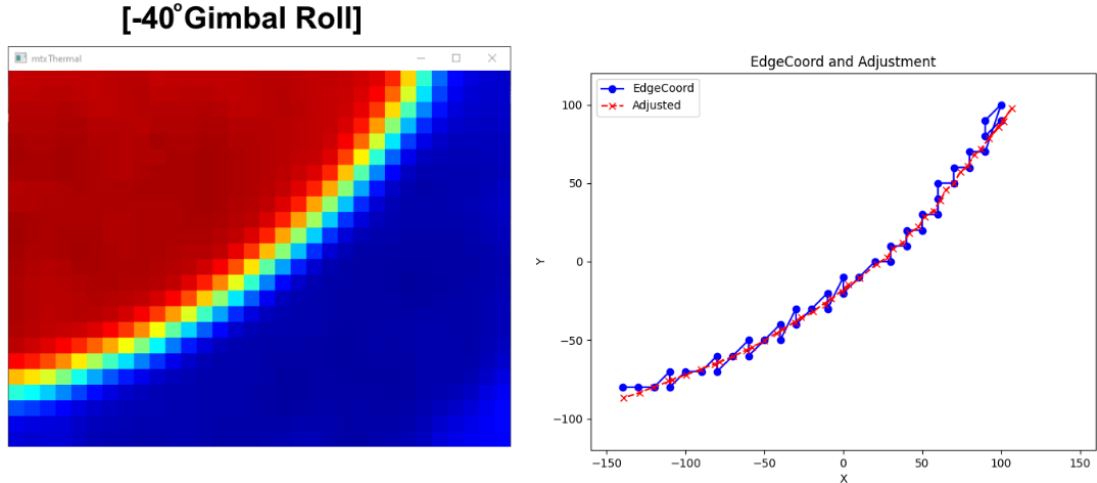


Fig. 48 Sensors thermal image of simulated orbital horizon and detected horizon edge; viewed with -40° z-axis roll in the sensor / gimbal frame

The range of the acceptable success criteria for -40° gimbal roll is:

- ✓ Nadir Alignment Rotations:

$$[R(z)_{sensorFrame} = 40^\circ \pm 5^\circ]; \text{then } [59^\circ \leq R(x)_{sensorFrame} \leq 69^\circ]$$

- ✓ *conicRotation* = $-50^\circ \pm 5^\circ$

TABLE 6 Average of initial results received from prototype while at -40° z-axis roll in the sensor / gimbal frame; refer Appendix F for individual results

5 Initial Results	Cutting Plane $[\alpha]$ ($26^\circ \pm 5^\circ$)	bore \angle nadir ($64^\circ \pm 5^\circ$)	Conic Rotation (from x-axis)	Align Sensor Bore Axis to Nadir Vector
Avg.	25.25°	64.75°	-53.75°	R(z): 36.245° ; then R(x): 64.756°

3.1.6.1.2 -30° Roll Test Results

The prototype's thermal image and detected horizon edge is shown in Fig. 49, the average of the initial five attitude estimation results is summarised in Table 7.

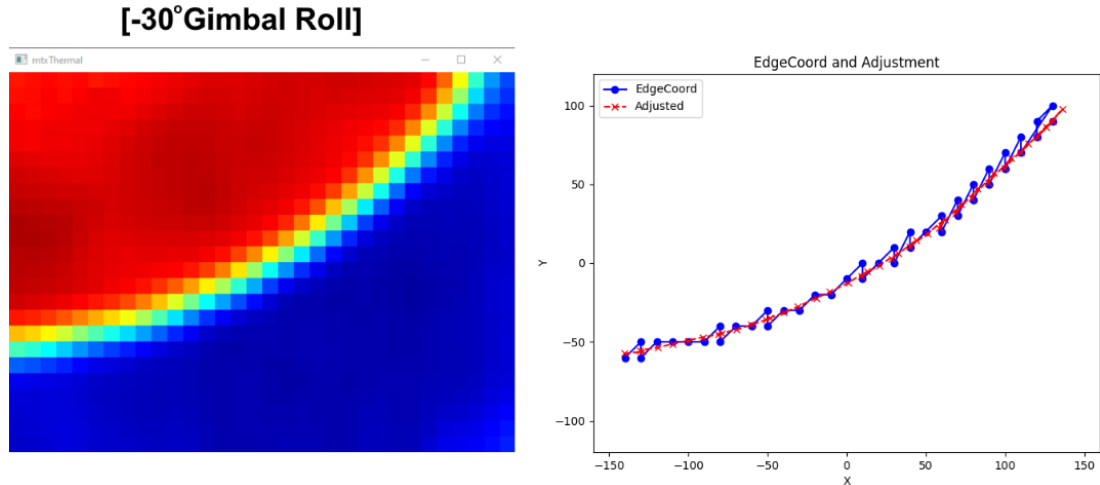


Fig. 49 Sensors thermal image of simulated orbital horizon and detected horizon edge; viewed with -30° z-axis roll in the sensor / gimbal frame

The range of the acceptable success criteria for -30° gimbal roll is:

- ✓ Nadir Alignment Rotations:

$$[R(z)_{sensorFrame} = 30^\circ \pm 5^\circ]; \text{then } [59^\circ \leq R(x)_{sensorFrame} \leq 69^\circ]$$

- ✓ $conicRotation = -60^\circ \pm 5^\circ$

TABLE 7 Average of initial results received from prototype while at -30° z-axis roll in the sensor / gimbal frame; refer Appendix F for individual results

5 Initial Results	Cutting Plane $[\alpha]$ ($26^\circ \pm 5^\circ$)	$bore\angle nadir$ ($64^\circ \pm 5^\circ$)	Conic Rotation (from x-axis)	Align Sensor Bore Axis to Nadir Vector
Avg.	24.89°	65.11°	-63.13°	R(z): 26.874°; then R(x): 65.107°

3.1.6.1.3 -20° Roll Test Result

The prototype's thermal image and detected horizon edge is shown in Fig. 50, the average of the initial five attitude estimation results is summarised in Table 8.

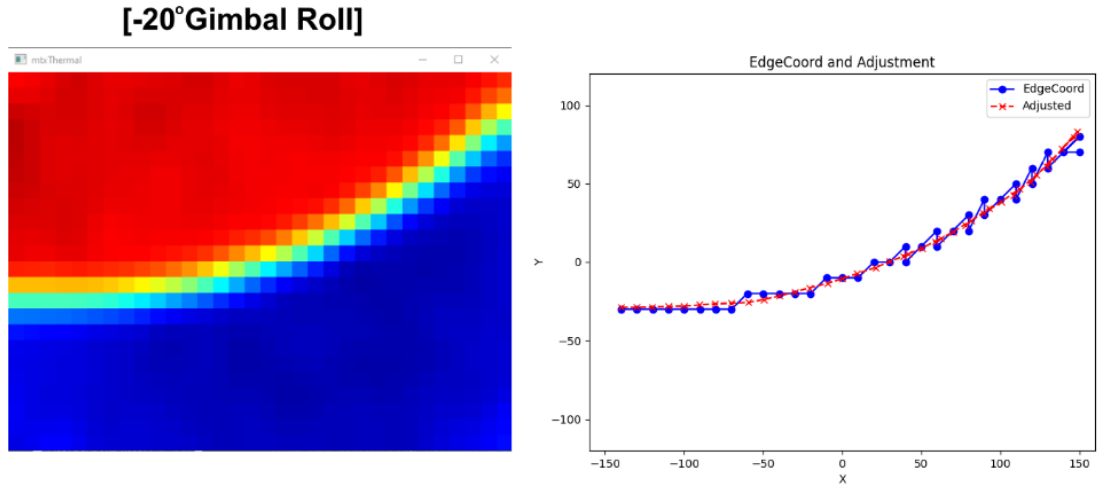


Fig. 50 Sensors thermal image of simulated orbital horizon and detected horizon edge; viewed with -20° z-axis roll in the sensor / gimbal frame

The range of the acceptable success criteria for -20° gimbal roll is:

- ✓ Nadir Alignment Rotations:

$$[R(z)_{sensorFrame} = 20^\circ \pm 5^\circ]; \text{then } [59^\circ \leq R(x)_{sensorFrame} \leq 69^\circ]$$

- ✓ $conicRotation = -70^\circ \pm 5^\circ$

TABLE 8 Average of initial results received from prototype while at -20° z-axis roll in the sensor / gimbal frame; refer Appendix F for individual results

5 Initial Results	Cutting Plane $[\alpha]$ ($26^\circ \pm 5^\circ$)	bore∠nadir ($64^\circ \pm 5^\circ$)	Conic Rotation (from x-axis)	Align Sensor Bore Axis to Nadir Vector
Avg.	24.06°	65.94°	-73.37° (incl. 2 outliers)	R(z): 16.634°; then R(x): 65.94°

3.1.6.1.4 -10° Roll Test Result

The prototype's thermal image and detected horizon edge is shown in Fig. 51, the average of the initial five attitude estimation results is summarised in Table 9.

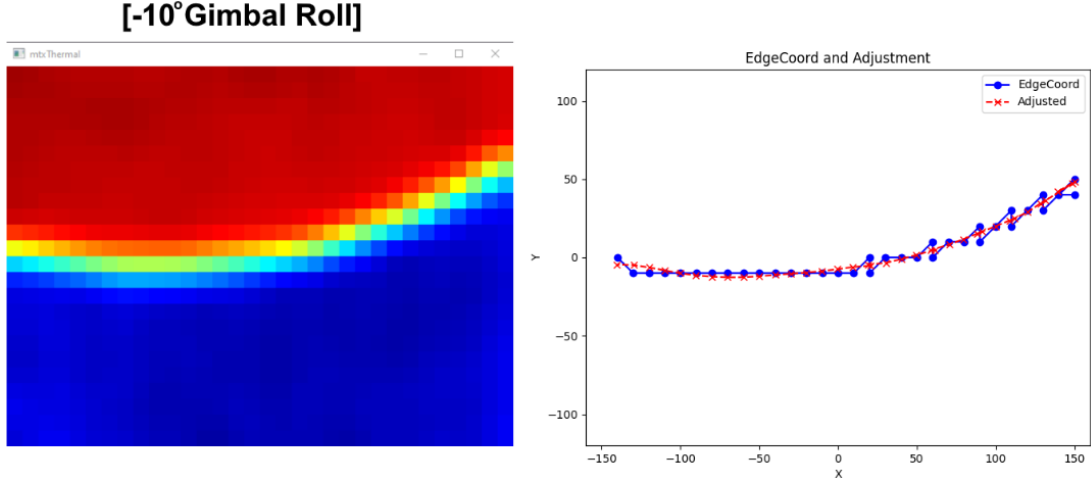


Fig. 51 Sensors thermal image of simulated orbital horizon and detected horizon edge; viewed with -10° z-axis roll in the sensor / gimbal frame

The range of the acceptable success criteria for -10° gimbal roll is:

- ✓ Nadir Alignment Rotations:

$$[R(z)_{sensorFrame} = 10^\circ \pm 5^\circ]; \text{then } [59^\circ \leq R(x)_{sensorFrame} \leq 69^\circ]$$

- ✓ $conicRotation = -80^\circ \pm 5^\circ$

TABLE 9 Average of initial results received from prototype while at -10° z-axis roll in the sensor / gimbal frame; refer Appendix F for individual results

5 Initial Results	Cutting Plane $[\alpha]$ ($26^\circ \pm 5^\circ$)	bore \angle nadir ($64^\circ \pm 5^\circ$)	Conic Rotation (from x-axis)	Align Sensor Bore Axis to Nadir Vector
Avg.	24.99°	65.01°	-81.42° (incl. 1 outlier)	R(z): 8.58°; then R(x): 65.011°

3.1.6.1.5 0° Roll Test Result

The prototype's thermal image and detected horizon edge is shown in Fig. 52, the average of the initial five attitude estimation results is summarised in Table 10.

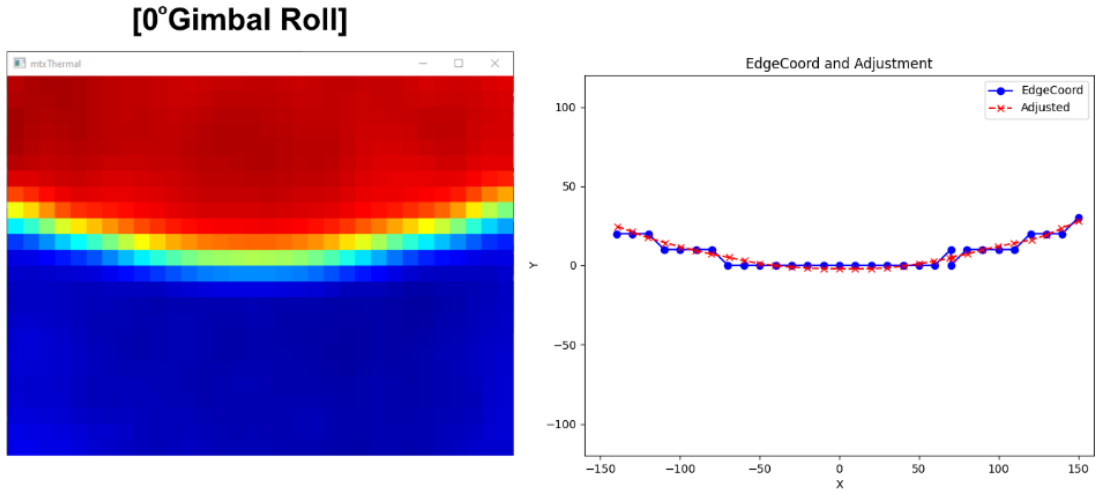


Fig. 52 Prototype thermal image of simulated orbital horizon and detected horizon edge; viewed with 0° z-axis roll in the sensor / gimbal frame

In the case of no gimbal roll, the range of the acceptable success criteria is:

- ✓ Nadir Alignment Rotations:

$$[R(z)_{sensorFrame} = 0^\circ \pm 5^\circ]; \text{ then } [59^\circ \leq R(x)_{sensorFrame} \leq 69^\circ]$$

- ✓ $85^\circ \leq |conicRotation| \leq 90^\circ$

TABLE 10 Average of initial results received from prototype while at 0° z-axis roll in the sensor / gimbal frame; refer Appendix F for individual results

5 Initial Results	Cutting Plane $[\alpha]$ ($26^\circ \pm 5^\circ$)	bore∠nadir ($64^\circ \pm 5^\circ$)	Conic Rotation (from x-axis)	Align Sensor Bore Axis to Nadir Vector
Avg.	25.9°	64.1°	89.17°	R(z): -0.744°; then R(x): 64.101°

3.1.6.1.6 +10° Roll Test Result

The prototype's thermal image and detected horizon edge is shown in Fig. 53, the average of the initial five attitude estimation results is summarised in Table 11.

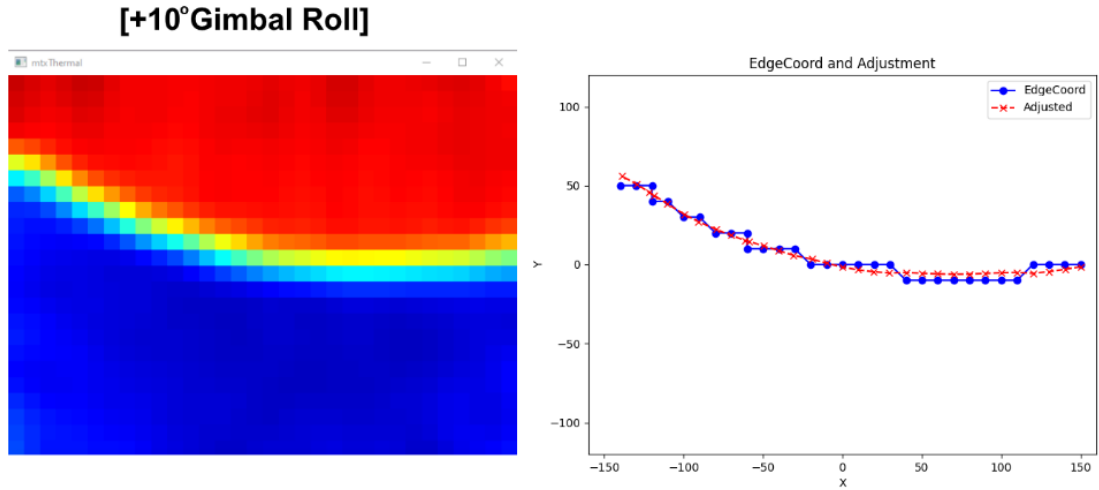


Fig. 53 Sensors thermal image of simulated orbital horizon and detected horizon edge; viewed with $+10^\circ$ z-axis roll in the sensor / gimbal frame

The range of the acceptable success criteria for $+10^\circ$ gimbal roll is:

- ✓ Nadir Alignment Rotations:

$$[R(z)_{sensorFrame} = -10^\circ \pm 5^\circ]; \text{ then } [59^\circ \leq R(x)_{sensorFrame} \leq 69^\circ]$$

- ✓ $conicRotation = 80^\circ \pm 5^\circ$

TABLE 11 Average of initial results received from prototype while at $+10^\circ$ z-axis roll in the sensor / gimbal frame; refer Appendix F for individual results

5 Initial Results	Cutting Plane $[\alpha]$ ($26^\circ \pm 5^\circ$)	bore \angle nadir ($64^\circ \pm 5^\circ$)	Conic Rotation (from x-axis)	Align Sensor Bore Axis to Nadir Vector
Avg.	26.95°	63.05°	75.55° (incl. 3 outliers)	R(z): -14.454°; then R(x): 63.049°

3.1.6.1.7 +20° Roll Test Result

The prototype's thermal image and detected horizon edge is shown in Fig. 54, the average of the initial five attitude estimation results is summarised in Table 12.

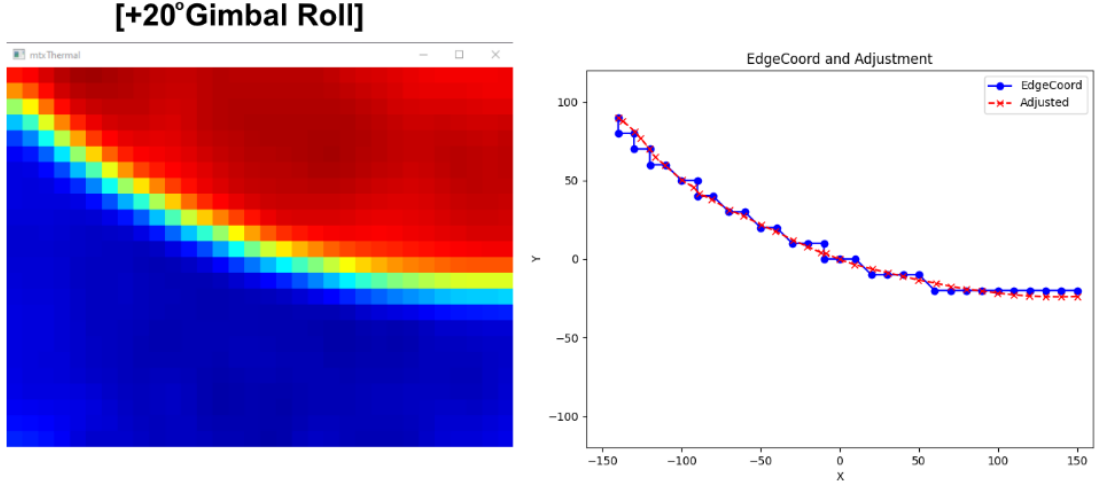


Fig. 54 Sensors thermal image of simulated orbital horizon and detected horizon edge; viewed with $+20^\circ$ z-axis roll in the sensor / gimbal frame

The range of the acceptable success criteria for $+20^\circ$ gimbal roll is:

- ✓ Nadir Alignment Rotations:

$$[R(z)_{sensorFrame} = -20^\circ \pm 5^\circ]; \text{then } [59^\circ \leq R(x)_{sensorFrame} \leq 69^\circ]$$

- ✓ $conicRotation = 70^\circ \pm 5^\circ$

TABLE 12 Average of initial results received from prototype while at $+20^\circ$ z-axis roll in the sensor / gimbal frame; refer Appendix F for individual results

5 Initial Results	Cutting Plane $[\alpha]$ ($26^\circ \pm 5^\circ$)	bore∠nadir ($64^\circ \pm 5^\circ$)	Conic Rotation (from x-axis)	Align Sensor Bore Axis to Nadir Vector
Avg.	25.36°	64.64°	70.52° (incl. 1 outlier)	R(z): -19.475°; then R(x): 64.639°

3.1.6.1.8 $+30^\circ$ Roll Test Result

The prototype's thermal image and detected horizon edge is shown in Fig. 55, the average of the initial five attitude estimation results is summarised in Table 13.

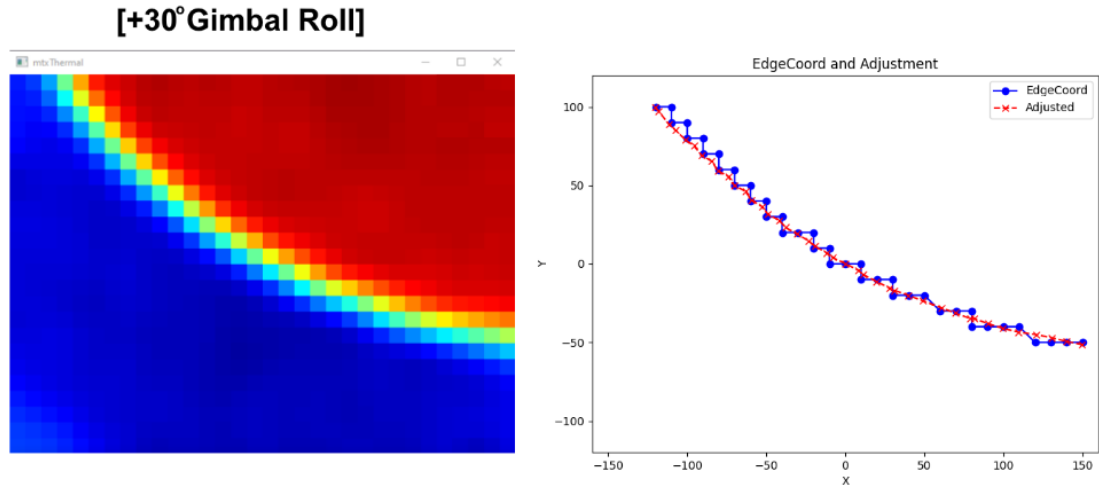


Fig. 55 Sensors thermal image of simulated orbital horizon and detected horizon edge; viewed with $+30^\circ$ z-axis roll in the sensor / gimbal frame

The range of the acceptable success criteria for $+30^\circ$ gimbal roll is:

- ✓ Nadir Alignment Rotations:

$$[R(z)_{sensorFrame} = -30^\circ \pm 5^\circ]; \text{then } [59^\circ \leq R(x)_{sensorFrame} \leq 69^\circ]$$

- ✓ $conicRotation = 60^\circ \pm 5^\circ$

TABLE 13 Average of initial results received from prototype while at $+30^\circ$ z-axis roll in the sensor / gimbal frame; refer Appendix F for individual results

5 Initial Results	Cutting Plane $[\alpha]$ ($26^\circ \pm 5^\circ$)	bore \angle nadir ($64^\circ \pm 5^\circ$)	Conic Rotation (from x-axis)	Align Sensor Bore Axis to Nadir Vector
Avg.	26.33°	63.67°	60.04°	R(z): -29.955°; then R(x): 63.666°

3.1.6.1.9 $+40^\circ$ Roll Test Result

The prototype's thermal image and detected horizon edge is shown in Fig. 56, the average of the initial five attitude estimation results is summarised in Table 14.

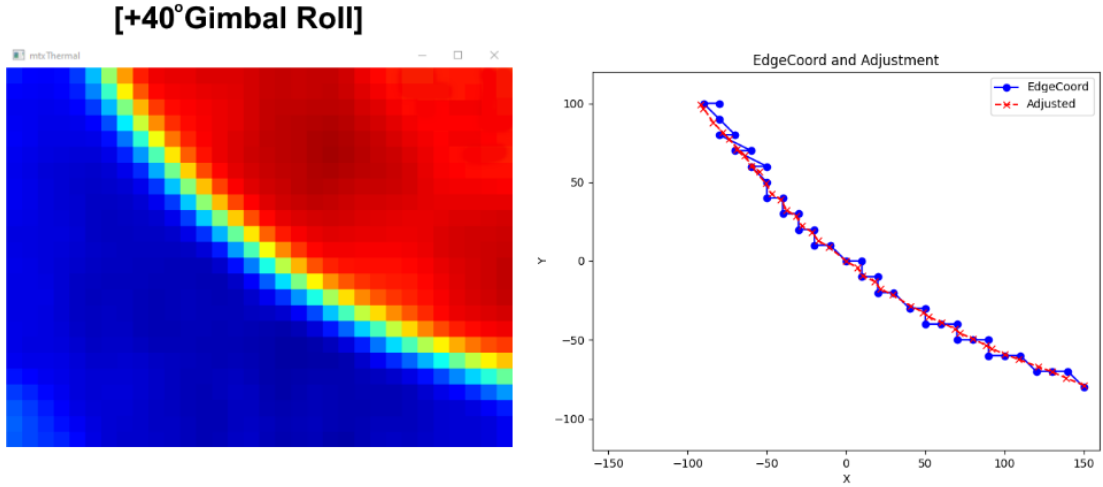


Fig. 56 Sensors thermal image of simulated orbital horizon and detected horizon edge; viewed with $+40^\circ$ z-axis roll in the sensor / gimbal frame

The range of the acceptable success criteria for $+40^\circ$ gimbal roll is:

- ✓ Nadir Alignment Rotations:

$$[R(z)_{sensorFrame} = -40^\circ \pm 5^\circ]; \text{ then } [59^\circ \leq R(x)_{sensorFrame} \leq 69^\circ]$$

- ✓ $conicRotation = 50^\circ \pm 5^\circ$

TABLE 14 Average of initial results received from prototype while at $+40^\circ$ z-axis roll in the sensor / gimbal frame; refer Appendix F for individual results

5 Initial Results	Cutting Plane $[\alpha]$ ($26^\circ \pm 5^\circ$)	bore∠nadir ($64^\circ \pm 5^\circ$)	Conic Rotation (from x-axis)	Align Sensor Bore Axis to Nadir Vector
Avg.	26.44°	63.56°	53.26°	R(z): -36.739°; then R(x): 63.555°

3.1.6.2 Attitude Estimation Discussion

All individual attitude estimations received from the horizon sensor correctly identifying the angle of the conic cutting plane $[\alpha]$, and the bore to nadir alignment rotation $[R(x)]$ within the stated tolerance of the success criteria.

Out of 45 total attitude determinations, only 7 showed non-conforming results, all caused by the estimated conic rotation within the image frame (therefore affecting the calculated alignment rotation $[R(z)]$). As the number of coordinates in the edge contour is limited, these discrepancies appear to be due to the large number of valid conic models, at slightly different rotations, that can be well-fit to the limited edge

data; an illustration of this phenomenon from two models fit to the contour points of the -20° gimbal roll is provided in Fig. 57.

Given that the rotation of the conic is better defined with a wider spread of sample points along its edge, it is proposed that a wider sensor FOV may be able to provide more information about the horizons projected conic arc in the image frame, and therefore its relative rotation within the scene.

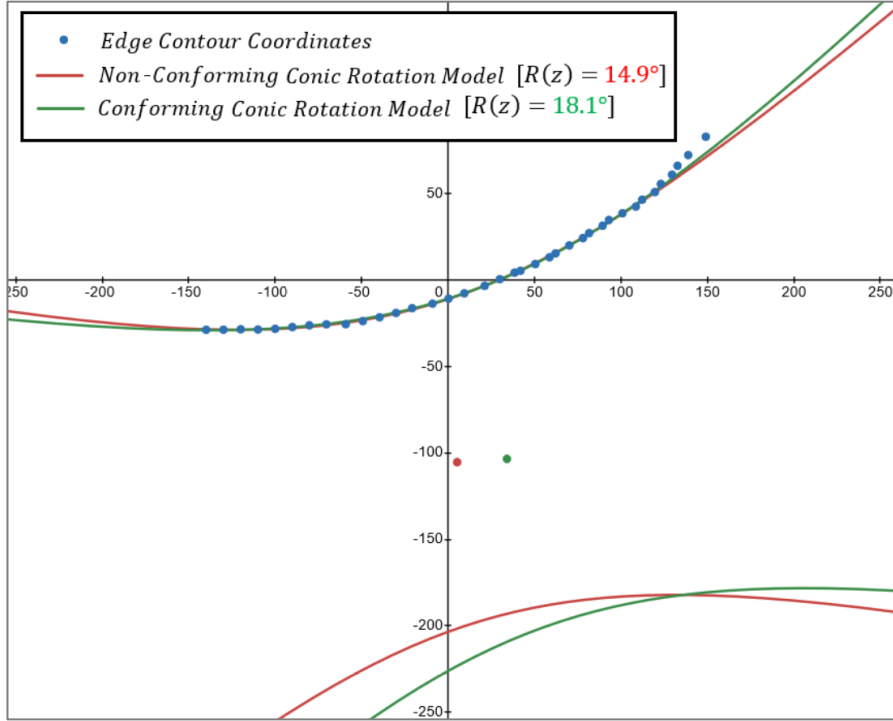


Fig. 57 Illustration of conic rotation discrepancy from two well-fit models; contour points and models taken from the -20° gimbal roll dataset [$R(z)_{accepted} = 20^\circ \pm 5^\circ$]

Although the prototype performed well with respect to the $\pm 5^\circ$ tolerance ranges of the acceptance criteria, the attitude determination performance of a real orbital craft is likely to require a much more refined accuracy and precision tolerance.

While the sub-pixel correction method improved the edge detection performance of the 32x24px low-resolution sensor used in the prototype (and was deemed a key contributor to the attitude determination tolerance range it was able to achieve), the additional scene information granted from a higher resolution infrared imaging sensor is likely to aid in improving both the accuracy of the sub-pixel corrections, and the sensors overall attitude estimation performance. It is therefore proposed that a higher resolution infrared sensor may have allowed for the selection of criteria with a narrower range of accepted tolerances.

3.1.7 [P-7] Power Source

Statement: The prototype shall accept and operate from an unregulated 4-18V DC supply; *i.e.* analogous to a typical direct battery supply from the Electrical Power Subsystem (EPS) of a CubeSat.

Success Criteria:

- ✓ *[Test]:* Incrementally vary prototypes supply in 1V steps within expected input range and confirm correct board operation via continuous program serial output to host machine.

To test the voltage range requirement, the prototype was connected to a standard benchtop DC power supply, which had its output incrementally adjusted from 18V to 4V. During this, the prototype would process its view of the test stand. Its continuous operation during the test was confirmed by sending its calculated results, as well as an incrementing timer from the microcontrollers last reset, to a host device.

Table 15 below shows the applied voltage, and the program timer at the point the voltage was reduced (approximately 20 seconds operating at each voltage step).

TABLE 15 Prototype supply range verification

Supply Voltage	Program Reset Timer & State	Supply Voltage	Program Reset Timer & State
18V	21,206ms; [Operating OK]	10V	184,189ms; [Operating OK]
17V	35,936ms; [Operating OK]	9V	210,894ms; [Operating OK]
16V	54,248ms; [Operating OK]	8V	235,730ms; [Operating OK]
15V	74,390ms; [Operating OK]	7V	259,567ms; [Operating OK]
14V	95,671ms; [Operating OK]	6V	285,923ms; [Operating OK]
13V	117,373ms; [Operating OK]	5V	308,363ms; [Operating OK]
12V	140,400ms; [Operating OK]	4V	335,052ms; [Operating OK]
11V	162,011ms; [Operating OK]		

The prototype was able to continuously operate from a varied supply input within the given range, and therefore satisfies this requirement.

Considering the 4-36V input specification of the prototypes designed supply regulation circuit, its ability to operate in this range does not come as a surprise, however it is still

a confirmation that the circuit was configured correctly to meet this specification, and successfully supply the horizon sensor while it is operating.

Despite the success criteria being achieved, the DC input from the benchtop supply does contain some minor signal conditioning, and further rundown testing is therefore recommended with a BMS (Battery Management System) managed LiPo pack in a 1S to 4S configuration.

3.1.8 [P-8] External Interface

Statement: The prototype shall interface externally via serial for calculated outputs, sensor state flags, and debug messages; *i.e.* emulating rudimentary data transfers to the CubeSat's ADCS.

Success Criteria:

- ✓ *[By Inspection]:* The prototype interfaces and sends stated data to connected port on host device via serial UART.

The external interface to the host device viewing software was used extensively throughout testing, and was a pivotal aspect of the design that allowed fast iterations to the sensor's configuration / parameter tuning, and direct connection to the debugging functionality that was setup within the prototype's firmware; see example Fig. 58; therefore, satisfying this requirement.

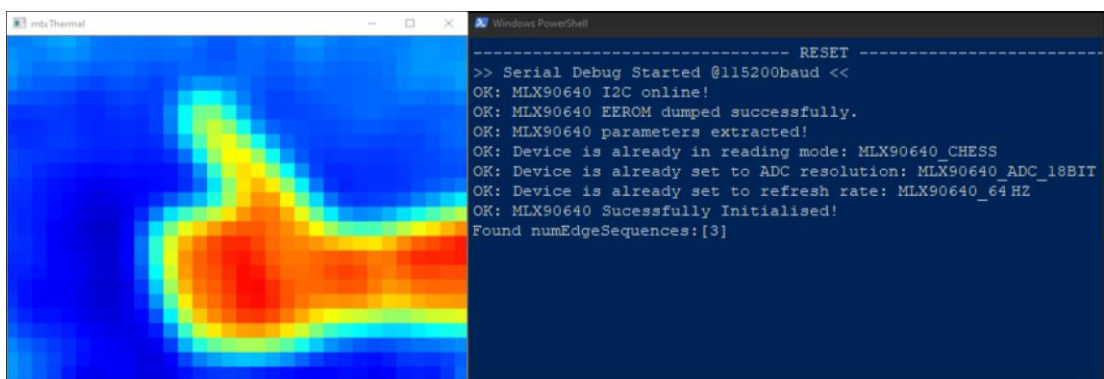


Fig. 58 Host device thermal rendering and debug display of serial output from prototype horizon sensor

3.2 Orbital View Test Stand Verification

The results and discussion of each project requirement relating to the orbital view test stand have been grouped into the following sub-sections; a summary of the outcomes is provided in Table 16.

TABLE 16 Orbital View Test Stand Requirement Verification Results

Req. No.	Name	Result	On	By
[P-9]	Simulated Orbital View	Success criteria met contingent assumption on thermal transmission through test stand cold plate. Sensitivity range of available calibrated thermal camera unable to explicitly confirm $\Delta\text{C} \geq 200^\circ\text{C}$ success criteria. Sub-zero temperatures determined to likely not be required for prototype sensor testing.	9-Oct-2024	A.Janssen
[P-10]	Positional Pitch-Roll Gimbal	All success criteria met.	9-Oct-2024	A.Janssen
[P-11]	Test Stand Functional Range	All success criteria met.	9-Oct-2024	A.Janssen

3.2.1 [P-9] Simulated Orbital View

Statement: A proxy infrared scene of Earth's conic horizon shall be built that approximates what is seen from an LEO orbit altitude of 600-800km, with a $55^\circ \times 35^\circ$ sensor FOV, while in the nominal orientation (refer Fig. 14).

Success Criteria:

- ✓ *[Test]:* Confirm by measurement horizon arc represents a conic with eccentricity between 1.94 (800km altitude) and 2.25 (600km altitude); e.g. a conic apex [D1] of 21-24mm for a 380mm span simulate scene, refer Eq. (17).

- ✓ [Test]: Confirm a distinct thermal edge between the simulated Earth and space background using calibrated thermal camera; $\Delta^{\circ}\text{C} \geq 200^{\circ}\text{C}$.

The conic representing the Earth horizon was measured to have an FOV bound conic apex of approximately 23mm, therefore simulating a $\sim 700\text{km}$ orbit at the test stands scaled view, and satisfying the projective discriminant criteria; Fig. 59.



Fig. 59 Test stand FOV bound conic apex measurement

While testing the prototype with the simulated orbital view, the reservoir that cools the plate representing the space background was filled with liquid nitrogen (LN_2), see Fig. 60, while the front plate representing the Earth silhouette was heated to $\sim 39^{\circ}\text{C}$.



Fig. 60 Test stand receiving liquid nitrogen to cool the proxy space background plate

Imaging the test stand with the prototype horizon sensor and a calibrated thermal camera, the test stand was able to successfully produce a distinct thermal edge in the generated images; see Fig. 61.

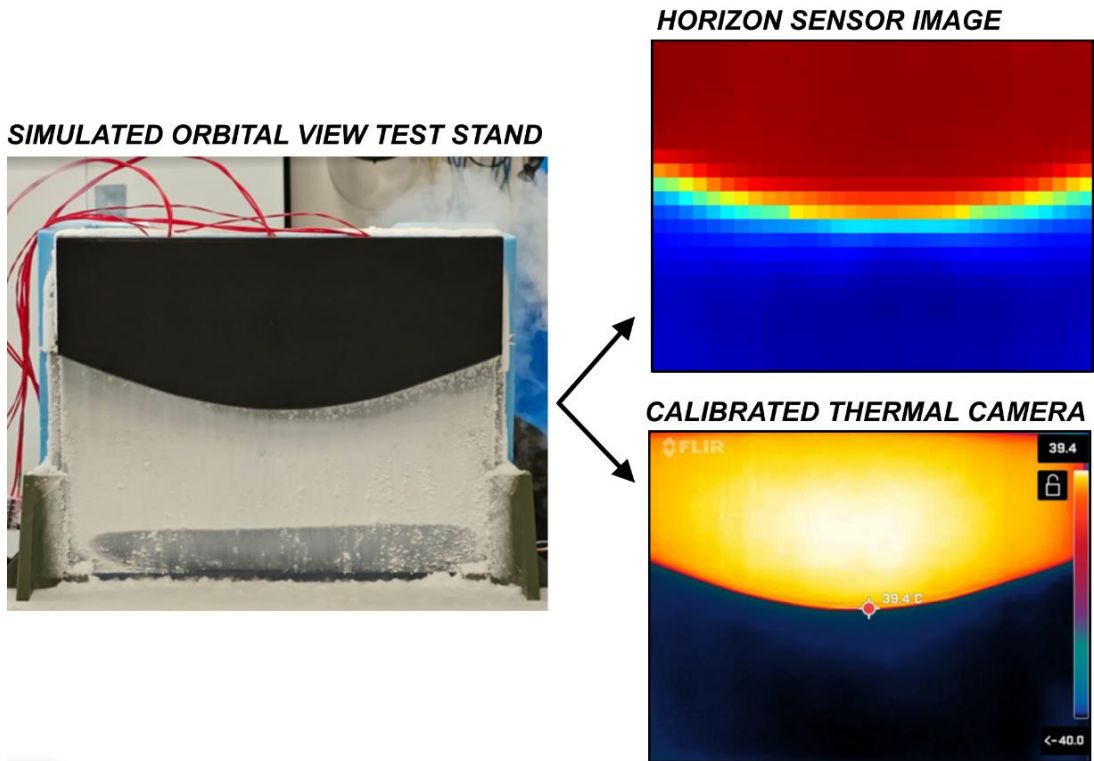


Fig. 61 Simulated orbital view test stand distinct thermal edge verification

Achieving a distinct thermal edge representing the horizon of the simulated orbital view was a key aspect of the test stands design. The approach implemented to evenly heat and thermally insulate the two plates, as well as the positioning of the heated Earth horizon at the top of the test stand, appear to have worked well to alleviate both the hot spot and poorly defined edge issues encountered by [18] and [19].

Unfortunately, the sensitivity range of the calibrated thermal camera that was available during testing was not able to accurately detect temperatures below -40°C . Therefore, the $\Delta^{\circ}\text{C} \geq 200^{\circ}\text{C}$ component of this requirement was not able to be explicitly confirmed. However, noting that the surface of the heated front plate was measured at $\sim 39^{\circ}\text{C}$, and the LN_2 at atmospheric pressure cooling the rear plate was estimated at $\sim -196^{\circ}\text{C}$ [40]. The $\Delta^{\circ}\text{C}$ between hot and cold plates does satisfy the success criteria with an assumption that heat gained crossing from the rear to front face of the 8mm thick aluminium cold plate was $< 35^{\circ}\text{C}$; *i.e.* an assumed cold plate front face temperature of $\leq -161^{\circ}\text{C}$, $\therefore 39^{\circ}\text{C} - (-161^{\circ}\text{C}) = \sim 200^{\circ}\text{C} \Delta$ between plates.

Contingent on the cold plate temperature assumption above, the simulated representation of the infrared orbital view was compared to the expected temperature difference as seen from orbit, shown in Table 17 below.

TABLE 17 Comparison of orbital view temperatures vs simulated (*contingent cold plate temperature transfer assumption)

	Background of Space °C	Earth °C	Δ°C
Real-World Average	-270°C [5][39]	15°C [8]	285°C
Test Stand Simulation*	~ - 161°C	~39°C	200°C
<i>Real World Δ:</i>	+109°C	+24°C	-85°C

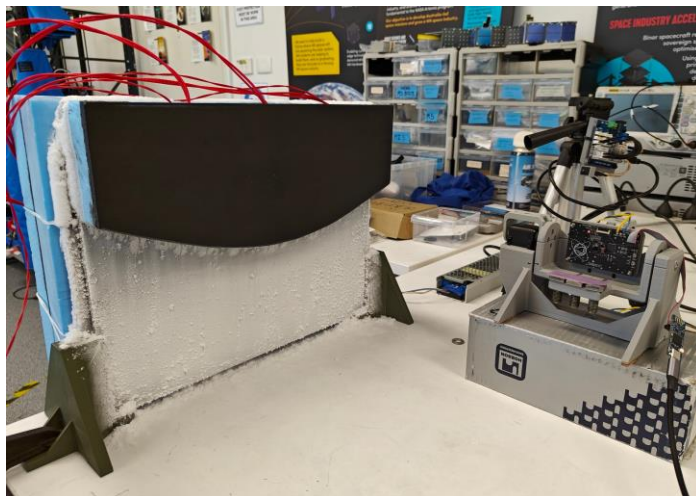


Fig. 62 Orbital view test stand, prototype sensor, and pitch-roll gimbal

Although the estimated $\Delta^{\circ}\text{C}$ achieved by the test stand was within 85°C of what is expected from orbit, it was noted throughout testing that the horizon sensor was still able to accurately determine the test stands distinct horizon edge with only a small difference between the hot and cold plate temperatures; *e.g.* $\Delta^{\circ}\text{C} \geq 15^{\circ}\text{C}$.

Despite the benefits of performing the test with parameters analogous to what would be seen from orbit, the MLX90640 (akin to the calibrated thermal camera) also does not have reliable sensitivity to temperatures below -40°C [30]. Therefore, it is proposed that the extreme cooling of the test stands cold plate was not a critical requirement to test the prototype horizon sensors functionality; and a similar result can be achieved by simply leaving the cold plate at room temperature, and heating the Earth plate until a distinct edge is evident to the sensor.

Since the prototype sensors firmware perceives the infrared scene in relative terms, the difference in uniform temperature across both plates is what is key for its edge detection performance. The chosen temperature difference between plates is therefore better selected for testing the sensor's response characteristics to changes in thermal radiation; *i.e.* rapid movement artifacts, image refresh rate, ghosting *etc.*

3.2.2 [P-10] Positional Pitch-Roll Gimbal

Statement: While viewing the proxy infrared scene, the horizon sensor prototype shall be centrally mounted to a controllable pitch and roll gimbal with a positional pitch and roll accuracy resolution <0.5°.

Success Criteria:

- ✓ *[By Inspection]:* Actuators directly tied to the pitch and roll structures are within positional accuracy tolerance, confirmed via manufacturer datasheet.

The pitch-roll gimbal's two actuators that position the sensor while it views the simulated horizon scene are Dynamixel AX-12A robotics servos. These servos position the prototype via direct links to the pitch and roll structures of the gimbal, and have a 0.29° positional accuracy [41]. Based on this, the project requirement is therefore deemed satisfied.

3.2.3 [P-11] Test Stand Functional Range

Statement: The proxy infrared scene shall extend to allow the prototype a minimum 90° ($\pm 45^\circ$) roll and 10° ($\pm 5^\circ$) pitch window without exceeding the edge of the simulated view (accounting also the diagonal of the sensors image under roll conditions).

Success Criteria:

- ✓ *[By Inspection]:* With the sensor centrally positioned 25cm from the thermal face of the test stand, the FOV is bound within test stand at extents of roll and pitch allowance; confirmed by visual inspection of intensity uniformity at edges of generated thermal image.

The horizon sensor is mounted to the pitch-roll gimbal while viewing the simulated orbital horizon test stand 25cm from its thermal face. The extents of the test stand were examined by analysing the prototypes output while at the designed $\pm 5^\circ$ pitch and $0^\circ \pm 45^\circ$ roll allowance.

The thermal image and identified edge at each orientation was then transferred from the prototype to a host device to be rendered; the results are shown in Fig. 63, Fig. 64, and Fig. 65 below, with x-axis pitch and z-axis roll angles given with respect to the gimbals coordinate frame (refer Fig. 35).

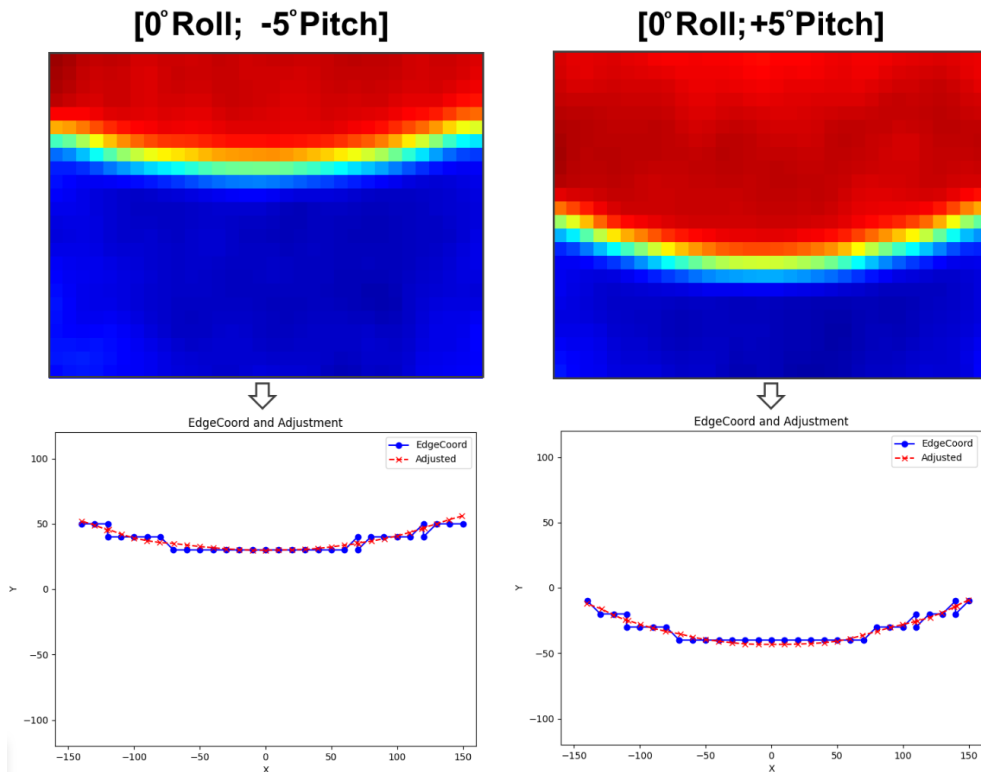


Fig. 63 Test stand functional range verification, pitch-roll gimbal at 0° roll and $\pm 5^\circ$ pitch

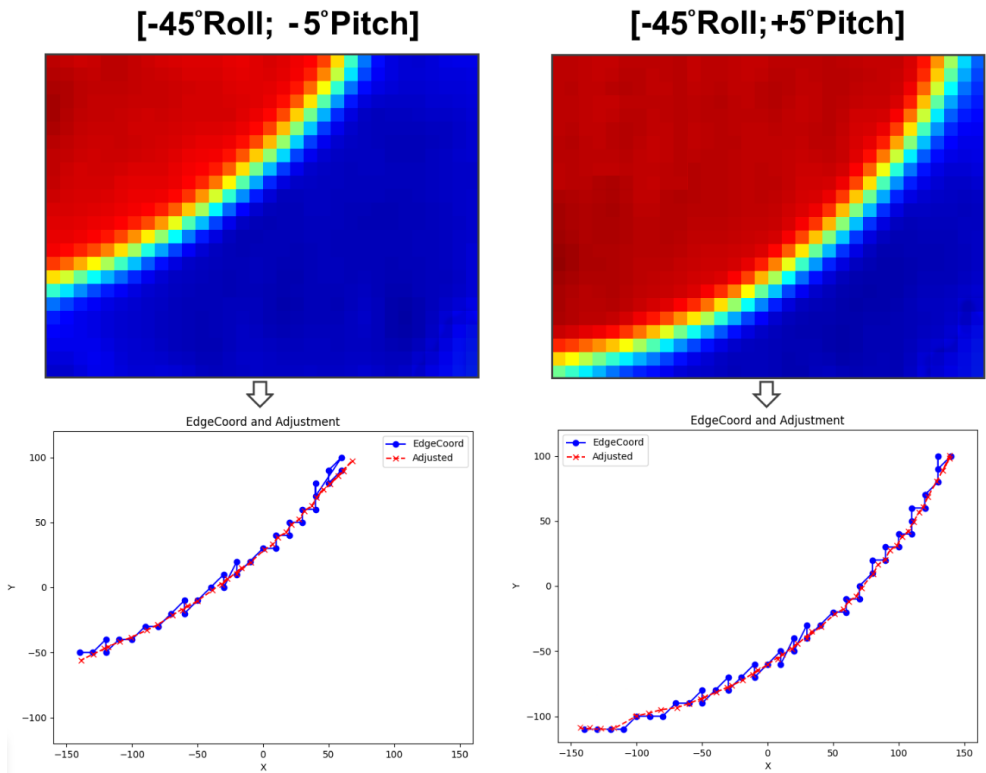


Fig. 64 Test stand functional range verification, pitch-roll gimbal at -45° roll and $\pm 5^\circ$ pitch

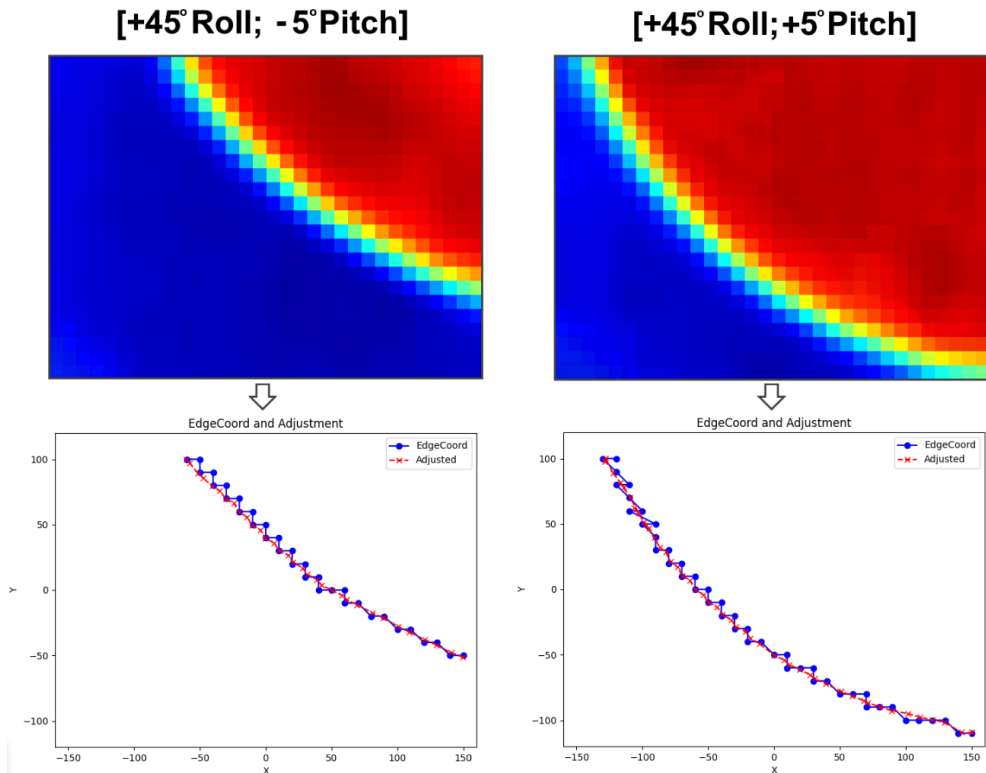


Fig. 65 Test stand functional range verification, pitch-roll gimbal at $+45^\circ$ roll and $\pm 5^\circ$ pitch

Referring to the figures above, the edges and diagonal corners of the generated thermal images are uniform, and don't appear to be erroneously picking up infrared measurements from above or below the face of the test stand. Therefore, the prototypes' view of the test stand is deemed to be bound within the extents of the designed pitch and roll allowance, and satisfies the success criteria for this requirement.

Although a larger pitch allowance on the test stand was a preference during design, a challenge of building a representative orbital horizon view on a 2D plane is that pitch of the craft cannot be accurately replicated. That is to say, while in orbit the conic horizon shape in the sensors image frame changes as the craft is pitched towards or away from the nadir vector, while the horizon plate of the test stand is cut to a fixed conic shape.

This was another factor that contributed to the limited pitch allowance given in this test stands design; in addition to the plate sizes available to construct the test stands view. An alternative design for the test stand that may perform better in this regard is introduced in 5.3.

4. Conclusions

The prototype infrared horizon sensor was able to perform attitude determination and estimate the relative location of the nadir vector to within $\pm 5^\circ$ of the test stands simulated location. The implementation of subpixel edge corrections using the Zernike polynomials enhanced the 32x24px thermal imaging sensor's ability to accurately perceive the distinct edges in the scene, allowing tighter inlier tolerances to be stipulated, and resulting in performance that may be expected of a sensor with a much higher resolution. To the authors knowledge, this is the first time this sub-pixel correction technique has been applied to infrared images in the context of horizon detection for attitude determination.

The test stand worked well to evaluate the thermal detectors utility, and its design alleviated many of the challenges in creating a distinct horizon edge encountered by similar research. It was also proposed that sub-zero cooling of the space background representation was not a requirement to test the sensors general edge detection and attitude determination performance.

Despite the sensor meeting all stated attitude determination tolerance ranges, the slow response to thermal change inherent to the thermal detector class of infrared sensors was noted as an area that requires further investigation; this is particularly important in the context of a spacecraft experiencing high roll rates / tumble scenarios.

In conclusion, this paper contributes to the field of infrared horizon detection research, with particular context given to resource-limited small satellites, such as CubeSats, and design considerations required of a working infrared horizon sensor prototype.

By adapting research from visible light cameras to infrared sensors, this paper was able to illustrate the advantages of orbital horizon detection in the thermal band, while enhancing the horizon detection precision of the low-resolution infrared sensors. The findings highlight the potential to optimise existing space systems for more efficient and reliable satellite navigation.

This work not only addresses a key challenge of low-resolution infrared horizon detection, but hopefully paves the way for future innovations in small-satellite technologies.

5. Suggested Future Work

The sections below detail a few recommendations for areas to investigate in future research / revisions of the work completed in this paper. This project is open-source, and available for collaboration at [44].

5.1 Component Selection

The limited 32x24px and $55^\circ \times 35^\circ$ FOV of the MLX90640-BAB resulted in only a narrow section of the conic horizon shape being visible to the sensor, and is deemed to have contributed to the minor inconsistencies in the rotations of valid conics that could be fit to the adjusted edge data. In 3.1.6.2, it was proposed that a wider FOV infrared sensor with a higher resolution may have improved the sub-pixel edge detection and attitude determination performance of the prototype; it is recommended this be investigated, along with the effects a wider FOV has in the context of picking up additional ‘non-Earth-horizon’ bodies in the background of the image frame (*e.g.* the Sun and Moon). Additionally, any new sensor should be investigated for the sub-paging behaviour discussed in 3.1.2, and other temporal artifacts inherent to the response rate of thermal detector type infrared sensors; *i.e.* when their view of the scene rapidly changes, as is the case when the craft is rapidly rotating.

Although the prototype was able to run the mtxCV firmware within the limited 512KB of assigned memory, a non-insignificant amount of optimisation was required to fit everything within that space. This was primarily due to the additional overhead of the SVD functions used in the Eigen library for Least Squares model fitting.

The power efficiency granted from the low-power L4 variant of the STM32 microcontroller was beneficial in the context of designing for a resource limited spacecraft; however, despite not being explicitly tested, the MCU’s execution speed for an image capture, processing, and attitude estimation was approximately 1-3 seconds. Although the ADCS of a real craft can use accurate timestamping of when the sensors attitude estimation took place to partially correct for this processing time, a faster MCU with a larger allocation of memory is recommended in a future revision; *e.g.* the STM32 H7 family of MCU’s, with 1,000KB+ of memory.

5.2 Launch / Space Environment Testing

Another aspect worth further study in a future revision of the prototype is its response characteristics when exposed to other environmental factors typical of a space bound craft. This includes vibration testing to assess its ability to withstand the chaotic launch environment, as well as vacuum chamber and thermal cycle testing, analogous to what is encountered by a craft in orbit.

Thermal cycling the prototype while it is under vacuum also allows a better assessment of the thermal management design of the prototype PCB, discussed in 2.2.1.4. Additionally, vacuum chamber testing is useful to assess the material properties used on the prototype, particularly regarding their outgassing / sublimation behaviour. This is particularly important for any sensors that perceive the environment from behind a lens, or transparent surface (as is the case with the pinhole thermal sensor). This outgassing has the potential to inhibit the sensors performance by tarnishing the transparent surface it views the world through. Similarly, if the pinhole sensor body is sealed, it may require modification with a venting hole to allow proper equalisation to vacuum.

To better withstand the chaotic launch environment, it is recommended that the microcontrollers package type also be changed from the current QFN (Quad Flat No-Lead) to QFP (Quad Flat Package) variant in a future revision; see Fig. 66. While the QFN package allows for a smaller footprint, the external legs of the QFP version are better suited for use on space bound crafts. This is due to the packages external-legs improved thermal dissipation to the PCB, and better relative flexibility (reducing the chance of cracked solder joints from vibration during launch / thermal cycling *etc.*).

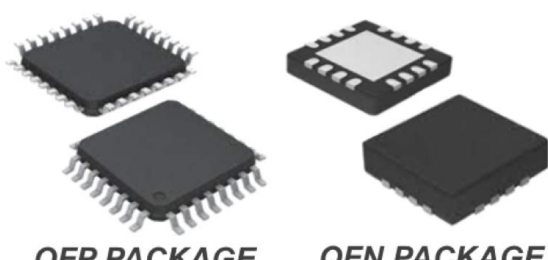


Fig. 66 Example illustration of QFP vs QFN package formfactor. Adapted from [45]

5.3 Alternate Conic View Test Stand

As discussed in the simulated orbital view test stand results in section 3.2.1, the use of a flat plane to represent the horizons conic edge does not allow for an accurate representation of the change to the shape of the projected conic as the sensor is pitched towards or away from the nadir vector.

An alternative design for the test stand was initially investigated which would better represent the circular visible horizons conic projection to the sensors 2D image plane; an original draft model illustrating the design is shown in Fig. 67.

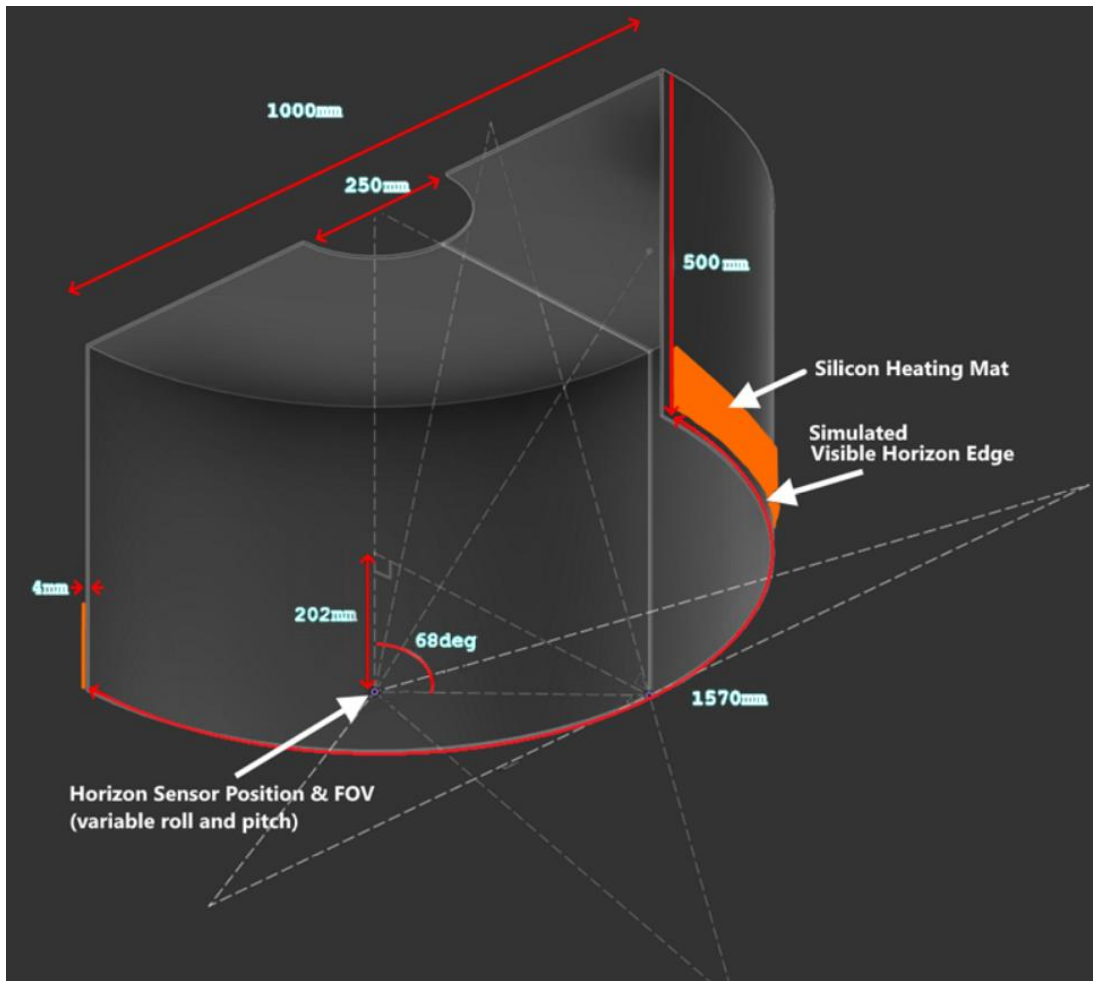


Fig. 67 Alternative idea for simulated infrared orbital view test stand, to more accurately represent the projected horizon conic in the sensors image frame during pitch movements; scaled to model a 600km LEO orbit altitude

The alternate test stand design uses a metal half cylinder to represent the circular visible horizon. The half cylinder is fixed concentrically above the pitch-roll-gimbal-mounted horizon sensor while it views the inside edge of the cylinder. The size of the cylinder, and the horizon sensor's location relative to it, are based on the scaled configuration of the view from a chosen orbit altitude. Silicon thermal heating straps are placed behind the bottom edge of the cylinder to create a uniform temperature differential across the lower internal face of the cylinder. Similar to the test stands design in this paper, the top positioning of the cylinder is intended to avoid heat rising into the sensors image frame due to convection, and create a distinct thermal edge for the sensor to perceive.

The concept of this design is to present the horizon edge to the sensor in a way that is more analogous to how the conic projection would be seen by the craft from orbit.

Although this design wasn't pursued due to perceived challenges creating a sub-zero space background proxy that spanned the entire test stand scene, the results in 3.2.1 suggest that this level of cooling may not be required; and as long as the background in view of the sensor behind the cylinder is uniform in temperature and distinct enough from the lower heated edge of the cylinder, the edge detection of the sensor could be evaluated with a wider range of detector FOVs, and additional allowance for pitch rotations during testing (by more accurately representing the associated projected conic shape change this movement creates).

5.4 Skip Conic Fitting

As a brief introduction, another approach investigated for attitude determination is the Christian-Robinson algorithm [20] demonstrated by Inman et al. [46]. This involves representing the Earth as a unit sphere and using projective geometries to skip the conic section fitting by working directly in the vector transform space; *i.e.* a direct projective transform.

In the sensors image frame, the conic horizon edge in the image represents the points on the celestial body's surface that are tangent to the line of sight of the camera. Given the camera is at the apex of the conic representing these rays, the linear distance from the sensor to the circular visible horizon edge is consistent regardless of direction.

Therefore, with knowledge of the planet's radius and the craft's current altitude, the approximate linear distance from the sensor to the visible horizon can be calculated; relating to Fig. 10, L_{sight} is estimated using Eq. (19).

$$L_{sight} = \sqrt{(R_E + h)^2 - R_E^2} \quad (19)$$

Using these distances, a transform is found such that the projected points making a conic in the 2D image plane are mapped to 3D points that represent the circular visible horizon on the surface of a unit sphere; as illustrated in Fig. 68.

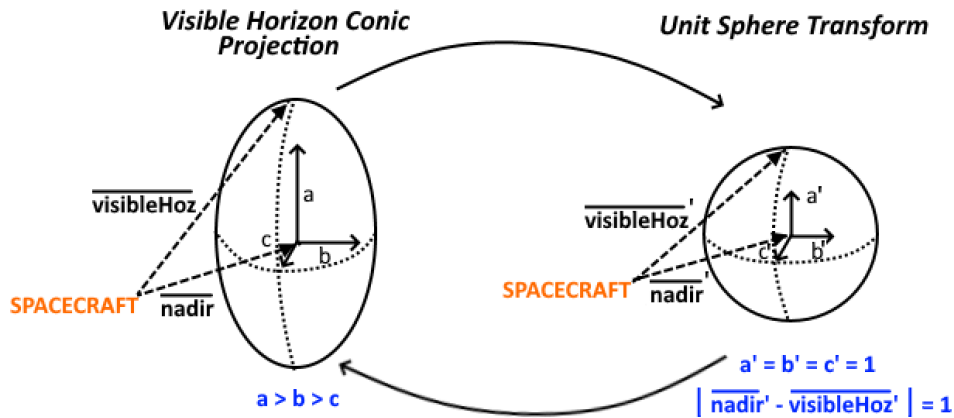


Fig. 68 Illustration of Christian-Robinson projection transform to unit sphere vector space

This transform allows the problem to be reframed in terms of a circular visible horizon edge on a unit sphere representation of the planet. Utilised this representation, the least squares method is used to find a solution which aligns the cameras line of sight vector with the centre of the planetary unit sphere, *i.e.* the nadir vector. By inverting the initial unit sphere transform, the solution found for the orientation of the nadir vector relative to the cameras actual line of sight can be identified.

This approach has been demonstrated for orbital navigation using visible band cameras by [46] on the Artemis I flight with promising results, and is a recommended point of future investigation to assess its utility in improving the attitude determination performance of infrared horizon sensors too; by simplifying the number of required calculations typical of an approach using the conic fitting method.

6. References

- [1] Virginia Space Grant Consortium, “Virginia CubeSat Constellation.” VSGC. Accessed: Apr. 10, 2024. [Online.] Available: <https://vsgc.odu.edu/virginiacubesatconstellation/#primaryimage>
- [2] *CubeSat Design Specification*, CP-CDS-R14.1, Cal Poly CubeSat Program, USA, Feb. 2022. [Online.] Available: https://static1.squarespace.com/static/5418c831e4b0fa4ecac1bacd/t/62193b7fc9e72e0053f00910/1645820809779/CDS+REV14_1+2022-02-09.pdf
- [3] C. Huston, “Orion Stage Adapter Readied for Ride on Artemis I.” NASA. Accessed: Apr. 10, 2024. [Online.] Available: <https://www.nasa.gov/image-article/orion-stage-adapter-readied-ride-artemis-i/>
- [4] National Aeronautics & Space Administration. “NASA State of the Art 2022: Guidance, Navigation & Control,” NASA, USA, 5.-SOA-GNC-2022, 2022. [Online.] Available: <https://www.nasa.gov/wp-content/uploads/2023/05/5.-soa-gnc-2022.pdf>
- [5] P. Fortescue et al., *Spacecraft Systems Engineering*, 4th ed. USA: Wiley, 2011. [Online.] doi: [10.1002/9781119971009](https://doi.org/10.1002/9781119971009)
- [6] Wikimedia Commons, “EM Spectrum Properties.” Wikipedia. Accessed: Sep. 29, 2024. [Online.] Available: https://commons.wikimedia.org/wiki/File:EM_Spectrum_Properties_edit.svg
- [7] J. W. Burn, “The Application of the Spectral and Spatial Characteristics of the Earth's Infrared Horizon to Horizon Scanners,” *IEEE Transactions on Aerospace.*, vol. 1, no. 2, pp. 1115-1126, Aug. 1963, doi: [10.1109/TA.1963.4319485](https://doi.org/10.1109/TA.1963.4319485)
- [8] National Oceanic & Atmospheric Administration, National Centres for Environmental Information, “Monthly Global Climate Report for Annual 2023,” NOAA, USA, Jan. 2024. [Online.] Available: <https://www.ncei.noaa.gov/access/monitoring/monthly-report/global/202313>
- [9] N. Kuring, “Blue Marble: The View from the Top.” NASA. Accessed: May. 5, 2024. [Online.] Available: <https://visibleearth.nasa.gov/images/78349/the-view-from-the-top>

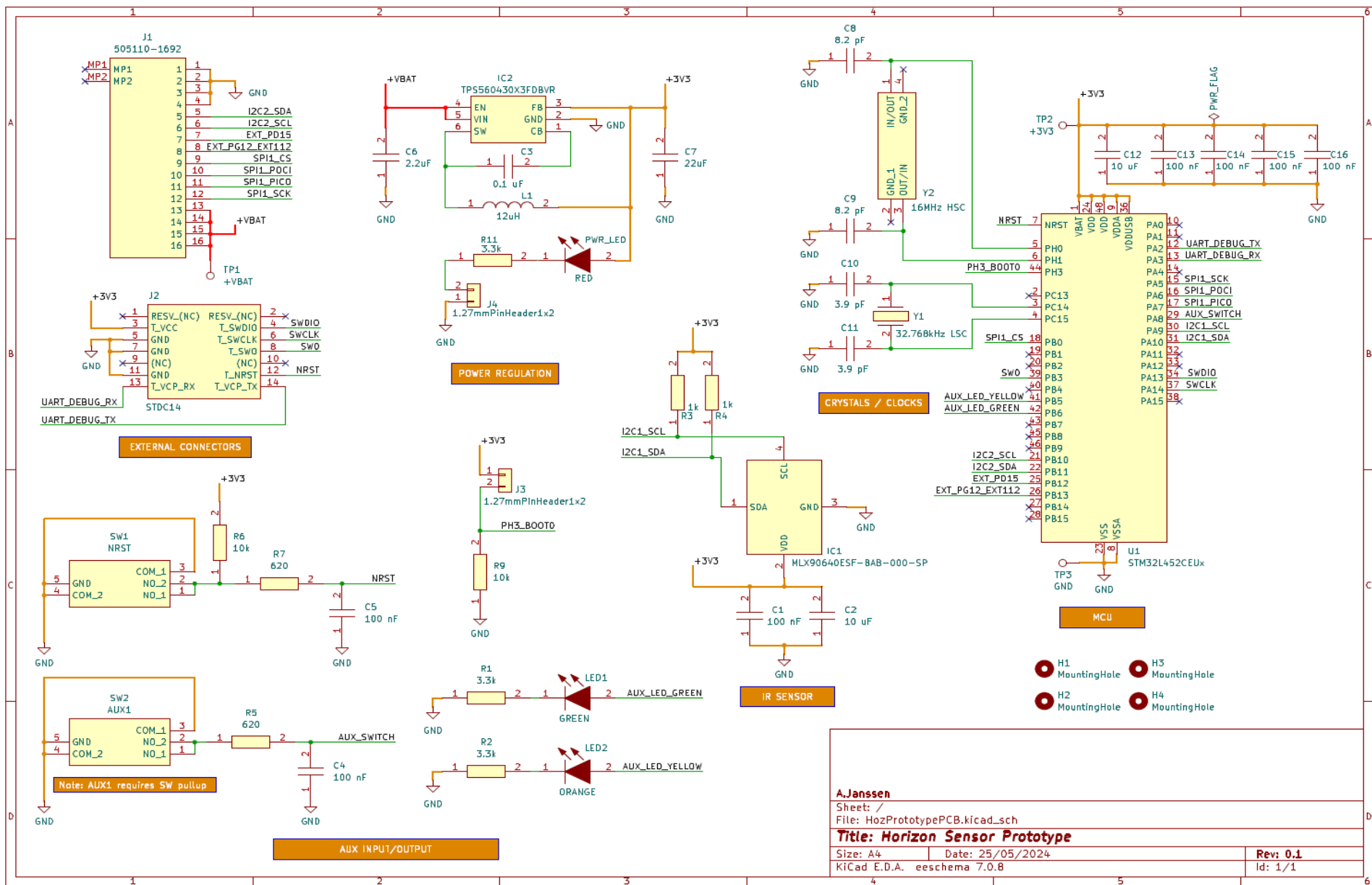
- [10] Wikimedia Commons, “Solar spectrum en.” Wikipedia. Accessed: May. 15, 2024. [Online.] Available: https://en.m.wikipedia.org/wiki/File:Solar_spectrum_en.svg
- [11] A. Rogalski, “Infrared detectors: an overview,” *Infrared Physics & Technology.*, vol. 43, no. 3-5, pp. 187-210, Jun. 2002, doi: [10.1016/S1350-4495\(02\)00140-8](https://doi.org/10.1016/S1350-4495(02)00140-8)
- [12] I. Vertat et al., “Earth's thermal radiation sensors for attitude determination systems of small satellites,” *Contributions of the Astronomical Observatory.*, vol. 47, no. 2, pp. 157-164, Jan. 2017, doi: https://www.researchgate.net/publication/320432692_Earth's_thermal_radiation_sensors_for_attitude_determination_systems_of_small_satellites
- [13] National Aeronautics & Space Administration, “NASA Space Vehicle Design Criteria: Spacecraft Earth Horizon Sensors,” NASA., USA, NASA-SP-8033, Dec. 1969. [Online.] Available: <https://ntrs.nasa.gov/api/citations/19700026254/downloads/19700026254.pdf>
- [14] R. W. Astheimer, “Infrared Horizon Sensors for Attitude Determination,” *IFAC Proceedings Volumes.*, vol. 2, no. 1, pp. 381-396, Jun. 1965, doi: [10.1016/S1474-6670\(17\)69110-9](https://doi.org/10.1016/S1474-6670(17)69110-9)
- [15] A. García Sáez et al., “Earth Sensor Based on Thermopile Detectors for Satellite Attitude Determination,” *IEEE Sensors Journal.*, vol. 16, no. 8, pp. 2260-2271, Apr. 2016, doi: [10.1109/JSEN.2015.2511070](https://doi.org/10.1109/JSEN.2015.2511070)
- [16] T. Nguyen et al., “Attitude Determination for Small Satellites with Infrared Earth Horizon Sensors,” *Journal of Spacecraft and Rockets.*, vol. 55, no. 6, pp. 1466-1475, Aug. 2018, doi: [10.2514/1.A34010](https://doi.org/10.2514/1.A34010)
- [17] A. W. Herwaarden, “Low-cost satellite attitude control sensors based on integrated infrared detector arrays,” *IEEE Transactions on Instrumentation and Measurement.*, vol. 50, no. 6, pp. 1524-1529, Dec. 2001, doi: [10.1109/19.982939](https://doi.org/10.1109/19.982939)
- [18] H. M. Van Rensburg, “An infrared earth horizon sensor for a LEO satellite,” M.S. thesis, Dept. Physics and Eng., Univ. of Stellenbosch, Western Cape, South Africa, Mar. 2008. [Online.] Available: <https://api.semanticscholar.org/CorpusID:127396234>

- [19] J. H. Wessels, “Infrared horizon sensor for CubeSat implementation,” M.S. thesis, Dept. Physics and Eng., Univ. of Stellenbosch, Western Cape, South Africa, Mar. 2018. [Online.] Available: <https://api.semanticscholar.org/CorpusID:125611527>
- [20] J. A. Christian, “A Tutorial on Horizon-Based Optical Navigation and Attitude Determination with Space Imaging Systems,” *IEEE Access.*, vol. 9, pp. 19819–19853, Jan. 2021, doi: [10.1109/ACCESS.2021.3051914](https://doi.org/10.1109/ACCESS.2021.3051914)
- [21] B. Braun and J. Barf, “Image processing-based horizon sensor for estimating the orientation of sounding rockets, launch vehicles and spacecraft,” *CEAS Space Journal.*, vol. 15, pp. 509–533, May. 2023, doi: [10.1007/s12567-022-00461-0](https://doi.org/10.1007/s12567-022-00461-0)
- [22] F. Zernike, “Diffraction theory of the knife-edge test and its improved form, the phase-contrast method,” *Monthly Notices of the Royal Astronomical Society.*, vol. 94, pp. 377–384, 1934, doi: [1934MNRAS.94..377Z7](https://doi.org/10.1093/mnras/94..377z7)
- [23] Wikimedia Commons, “Zernike polynomials with read-blue cmap.” Wikipedia. Accessed: Oct. 10, 2024. [Online.] Available: https://commons.wikimedia.org/wiki/File:Zernike_polynomials_with_read-blue_cmap.png
- [24] J. A. Christian, “Accurate Planetary Limb Localization for Image-Based Spacecraft Navigation,” *Journal of Spacecraft and Rockets.*, vol. 54, no. 3, pp. 708–730, Apr. 2017, doi: [10.2514/1.A33692](https://doi.org/10.2514/1.A33692)
- [25] M. Edwards, “Pinhole Theory Explained,” Martin Edwards Photography. Accessed: Apr. 22, 2024. [Online.] Available: http://www.martinedwardsphotography.co.uk/pinhole_cameras_explained.pdf
- [26] Wikimedia Commons, “Pinhole.” Wikipedia. Accessed: Oct. 1, 2024. [Online.] Available: <https://commons.wikimedia.org/wiki/File:Pinhole.svg>
- [27] K. Simek, “Dissecting the Camera Matrix.” ksimek. Accessed: Aug. 30, 2024. [Online.] Available: <https://ksimek.github.io/2013/08/13/intrinsic/>
- [28] A.H. Robinson and The Committee on Map Projections, “Choosing a World Map”, in *Choosing a Map Projection*, M. Lapaine and E.L. Usery, Eds., USA: Springer, 2017, pp. 15–48.
- [29] M. H. Protter and C. B. Morrey, “Chapter 10. The Conics”, in *College calculus with analytic geometry*, 2nd ed. USA: Addison-Wesley, 1970, pp. 286–330.

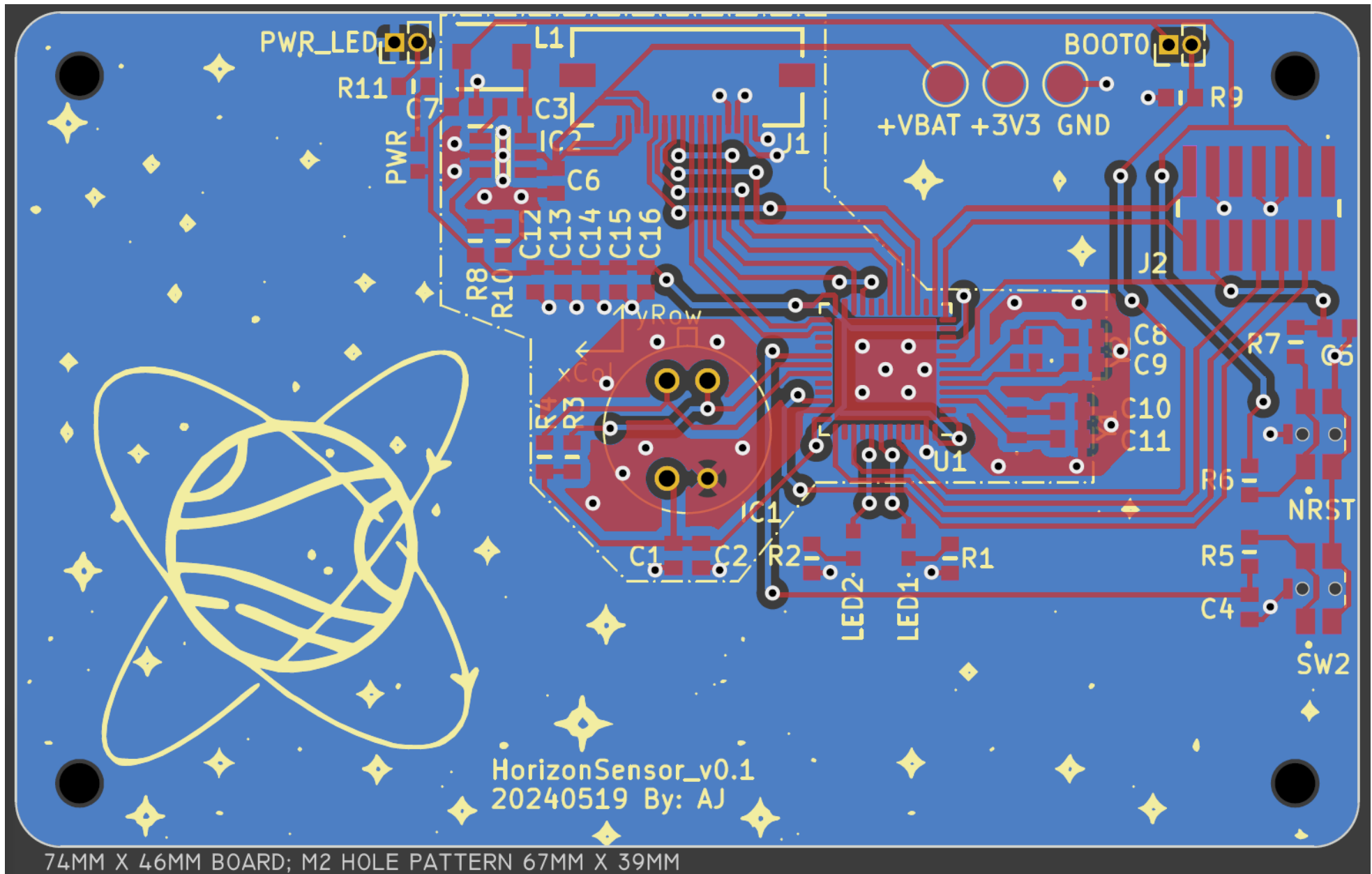
- [30] Melexis, “Datasheet for MLX90640,” Melexis. Accessed: Mar. 12, 2024. [Online.] Available: <https://www.melexis.com/en/documents/documentation/datasheets/datasheet-mlx90640>
- [31] M. Harris, “Why does the Clock Source Matter.” Altium. Accessed: Oct. 13, 2024. [Online.] Available: <https://resources.altium.com/p/how-important-your-microcontroller-clock-source>
- [32] BinarX-Curtin, “BinarX-Rocket-Payload-Microcontroller-Board,” GitHub. Accessed: Apr. 10, 2024. [Online.] Available: <https://github.com/BinarX-Curtin/BinarX-Rocket-Payload-Microcontroller-Board>
- [33] BinarX-Curtin, “Payload-Development-Kit,” GitHub. Accessed: Apr. 10, 2024. [Online.] Available: <https://github.com/BinarX-Curtin/Payload-Development-Kit>
- [34] Eigen, “C++ template library for linear algebra: matrices, vectors, numerical solvers, and related algorithms,” GitLab. Accessed: Apr. 15, 2024. [Online.] Available: <https://gitlab.com/libeigen/eigen>
- [35] A. Janssen, “mtxCV,” GitHub. Accessed: Apr. 28, 2024. [Online.] Available: <https://github.com/gotenham/mtxCV>
- [36] Wikimedia Commons, “Canny edge detector,” Wikipedia. Accessed: Jul. 22, 2024. [Online.] Available: https://en.wikipedia.org/wiki/Canny_edge_detector
- [37] Wikimedia Commons, “Breadth-First Search,” Wikipedia. Accessed: Jul. 22, 2024. [Online.] Available: https://en.wikipedia.org/wiki/Breadth-first_search
- [38] Wikimedia Commons, “Random Sample Consensus,” Wikipedia. Accessed: Jul. 22, 2024. [Online.] Available: https://en.wikipedia.org/wiki/Random_sample_consensus
- [39] European Space Agency, “Planck and the cosmic microwave background.” ESA. Accessed: Aug. 8, 2024. [Online.] Available: https://www.esa.int/Science_Exploration/Space_Science/Planck/Planck_and_the_cosmic_microwave_background
- [40] The Engineering Toolbox, “Nitrogen - Thermophysical Properties.” engineeringtoolbox. Accessed: Aug. 8, 2024. [Online.] Available: https://www.engineeringtoolbox.com/nitrogen-d_1421.html

- [41] Robotis, “Datasheet for AX-12A,” Robotis. Accessed: Apr. 8, 2024. [Online.] Available: <https://emanual.robotis.com/docs/en/dxl/ax/ax-12a>
- [42] A. D’Amico et al., “Volatile Compounds Detection by IR Acousto-Optic Detectors”, in *Unexploded Ordnance Detection and Mitigation.*, J. Byrnes Ed, Tuscany, Italy, Jul. 2008, pp. 21-32.
- [43] A.M. Barradas, “Development of a non-invasive temperature monitoring and tracking device using machine learning algorithms,” M.S. thesis, Fac. Sciences and Eng., Univ. of Coimbra, Coimbra, Portugal, Sep. 2022. [Online.] Available: <https://estudogeral.uc.pt/handle/10316/106004>
- [44] A. Janssen, “Infrared Horizon Sensor,” GitHub. Accessed: Oct. 26, 2024. [Online.] Available: <https://github.com/gotenham/infraredHorizonSensor>
- [45] AVAQ Semiconductor Co., “Differences between QFP and QFN Packages.” Avaq. Accessed: Oct. 25, 2024. [Online.] Available: <https://www.avaq.com/technology/what-is-qfp-package-features-types-and-applications-2023>
- [46] R. Inman et al., “Artemis I Optical Navigation System Performance,” in *American Institute of Aeronautics and Astronautics SCITECH 2024 Forum.*, Florida, Jan. 2024, doi: [10.2514/6.2024-0514](https://doi.org/10.2514/6.2024-0514)

APPENDIX A – Horizon Sensor Schematic



APPENDIX B – Horizon Sensor PCB Layout



APPENDIX C – PCB Trace Electrical Calculations

Power net 0.4mm trace (~1A @10°C rise) left; signal lines 0.25mm trace (~0.35A @2°C rise) right:

The image displays two identical software interfaces for the Saturn PCB Toolkit V8.21. Both screens show the 'Conductor Characteristics' calculator.

Left Screen (Power Net Calculation):

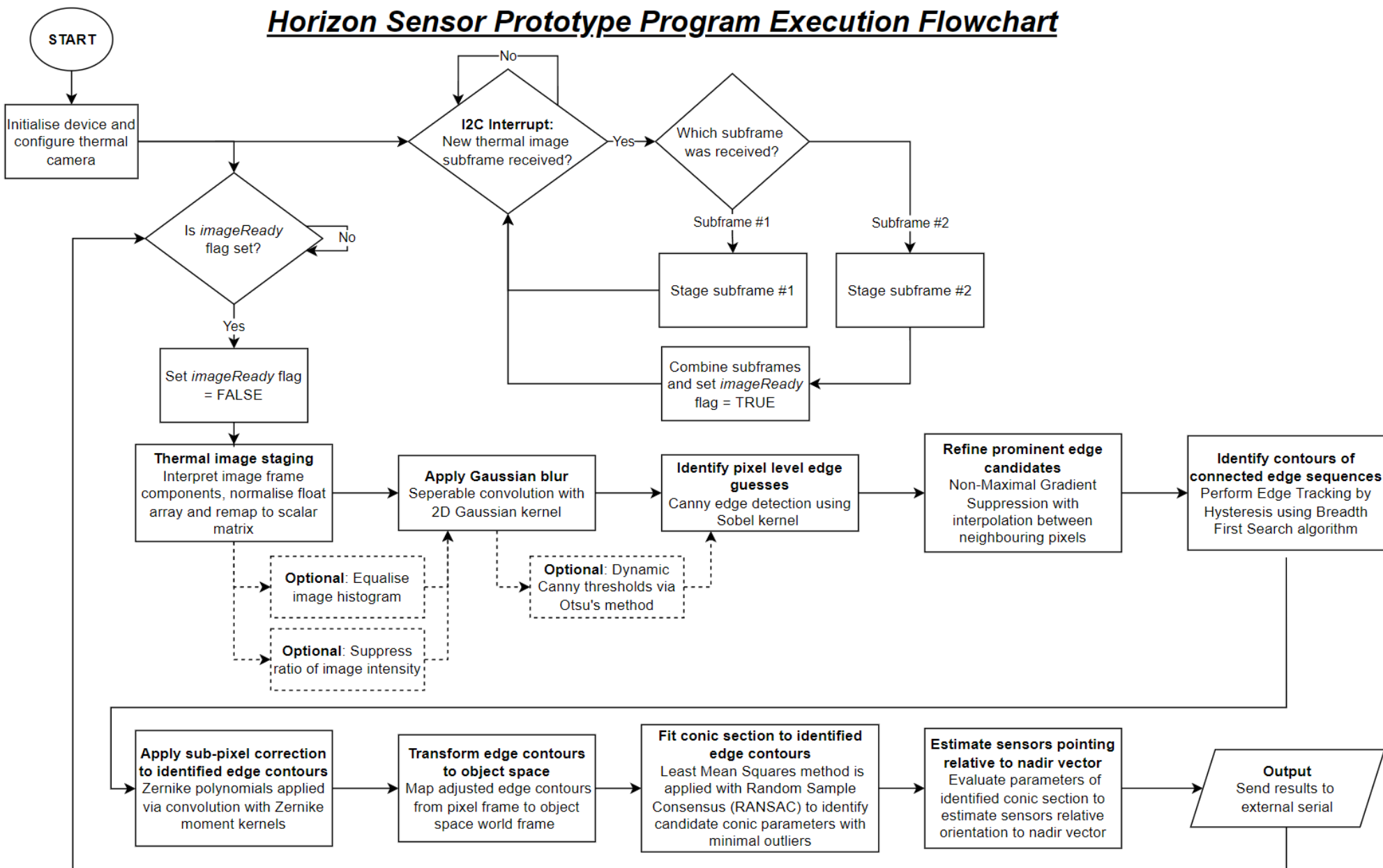
- Solve For:** Amperage (radio button selected).
- Conductor Width:** 0.4 mm.
- Conductor Length:** 50 mm.
- PCB Thickness:** 1.5748 mm.
- Frequency:** DC (checkbox checked).
- Options:**
 - Base Copper Weight:** 35um (radio button selected).
 - Units:** Metric (radio button selected).
 - Substrate Options:** FR-4 STD (dropdown menu).
 - Plating Thickness:** 18um (radio button selected).
 - Temp Rise (°C):** 10 (input field).
 - Ambient Temp (°C):** 0 (input field).
 - Information:** Total Copper Thickness: 70 um; Via Thermal Resistance: N/A; Via Count: 10; Conductor Temperature: Temp in (°C) = 10.0, Temp in (°F) = 50.0; Via Voltage Drop: N/A.
- Results:**
 - Power Dissipation: 0.03060 Watts.
 - Conductor DC Resistance: 0.02957 Ohms.
 - Power Dissipation in dBm: 14.8569 dBm.
 - Conductor Cross Section: 0.0280 Sq.mm.
 - Voltage Drop: 0.0301 Volts.
 - Conductor Current: 1.0172 Amps.

Right Screen (Signal Line Calculation):

- Solve For:** Amperage (radio button selected).
- Conductor Width:** 0.25 mm.
- Conductor Length:** 50 mm.
- PCB Thickness:** 1.5748 mm.
- Frequency:** DC (checkbox checked).
- Options:**
 - Base Copper Weight:** 35um (radio button selected).
 - Units:** Metric (radio button selected).
 - Substrate Options:** FR-4 STD (dropdown menu).
 - Plating Thickness:** 18um (radio button selected).
 - Temp Rise (°C):** 2 (input field).
 - Ambient Temp (°C):** 0 (input field).
 - Information:** Total Copper Thickness: 70 um; Via Thermal Resistance: N/A; Via Count: 10; Conductor Temperature: Temp in (°C) = 2.0, Temp in (°F) = 35.6; Via Voltage Drop: N/A.
- Results:**
 - Power Dissipation: 0.00581 Watts.
 - Conductor DC Resistance: 0.04577 Ohms.
 - Power Dissipation in dBm: 7.6429 dBm.
 - Conductor Cross Section: 0.0175 Sq.mm.
 - Voltage Drop: 0.0163 Volts.
 - Conductor Current: 0.3563 Amps.

APPENDIX D – Software Flowchart Illustration

Horizon Sensor Prototype Program Execution Flowchart



APPENDIX E – Prototype Conic Fitting Results

The five initial conic fitting results received from the prototype horizon sensor while viewing the simulated orbital horizon test stand at various roll angles are presented below.

The success criteria are based on an LEO altitude of 600-800km, from a 55°x35° FOV sensor, at nominal orientation.

The success criteria for the identified conic models are:

- a) $1.94 \leq e \leq 2.25$

Within each table, conforming eccentricity [e] results are depicted in **green**, and outliers are depicted in **red**.

-40° Roll Conic Fitting Result

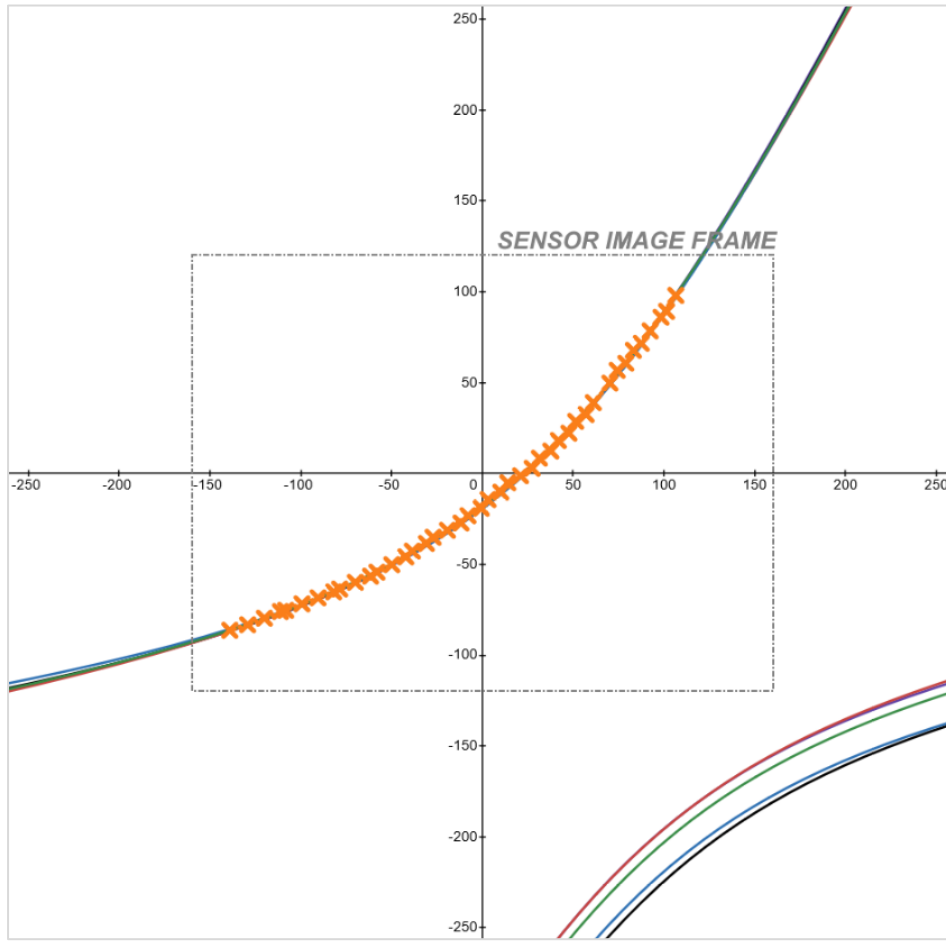


Fig. 69 Conic models fit to imaged horizon edge by the prototype sensor at -40° z-axis roll. Orange marks represent edge coordinates, lines depict fit conic models

TABLE 18 Initial 5 conic models fit to imaged horizon edge by RANSAC on prototype sensor while at -40° z-axis roll; model colours in first column align to graph above

Model Inliers	A x^2	B xy	C y^2	D x	E y	F	Eccentricity [e]
[39 of 43]	0.000050	-0.000376	0.000166	-0.043916	0.055238	0.997507	2.103
[41 of 42]	0.000041	-0.000355	0.000154	-0.044686	0.056413	0.997407	2.047
[40 of 43]	0.000055	-0.000392	0.000175	-0.045783	0.057923	0.997271	2.133
[38 of 43]	0.000037	-0.000346	0.000152	-0.042831	0.054568	0.997591	2.036
[39 of 42]	0.000051	-0.000388	0.000172	-0.046173	0.058374	0.997226	2.103

-30° Roll Conic Fitting Result

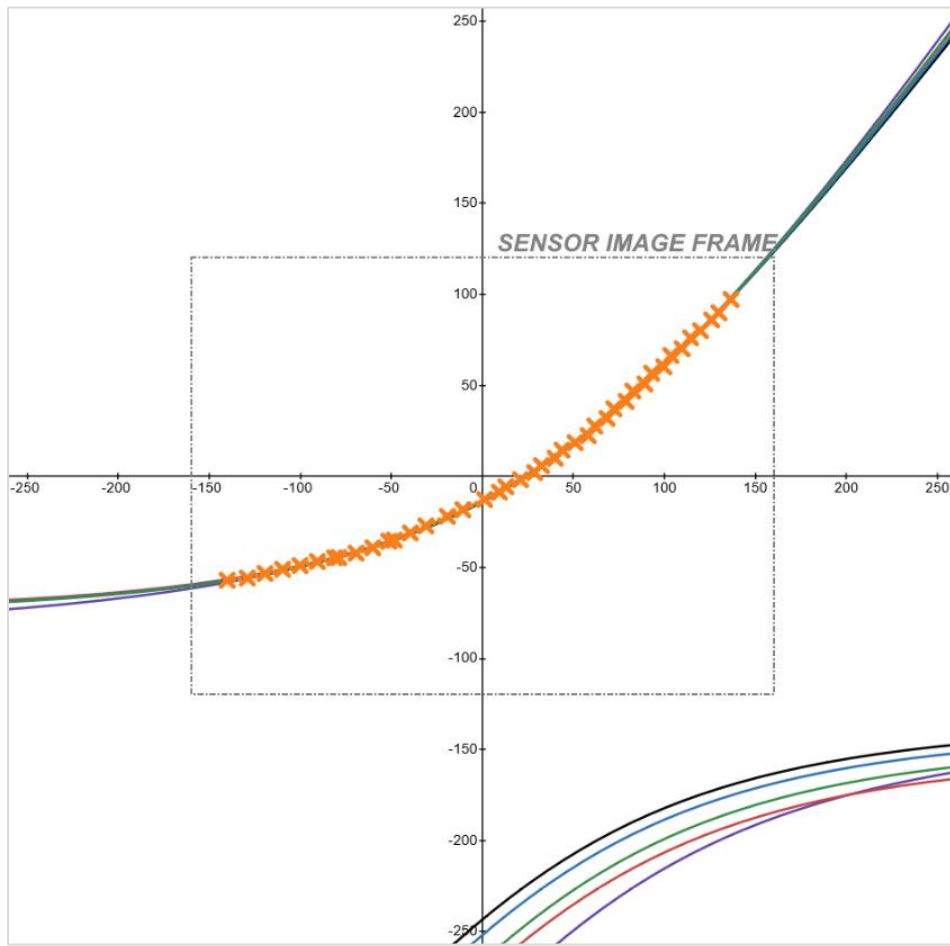


Fig. 70 Conic models fit to imaged horizon edge by the prototype sensor at -30° z-axis roll. Orange marks represent edge coordinates, lines depict fit conic models

TABLE 19 Initial 5 conic models fit to imaged horizon edge by RANSAC on prototype sensor while at -30° z-axis roll; model colours in first column align to graph above

Model Inliers	A x^2	B xy	C y^2	D x	E y	F	Eccentricity [e]
[38 of 42]	-0.000005	-0.000395	0.000258	-0.043231	0.079361	0.995908	2.069
[38 of 42]	-0.000012	-0.000407	0.000300	-0.042020	0.077078	0.996139	2.138
[37 of 41]	-0.000017	-0.000384	0.000270	-0.042102	0.077762	0.996082	2.059
[36 of 42]	-0.000013	-0.000396	0.000287	-0.041566	0.076230	0.996224	2.112
[35 of 41]	-0.000014	-0.000378	0.000266	-0.040735	0.074593	0.996382	2.075

-20° Roll Conic Fitting Result

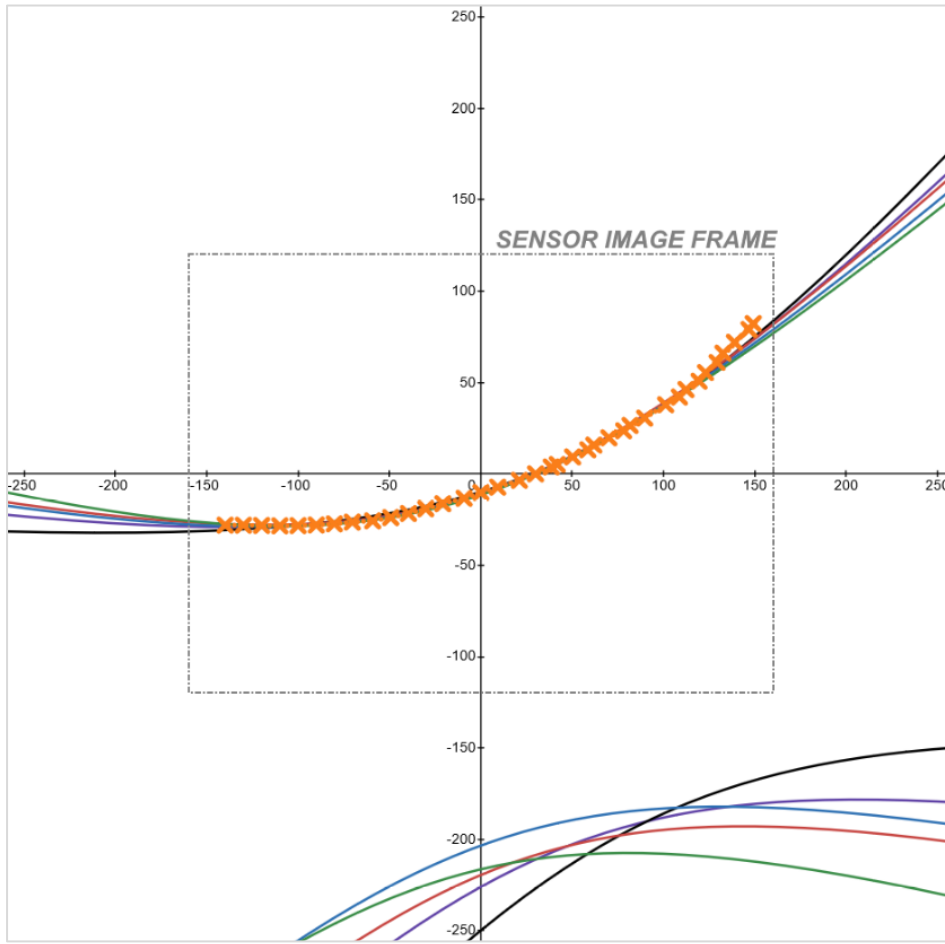


Fig. 71 Conic models fit to imaged horizon edge by the prototype sensor at -20° z-axis roll. Orange marks represent edge coordinates, lines depict fit conic models

TABLE 20 Initial 5 conic models fit to imaged horizon edge by RANSAC on prototype sensor while at -20° z-axis roll; model colours in first column align to graph above

Model Inliers	A x^2	B xy	C y^2	D x	E y	F	Eccentricity [e]
[30 of 38]	-0.000077	-0.000356	0.000410	-0.031636	0.097031	0.994778	2.111
[23 of 37]	-0.000047	-0.000456	0.000409	-0.033979	0.106113	0.993773	2.137
[31 of 38]	-0.000099	-0.000314	0.000422	-0.032068	0.097126	0.994755	2.067
[31 of 37]	-0.000093	-0.000308	0.000445	-0.031497	0.095371	0.994943	2.153
[27 of 37]	-0.000109	-0.000230	0.000403	-0.030175	0.091766	0.995323	2.051

-10° Roll Conic Fitting Result

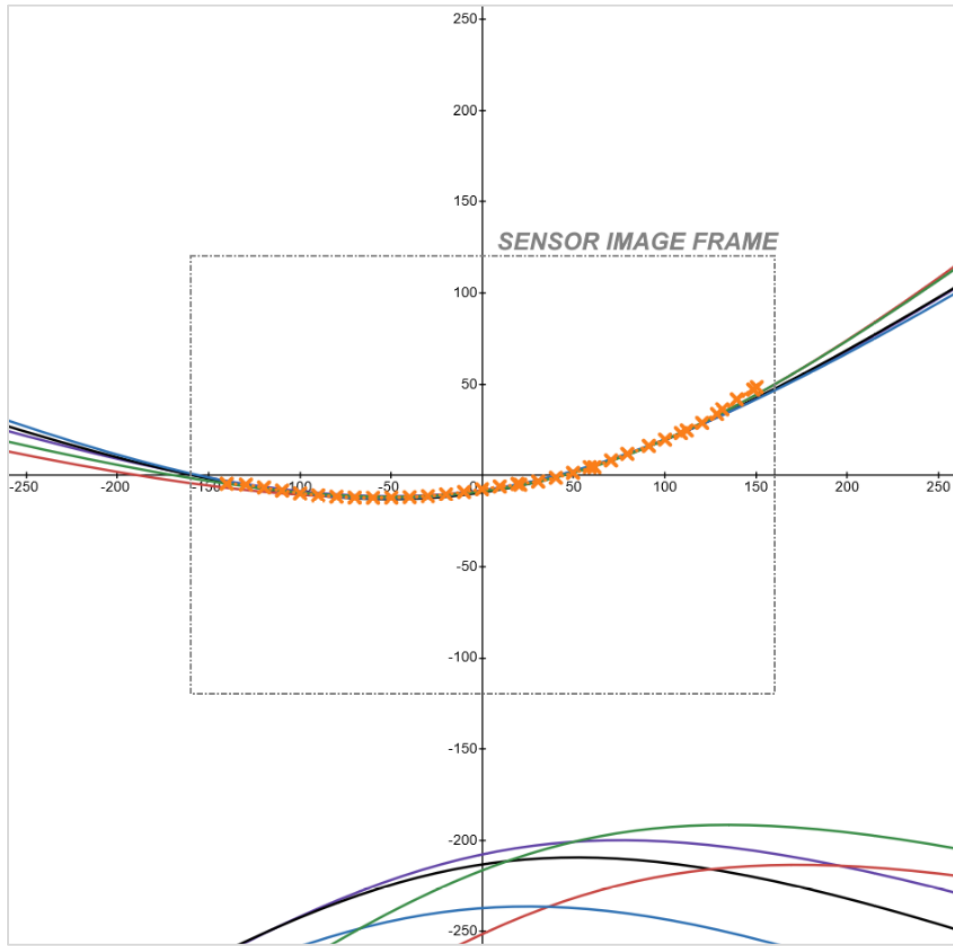


Fig. 72 Conic models fit to imaged horizon edge by the prototype sensor at -10° z-axis roll. Orange marks represent edge coordinates, lines depict fit conic models

TABLE 21 Initial 5 conic models fit to imaged horizon edge by RANSAC on prototype sensor while at -10° z-axis roll; model colours in first column align to graph above

Model Inliers	A x^2	B xy	C y^2	D x	E y	F	Eccentricity [e]
[23 of 36]	-0.000154	-0.000206	0.000595	-0.017824	0.128332	0.991571	2.148
[24 of 35]	-0.000144	-0.000150	0.000505	-0.016516	0.112305	0.993537	2.092
[25 of 35]	-0.000125	-0.000288	0.000481	-0.018205	0.124821	0.992012	2.065
[24 of 34]	-0.000158	-0.000110	0.000497	-0.018071	0.122025	0.992362	2.02
[27 of 35]	-0.000134	-0.000275	0.000532	-0.016650	0.119691	0.992671	2.115

+10° Roll Conic Fitting Result

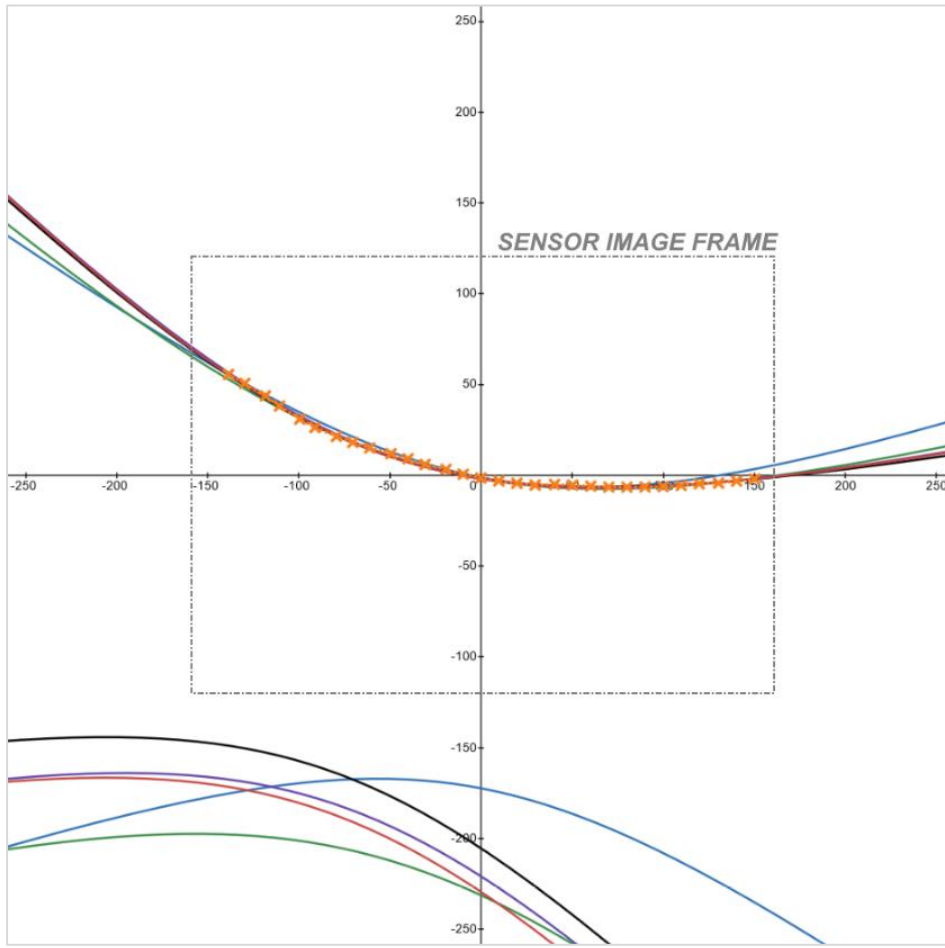


Fig. 73 Conic models fit to imaged horizon edge by the prototype sensor at +10° z-axis roll. Orange marks represent edge coordinates, lines depict fit conic models

TABLE 22 Initial 5 conic models fit to imaged horizon edge by RANSAC on prototype sensor while at +10° z-axis roll; model colours in first column align to graph above

Model Inliers	A x^2	B xy	C y^2	D x	E y	F	Eccentricity [e]
[9 of 30]	-0.001073	0.001537	0.003961	0.134353	0.686313	0.714776	2.105
[6 of 32]	-0.000554	0.001310	0.002059	0.084651	0.479676	0.873349	2.031
[12 of 31]	-0.000522	0.001741	0.002159	0.081325	0.480539	0.873190	2.024
[11 of 31]	-0.000522	0.002074	0.002536	0.083765	0.524870	0.847044	2.097
[10 of 30]	-0.000522	0.001789	0.002152	0.081856	0.497265	0.863724	2.014

+20° Roll Conic Fitting Result

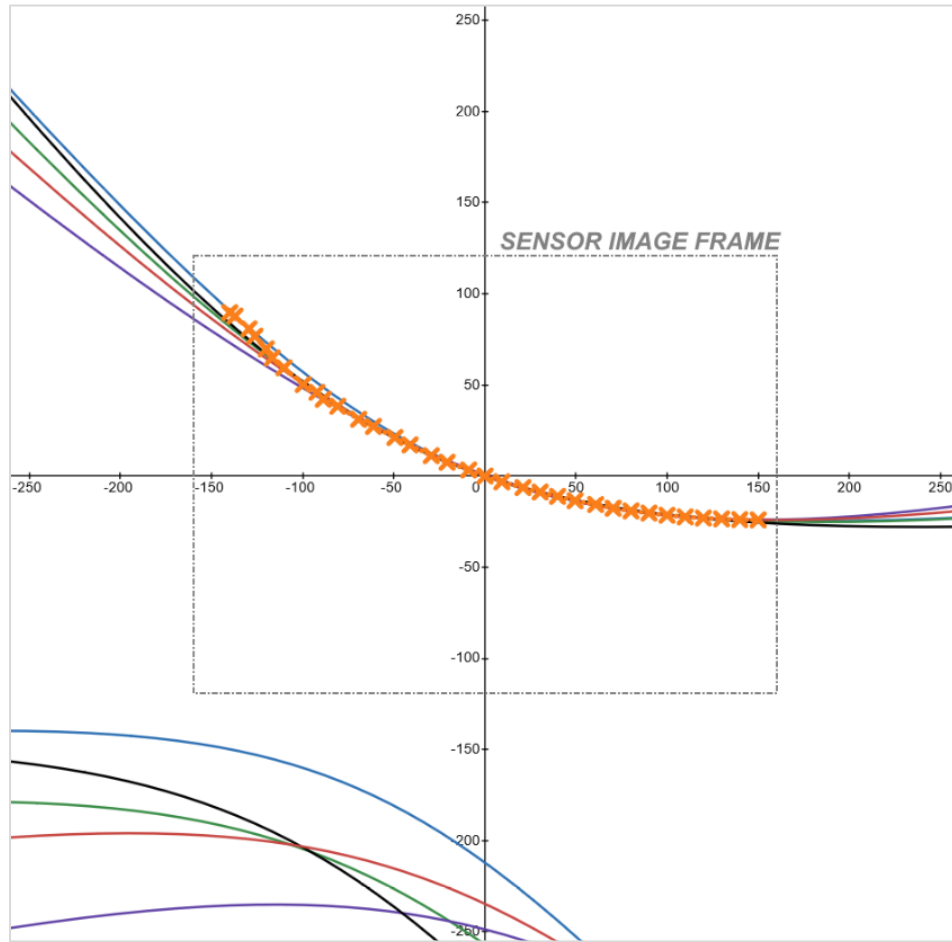


Fig. 74 Conic models fit to imaged horizon edge by the prototype sensor at +20° z-axis roll. Orange marks represent edge coordinates, lines depict fit conic models

TABLE 23 Initial 5 conic models fit to imaged horizon edge by RANSAC on prototype sensor while at +20° z-axis roll; model colours in first column align to graph above

Model Inliers	A x^2	B xy	C y^2	D x	E y	F	Eccentricity [e]
[9 of 34]	-0.000616	0.004837	0.004429	0.343341	0.939008	-0.018364	2.098
[12 of 34]	-0.000617	0.003816	0.003655	0.325235	0.939028	-0.111444	2.064
[5 of 35]	-0.000742	0.001877	0.003073	0.269735	0.761745	-0.589045	2.104
[12 of 34]	-0.000410	0.004291	0.003387	0.316323	0.942756	-0.105451	2.041
[11 of 34]	-0.000796	0.003288	0.003992	0.333290	0.936185	-0.111568	2.109

+30° Roll Conic Fitting Result

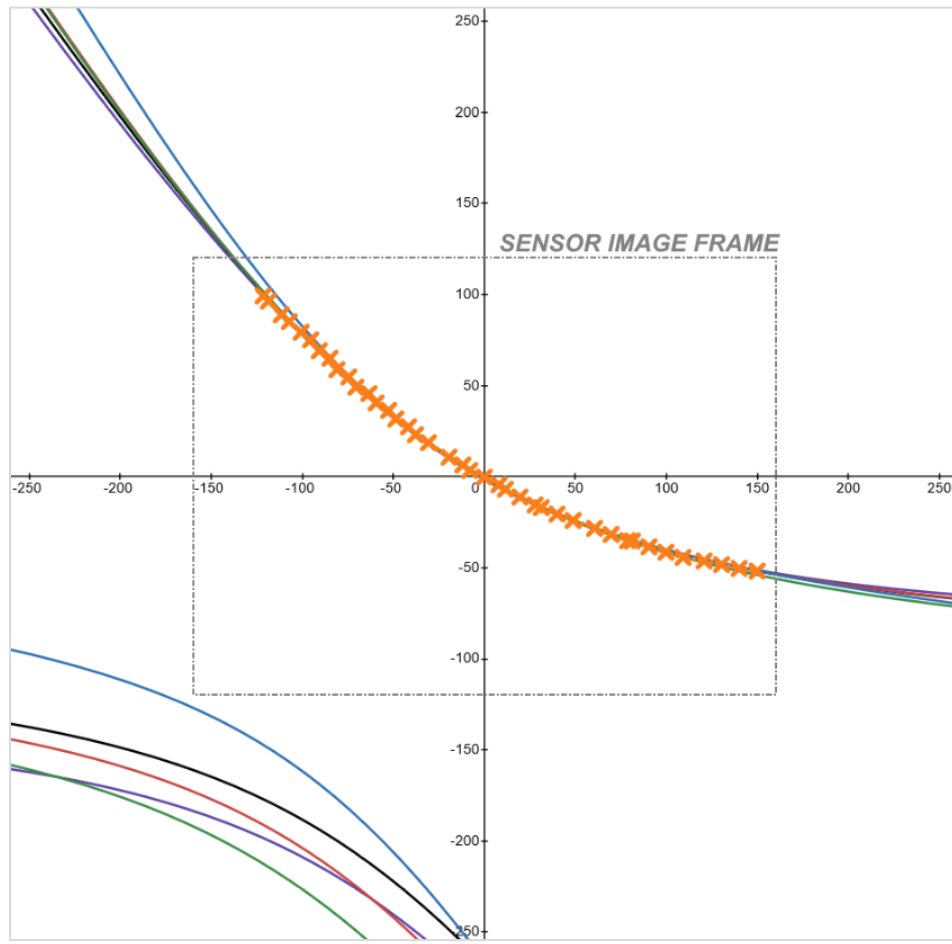


Fig. 75 Conic models fit to imaged horizon edge by the prototype sensor at +30° z-axis roll. Orange marks represent edge coordinates, lines depict fit conic models

TABLE 24 Initial 5 conic models fit to imaged horizon edge by RANSAC on prototype sensor while at +30° z-axis roll; model colours in first column align to graph above

Model Inliers	A x^2	B xy	C y^2	D x	E y	F	Eccentricity [e]
[11 of 41]	-0.000084	0.003837	0.002515	0.405048	0.713480	0.571718	2.051
[10 of 39]	0.000049	0.003902	0.002456	0.373934	0.659979	0.651598	2.1
[8 of 41]	0.000028	0.003056	0.001819	0.299934	0.534462	0.790175	2.044
[9 of 41]	0.000257	0.003843	0.002043	0.306061	0.545968	0.779889	2.091
[9 of 40]	0.000074	0.004168	0.002419	0.442046	0.774898	0.451781	2.044

+40° Roll Conic Fitting Result

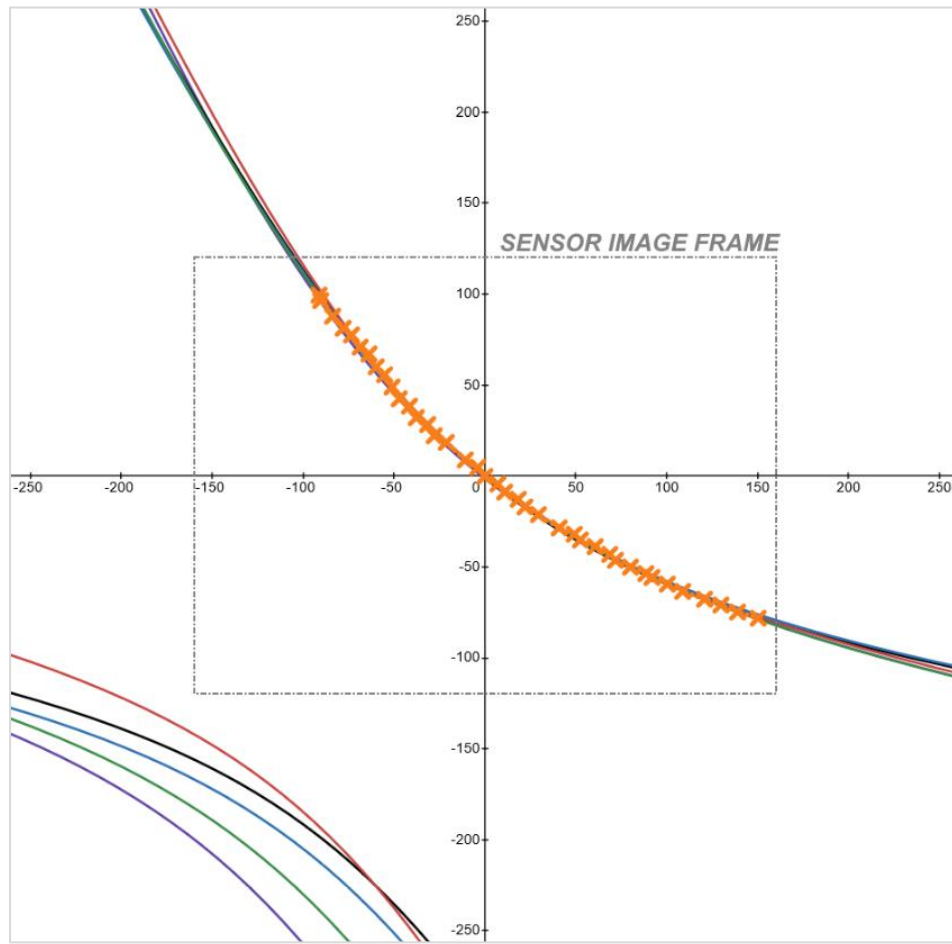


Fig. 76 Conic models fit to imaged horizon edge by the prototype sensor at +40° z-axis roll. Orange marks represent edge coordinates, lines depict fit conic models

TABLE 25 Initial 5 conic models fit to imaged horizon edge by RANSAC on prototype sensor while at +40° z-axis roll; model colours in first column align to graph above

Model Inliers	A x^2	B xy	C y^2	D x	E y	F	Eccentricity [e]
[12 of 39]	0.000468	0.003425	0.001298	0.420068	0.534405	0.733445	2.002
[5 of 40]	0.000574	0.005113	0.002347	0.571050	0.694773	0.437218	2.085
[8 of 39]	0.000898	0.006020	0.002507	0.627849	0.774096	0.080861	2.1
[8 of 40]	0.000551	0.005026	0.002280	0.576093	0.713776	-0.398260	2.069
[9 of 39]	0.000688	0.005165	0.002159	0.620100	0.772699	-0.135577	2.063

APPENDIX F – Prototype Attitude Estimation Results

Table 26 shows the five initial attitude estimation results received from the prototype horizon sensor while viewing the simulated orbital horizon test stand at various roll angles. The success criteria are based on an LEO altitude of 600-800km, from a $55^\circ \times 35^\circ$ FOV sensor, at nominal orientation.

The success criteria are listed below; within the table, conforming results are depicted in green, and outliers are depicted in red:

- a) $conicRotation = \begin{cases} \{|R(z)_{actual}| - 90^\circ\} \pm 5^\circ; & \text{if } R(z)_{actual} < 0^\circ \\ \{\pm 90^\circ\} \mp 5^\circ; & \text{if } R(z)_{actual} = 0^\circ \\ \{90^\circ - R(z)_{actual}\} \pm 5^\circ; & \text{if } R(z)_{actual} > 0^\circ \end{cases}$
- b) $21^\circ \leq \alpha \leq 31^\circ$
- c) $R(z) = (-R(z)_{actual}) \pm 5^\circ$
- d) $59^\circ \leq R(x) \leq 69^\circ$

TABLE 26 Prototype Horizon Sensor Attitude Estimation Results

Actual Craft Roll [$R(z)_{actual}$] (w.r.t sensor frame)	Figure Ref.	RANSAC Best Fit Conic Model Eq. $[Ax^2 + Bxy + Cy^2 + Dx + Ey + F = 0]$	Conic Rotation (from x-axis)	Cutting Plane Angle [α]	Rotations to align Sensor Bore to Nadir Vector (w.r.t sensor frame)
-40°	Fig. 48	$0.000050x^2 - 0.000376xy + 0.000166y^2 - 0.043916x + 0.055238y + 0.997507 = 0$	-53.56°	24.24°	R(z): 36.44°, then R(x): 65.765°
-40°	Fig. 48	$0.000041x^2 - 0.000355xy + 0.000154y^2 - 0.044686x + 0.056413y + 0.997407 = 0$	-53.81°	27.44°	R(z): 36.188°, then R(x): 62.563°
-40°	Fig. 48	$0.000055x^2 - 0.000392xy + 0.000175y^2 - 0.045783x + 0.057923y + 0.997271 = 0$	-53.49°	22.32°	R(z): 36.508°, then R(x): 67.681°
-40°	Fig. 48	$0.000037x^2 - 0.000346xy + 0.000152y^2 - 0.042831x + 0.054568y + 0.997591 = 0$	-54.22°	28°	R(z): 35.783°, then R(x): 61.997°
-40°	Fig. 48	$0.000051x^2 - 0.000388xy + 0.000172y^2 - 0.046173x + 0.058374y + 0.997226 = 0$	-53.69°	24.23°	R(z): 36.305°, then R(x): 65.773°
-30°	Fig. 49	$-0.000005x^2 - 0.000395xy + 0.000258y^2 - 0.043231x + 0.079361y + 0.995908 = 0$	-61.82°	26.2°	R(z): 28.183°, then R(x): 63.804°
-30°	Fig. 49	$-0.000012x^2 - 0.000407xy + 0.000300y^2 - 0.042020x + 0.077078y + 0.996139 = 0$	-63.72°	22°	R(z): 26.283°, then R(x): 68.004°
-30°	Fig. 49	$-0.000017x^2 - 0.000384xy + 0.000270y^2 - 0.042102x + 0.077762y + 0.996082 = 0$	-63.34°	26.75°	R(z): 26.663°, then R(x): 63.25°
-30°	Fig. 49	$-0.000013x^2 - 0.000396xy + 0.000287y^2 - 0.041566x + 0.076230y + 0.996224 = 0$	-63.53°	23.65°	R(z): 26.47°, then R(x): 66.345°

-30°	Fig. 49	$-0.000014x^2 - 0.000378xy + 0.000266y^2 - 0.040735x + 0.074593y + 0.996382 = 0$	-63.23°	25.87°	R(z): 26.772°, then R(x): 64.134°
-20°	Fig. 50	$-0.000077x^2 - 0.000356xy + 0.000410y^2 - 0.031636x + 0.097031y + 0.994778 = 0$	-71.92°	23.7°	R(z): 18.082°, then R(x): 66.297°
-20°	Fig. 50	$-0.000047x^2 - 0.000456xy + 0.000409y^2 - 0.033979x + 0.106113y + 0.993773 = 0$	-67.48°	22.09°	R(z): 22.522°, then R(x): 67.912°
-20°	Fig. 50	$-0.000099x^2 - 0.000314xy + 0.000422y^2 - 0.032068x + 0.097126y + 0.994755 = 0$	-74.46°	26.3°	R(z): 15.544°, then R(x): 63.701°
-20°	Fig. 50	$-0.000093x^2 - 0.000308xy + 0.000445y^2 - 0.031497x + 0.095371y + 0.994943 = 0$	-75.1°	21.01°	R(z): 14.898°, then R(x): 68.995°
-20°	Fig. 50	$-0.000109x^2 - 0.000230xy + 0.000403y^2 - 0.030175x + 0.091766y + 0.995323 = 0$	-77.88°	27.2°	R(z): 12.123°, then R(x): 62.796°
-10°	Fig. 51	$-0.000154x^2 - 0.000206xy + 0.000595y^2 - 0.017824x + 0.128332y + 0.991571 = 0$	-82.29°	21.3°	R(z): 7.706°, then R(x): 68.699°
-10°	Fig. 51	$-0.000144x^2 - 0.000150xy + 0.000505y^2 - 0.016516x + 0.112305y + 0.993537 = 0$	-83.48°	24.88°	R(z): 6.521°, then R(x): 65.116°
-10°	Fig. 51	$-0.000125x^2 - 0.000288xy + 0.000481y^2 - 0.018205x + 0.124821y + 0.992012 = 0$	-77.28°	26.44°	R(z): 12.716°, then R(x): 63.556°
-10°	Fig. 51	$-0.000158x^2 - 0.000110xy + 0.000497y^2 - 0.018071x + 0.122025y + 0.992362 = 0$	-85.26°	28.85°	R(z): 4.744°, then R(x): 61.149°
-10°	Fig. 51	$-0.000134x^2 - 0.000275xy + 0.000532y^2 - 0.016650x + 0.119691y + 0.992671 = 0$	-78.79°	23.46°	R(z): 11.212°, then R(x): 66.536°
0°	Fig. 52	$-0.000060x^2 + 0.000007xy + 0.000198y^2 + 0.001778x + 0.043991y + 0.999030 = 0$	89.25°	25.77°	R(z): -0.748°; then R(x): 64.234°
0°	Fig. 52	$-0.000576x^2 + 0.000055xy + 0.001948y^2 + 0.000895x + 0.398669y + 0.917093 = 0$	89.38°	24.8°	R(z): -0.625°; then R(x): 65.204°
0°	Fig. 52	$-0.000057x^2 - 0.0xy + 0.000179y^2 + 0.001544x + 0.044806y + 0.998995 = 0$	-89.79°	27.88°	R(z): 0.206°; then R(x): 62.116°
0°	Fig. 52	$-0.000552x^2 + 0.000072xy + 0.001949y^2 - 0.000922x + 0.345252y + 0.938508 = 0$	89.18°	22.69°	R(z): -0.822°; then R(x): 67.314°
0°	Fig. 52	$-0.000059x^2 + 0.000015xy + 0.000184y^2 + 0.001657x + 0.043311y + 0.999061 = 0$	88.27°	28.37°	R(z): -1.731°; then R(x): 61.634°
+10°	Fig. 53	$-0.001073x^2 + 0.001537xy + 0.003961y^2 + 0.134353x + 0.686313y + 0.714776 = 0$	81.51°	24.1°	R(z): -8.489°, then R(x): 65.903°
+10°	Fig. 53	$-0.000554x^2 + 0.001310xy + 0.002059y^2 + 0.084651x + 0.479676y + 0.873349 = 0$	76.69°	28.28°	R(z): -13.312°, then R(x): 61.72°

+10°	Fig. 53	$-0.000522x^2 + 0.001741xy + 0.002159y^2 + 0.081325x + 0.480539y + 0.873190 = 0$	73.5°	28.61°	R(z): -16.5°, then R(x): 61.39°
+10°	Fig. 53	$-0.000522x^2 + 0.002074xy + 0.002536y^2 + 0.083765x + 0.524870y + 0.847044 = 0$	72.93°	24.61°	R(z): -17.074°, then R(x): 65.391°
+10°	Fig. 53	$-0.000522x^2 + 0.001789xy + 0.002152y^2 + 0.081856x + 0.497265y + 0.863724 = 0$	73.1°	29.16°	R(z): -16.896°, then R(x): 60.841°
+20°	Fig. 54	$-0.000616x^2 + 0.004837xy + 0.004429y^2 + 0.343341x + 0.939008y - 0.018364 = 0$	68.1°	24.52°	R(z): -21.9°, then R(x): 65.476°
+20°	Fig. 54	$-0.000617x^2 + 0.003816xy + 0.003655y^2 + 0.325235x + 0.939028y - 0.111444 = 0$	69.11°	26.5°	R(z): -20.887°, then R(x): 63.499°
+20°	Fig. 54	$-0.000742x^2 + 0.001877xy + 0.003073y^2 + 0.269735x + 0.761745y - 0.589045 = 0$	76.9°	24.16°	R(z): -13.1°, then R(x): 65.835°
+20°	Fig. 54	$-0.000410x^2 + 0.004291xy + 0.003387y^2 + 0.316323x + 0.942756y - 0.105451 = 0$	65.75°	27.76°	R(z): -24.25°, then R(x): 62.239°
+20°	Fig. 54	$-0.000796x^2 + 0.003288xy + 0.003992y^2 + 0.333290x + 0.936185y - 0.111568 = 0$	72.76°	23.85°	R(z): -17.24°, then R(x): 66.147°
+30°	Fig. 55	$-0.000084x^2 + 0.003837xy + 0.002515y^2 + 0.405048x + 0.713480y + 0.571718 = 0$	62.06°	27.2°	R(z): -27.942°, then R(x): 62.797°
+30°	Fig. 55	$0.000049x^2 + 0.003902xy + 0.002456y^2 + 0.373934x + 0.659979y + 0.651598 = 0$	60.83°	24.41°	R(z): -29.167°, then R(x): 65.586°
+30°	Fig. 55	$0.000028x^2 + 0.003056xy + 0.001819y^2 + 0.299934x + 0.534462y + 0.790175 = 0$	60.19°	27.56°	R(z): -29.811°, then R(x): 62.436°
+30°	Fig. 55	$0.000257x^2 + 0.003843xy + 0.002043y^2 + 0.306061x + 0.545968y + 0.779889 = 0$	57.46°	24.91°	R(z): -32.536°, then R(x): 65.091°
+30°	Fig. 55	$0.000074x^2 + 0.004168xy + 0.002419y^2 + 0.442046x + 0.774898y + 0.451781 = 0$	59.68°	27.58°	R(z): -30.32°, then R(x): 62.42°
+40°	Fig. 56	$0.000468x^2 + 0.003425xy + 0.001298y^2 + 0.420068x + 0.534405y + 0.733445 = 0$	51.82°	29.73°	R(z): -38.183°, then R(x): 60.268°
+40°	Fig. 56	$0.000574x^2 + 0.005113xy + 0.002347y^2 + 0.571050x + 0.694773y + 0.437218 = 0$	54.56°	25.31°	R(z): -35.435°, then R(x): 64.686°
+40°	Fig. 56	$0.000898x^2 + 0.006020xy + 0.002507y^2 + 0.627849x + 0.774096y + 0.080861 = 0$	52.48°	24.41°	R(z): -37.518°, then R(x): 65.594°
+40°	Fig. 56	$0.000551x^2 + 0.005026xy + 0.002280y^2 + 0.576093x + 0.713776y - 0.398260 = 0$	54.49°	26.23°	R(z): -35.509°, then R(x): 63.771°
+40°	Fig. 56	$0.000688x^2 + 0.005165xy + 0.002159y^2 + 0.620100x + 0.772699y - 0.135577 = 0$	52.95°	26.54°	R(z): -37.051°, then R(x): 63.455°